**UNIVERSITY OF CALIFORNIA,
IRVINE**

Fast Ions and Shear Alfvén Waves

DISSERTATION

submitted in partial satisfaction of the requirements for the degree of

DOCTOR OF PHILOSOPHY

in Physics

By

Yang Zhang

Dissertation Committee:
Professor William W. Heidbrink, Co-chair
Professor Roger McWilliams, Co-chair
Professor Zhihong Lin

2008

The dissertation of Yang Zhang
is approved and is acceptable in quality
and form for publication on microfilm

_____

_____

_____

Committee Chair

University of California, Irvine
2008

DEDICATION

To my wife Lily,
and my parents,
for their love and support.

The LORD is my rock, and my fortress, and my deliverer; my God, my strength, in whom I will trust; my buckler, and the horn of my salvation, and my high tower.
Psalm 18:2

TABLE OF CONTENTS

LIST OF FIGURES

LIST OF TABLES

TABLES…….Page

LIST OF SYMBOLS

$\boldsymbol{B}_0$	Ambient Magnetic Field
$\tilde{B}_\theta$	Wave Magnetic Field Azimuthal Component
$\tilde{\mathbf{B}}$	Wave Magnetic Field
b	Gauss Fit Coefficient Of Fast Ion Profile (Proportional To FWHM)
c	Speed Of Light
c_s	Ion Sound Speed
e	Electronic Charge
$\mathbf{D}$	Electric Displacement Vector
$\tilde{\mathbf{E}}$	Plasma Wave Electric Field
$\tilde{\mathrm{E}}_y$	Plasma Wave Electric Field Along The Y Direction
$\tilde{\mathrm{E}}_z$	Plasma Wave Electric Field Component Parallel To $\boldsymbol{B}_0$
$\tilde{\mathbf{E}}_{//}$	Plasma Wave Electric Field Component Parallel To $\boldsymbol{B}_0$
$\tilde{\mathbf{E}}_{\perp}$	Plasma Wave Electric Field Component Perpendicular To $\boldsymbol{B}_0$
f_{Bragg}	Bragg Frequency Of A Periodic System
f_{G}	Saw Gap Frequency
f_{+}	Saw Upper Continuum Frequency
f_{-}	Saw Lower Continuum Frequency
f_{ci}	Plasma Ion Cyclotron Frequency
I_{ant}	Antenna Current
$\boldsymbol{j}_{\mathrm{a}}$	Antenna Current Density
k	Boltzmann's Constant
k_{Bragg}	Bragg Wave Vector
$k_{//}$, k_{z}	Wave Vector Component Parallel To $\boldsymbol{B}_0$
$k_{\perp}$	Wave Vector Component Perpendicular To $\boldsymbol{B}_0$
L_{a}	Antenna Length (Rod)
L_{m}	Magnetic Mirror Length Perpendicular To $\boldsymbol{B}_0$
m	Mass; Wave Mode Number
M	Magnetic Mirror Depth
m_e	Mass Of Electron
m_f	Mass Of Fast Ion
m_i	Mass Of Plasma Ion
n	Integer Wave Mode Number

n_e	Electron Density
n_i	Plasma Ion Density
P	Fast Ion Signal Intensity
q_{f}	Fast Ion Charge
r_0	Gyro-Radius
r	Radial Coordinate
r_{SAW}	Saw Perturbed Fast Ion Radial Coordinate
t	Time
T_e	Electron Temperature
T_i	Ion Temperature
U	Saw Magnetic Disk Energy Density
V	Voltage
$\mathbf{v}$	Fast Ion Velocity
$\mathrm{v}_{\perp}$	Velocity Component Perpendicular To Magnetic Field
$\mathrm{v}_{\parallel}$, v_z	Velocity Component Parallel To Magnetic Field
v_e	Electron Velocity
v_i	Plasma Ion Velocity; Ion Sound Speed
V_f	Plasma Floating Potential
W	Beam Energy
$W_{\perp}$	Beam Energy Perpendicular To $\boldsymbol{B}_0$
$W_{//}$	Beam Energy Parallel To $\boldsymbol{B}_0$
$\mathbf{x}$	Fast Ion Coordinate
z	Axial Position In The Lapd Parallel To $\boldsymbol{B}_0$
δz	Fast Ion Travel Distance Parallel To $\boldsymbol{B}_0$
$\bar{\beta}_e$	Electron Beta To Determine Kinetic (>>1) Or Inertial (<<1) Alfvén Wave
δ_{s}	Electron Skin Depth
δB	Wave Magnetic Field Instensity
$\Delta \mathrm{r}$	SAW Induced Fast Ion Displacement Along The Radial Direction
$\Delta\Phi$	SAW Induced Fast Ion Displacement Along The Gyro Direction
ε_0	Permittivity Of Free Space
$\varepsilon_{\alpha\beta}$	Plasma Dielectric Tensor
θ	Fast Ion Pitch Angle
ν_{ei}	Electron-Ion Coulomb Collision Rate
$\nu_{e-Landau}$	Effective Landau Damping Collision Frequency

ω_{ci}	Plasma Ion Cyclotron Frequency
ω_{pi}	Ion Plasma Frequency
$\bar{\omega}$	Normalized Wave Angular Frequency
ρ_0	Fast Ion Beam Charge Density
ρ	Gyro-Radius
ρ_s	Ion Sound Gyro-Radius
$\tau_{Cyclotron}$	Fast Ion Gyro Period
τ_{PAS}	Pitch Angle Scattering Time
τ_{SAW}	Saw Period
τ_{trap}	Trapping Period Of Fast Ion In Wave Field
τ_W	Fast Ion Slowing-Down Time
ϕ	Gyro Phase
φ_0	Phase Difference Between Fast Ion And Alfvén Wave
χ^2	Chi Square Test
μ	Magnetic Moment
μ_0	Permeability Of Free Space
Ω_f	Fast Ion Gyro-Frequency

ACKNOWLEDGMENTS

I was very glad when I first got into the UC Irvine fast-ion transport group. The faculty-to-student ratio has been 3 to 1 for nearly three years after Liangji graduated. I don't know if this is a nation high but I surely enjoyed the affluent experimental plasma physics from all my advisors, Professor William W. Heidbrink, Professor Roger McWilliams and Dr. Heinrich Boehmer.

Bill has always been an energetic researcher (it may be completely uncorrelated to address here that his concentration is on energetic particles in fusion devices). The experiment weeks at the LAPD facility are intense. I could barely stay awake after a whole day of setting up instruments and tuning devices when I first started four years ago. Now my stamina has been trained to last more than 14 hours a day, 7 days straight, all because that Bill has set himself as a good example.

Roger is an experimental physicist, a jazz musician and an automobile hobbyist. He taught me to train and trust my own senses before using any advanced instruments, as well as the experimental skills in his plasma laboratory. He always shows me how confident and eloquent a physicist can truly be. I still remember the time I was first amazed by "Take Five" when he played sax with his band at the University Club, UC Irvine. His performance at my wedding banquet was a great gift to Lily and me.

Dr. Boehmer's memory is always young for all the experiments that he has done. I learned what is called German efficiency and accuracy from him. His knowledge and experience on fast-ion sources contributes greatly in the design and application of the lithium fast-ion sources in this thesis. He told me that he enjoys pondering on a physics problem in the afternoon breeze with a glass of wine. The coupled-wave model in the

second experiment of this thesis, for example, was a direct outcome of this habit.

I would also like to thank the LAPD group at UCLA, including Professor Walter Gekelman, Dr. David Leneman, and Dr. Steve Vincena, for their hospitality at the facility and essential support to this thesis work. Their expertise in shear Alfvén waves makes the final fast-ion-wave resonance results possible. Professor Troy Carter and Brian Brugman provided us with their loop antenna and power supply, Patrick Pribyl designed the *b-dot* probes used in this thesis work and helped a lot with our noise reduction.

I would like to thank all the people that contributed to this thesis work at UC Irvine. Liangji Zhao was my predecessor who initiated the transport project and finished the fast-ion classical transport study and the Monte-Carlo simulation code. Professor Boris N. Breizman (Univ. Texas, Austin) proposed the mirror-array experiment and Guangye Chen (Univ. Texas, Austin) used his 2D finite difference code to simulate the spectral gap experiment. I thank Professor Liu Chen for his enlightenment in resonance and wave theories. I thank Virgil Laul, Rung Hulme for their helps in mechanical engineering. I thank all the “comrade” graduate students including Wayne Harris, Yadong Luo, Deyong Liu, Zehua Guo, Erik Trask, and Tommy Roche for their support and discussions.

I thank my dear wife, Lily Wu, for always being with me through the good times and bad times of my graduate school life.

Above all else, I want to thank Jesus Christ for being my personal savior and helper all the time. No matter what good I want to accomplish in my life, He always gives me another chance to try, which turned out to be so important when doing experimental plasma physics. I have never been this confident yet respectful when I am facing problems in research and life.

CURRICULUM VITAE

Yang Zhang

FIELD OF STUDY:

- Experimental Plasma Physics

EDUCATION:

- Ph. D. in Plasma Physics, UC Irvine 03/2008
- M.S. in Plasma Physics, UC Irvine 10/2004
- B.S. in Applied Physics,
  University of Science and Technology of China (USTC) 07/2002

COLLABORATIONS:

- The Basic Plasma Science Facility—the Large Plasma Device (LAPD)
  UCLA 07/2004-03/2008
- Guangye Chen (Department of Aerospace Engineering and Engineering Mechanics), Boris N. Breizman (Institute for Fusion Studies),
  University of Texas, Austin 01/2006-03/2008
- The CRPP Plasma Lab at EPFL (Lausanne, Switzerland) 01/2006-03/2008
- Laboratory for Low Temperature Plasmas (KAIST, Korea) 10/2006-02/2007

HONORS & AWARDS:

- Regents Fellowship, $10,000, UC Irvine 09/2002-06/2004

PUBLICATIONS

- *Observation of Fast-Ion Doppler-Shifted Cyclotron Resonance with Shear Alfvén Waves*
  Y. Zhang, H. Boehmer, W.W. Heidbrink, R. McWilliams (UC Irvine), S. Vincena, T. Carter, D. Leneman, P. Pribyl, W. Gekelman (UCLA), Phys. Plasmas, to be submitted 2008

- *Fundamental Studies of Alfvén Waves and Fast Ions in the LArge Plasma Device*
  Proceedings of 10th International Atomic Energy Agency Technical Meeting on Energetic Particles in Magnetic Confinement Systems, Max-Planck-Institut für Plasmaphysik, Garching,

Germany 10/2007
Yang Zhang,[a] H. Boehmer,a B.N. Breizman,[b] T. Carter,[c] Guangye Chen,[b] W. Gekelman,[c] W.W. Heidbrink,[a] D. Leneman,[c] R. McWilliams,[a] and S. Vincena[c], P. Pribyl[c] ([a]UC, Irvine; [b]University of Texas, Austin (UT, Austin); [c]University of California, Los Angeles (UCLA))

- *Spectral Gap of Shear Alfvén Waves in a Periodic Array of Magnetic Mirrors*
  Yang Zhang, W.W. Heidbrink, H. Boehmer, R. McWilliams (UC Irvine) Guangye Chen, B. N. Breizman (UT Austin)S. Vincena, T. Carter, D. Leneman, W. Gekelman, P. Pribyl, B. Brugman (UCLA), Phys. Plasmas, **15**, 012103 01/2008

- *Lithium Ion Sources for Investigation of Fast-ion Transport in Magnetized Plasma*
  Y. Zhang, H. Boehmer, W. W. Heidbrink, R. McWilliams, D. Leneman, S. Vincena, Rev. Sci. Instrum. **78**, 013302 01/2007

- *Fast-ion source and detector for investigating the interaction of turbulence with suprathermal ions in a low temperature toroidal plasma*
  G. Plyushchev, A. Diallo, A. Fasoli, I. Furno, B. Labit, S. H. Müller, M. Podestà, and F. M. Poli (EPFL), H. Boehmer, W. W. Heidbrink, and **Y. Zhang** (UC Irvine)
  Rev. Sci. Instrum. **77**, 10F503 01/2006

- *Fundamental Studies of Alfvén Waves and Fast Ions in the LArge Plasma Device*
  Proceedings of 9th International Atomic Energy Agency Technical Meeting on Energetic Particles in Magnetic Confinement Systems, Hida Earth Wisdom Center, Takayama, Japan. NIFS-PROC-63, p107 2005
  Yang Zhang, H. Boehmer, W.W. Heidbrink, R. McWilliams, L. Zhao, (UC Irvine); B. Brugman, , T. Carter, D. Leneman, S. Vincena (UCLA)

PRESENTATIONS:

- *Observation of Fast-Ion Doppler-Shifted Cyclotron Resonance with Shear Alfvén Waves* (Oral Pres.)
  SciDAC (www.scidac.gov) Gyrokinetic Simulation of Energetic Particle Turbulent and Transport Workshop 01/2008
  21st US-European Transport Taskforce Workshop, IAEA, Boulder, CO 03/2008
  Y. Zhang, W.W. Heidbrink, H. Boehmer, R. McWilliams (UC Irvine) S. Vincena, T. Carter, D. Leneman, P. Pribyl, W. Gekelman (UCLA)

- *Magnetic Mirror Array Induced Alfvén Spectral Gaps and Continua* (Seminar)
  Physics and Astronomy, UCLA, 05/2007
  Y. Zhang, W.W. Heidbrink, H. Boehmer, R. McWilliams (UC Irvine) Guangye Chen, Boris N. Breizman (UT Austin)S. Vincena, T. Carter, D. Leneman, W. Gekelman, B. Brugman (UCLA)

- *Shear Alfvén Wave (SAW) Spectra in a Periodic Magnetic Mirror Array* (Oral Pres.)
  12th US-European Transport Taskforce Workshop, IAEA, San Diego, CA 04/2007
  Y. Zhang, W.W. Heidbrink, H. Boehmer, R. McWilliams (UC Irvine) Guangye Chen, Boris N. Breizman (UT Austin)S. Vincena, T. Carter, D. Leneman, W. Gekelman, B. Brugman (UCLA)

- *Transport of Fast Ions in Shear Alfvén Waves* (Oral Pres.)
  Yang Zhang, Fast-Ion Workshop at Basic Plasma Facility, UCLA, 02/2006

ABSTRACT OF THE DISSERTATION

Fast Ions and Shear Alfvén Waves

By

Yang Zhang

Doctor of Philosophy in Physics

University of California, Irvine, 2008

Professor William W. Heidbrink, Co-Chair

Professor Roger McWilliams, Co-Chair

In order to study the interaction of ions of intermediate energies with plasma fluctuations, two plasma immersible lithium ion sources, based on solid–state thermionic emitters (Li aluminosilicate) were developed. Compared to discharge based ion sources, they are compact, have zero gas load, small energy dispersion, and can be operated at any angle with respect to an ambient magnetic field of up to 4.0 kG. Beam energies range from 400 eV to 2.0 keV with typical beam current densities in the 1 mA/cm^2 range. Because of the low ion mass, beam velocities of 100 – 300 km/s are in the range of Alfvén speeds in typical helium plasmas in the LArge Plasma Device (LAPD).

The Doppler-shifted cyclotron resonance ($\omega - k_z v_z = \Omega_f$) between fast ions and shear Alfvén waves is experimentally investigated. (ω: wave frequency; k_z: axial wavenumber; v_z: fast-ion axial speed; Ω_f: fast-ion cyclotron frequency.) A test particle beam of fast ions is launched by a Li^+ source in the helium plasma of the Large Plasma Device (LAPD), with shear Alfvén waves (SAW) (amplitude $\delta B / B$ up to 1%) launched by a

loop antenna. A collimated fast-ion energy analyzer measures the non-classical spreading of the beam, which is proportional to the resonance with the wave. A resonance spectrum is observed by launching SAWs at 0.3 – 0.8 ω_{ci}. Both the magnitude and frequency dependence of the beam-spreading are in agreement with the theoretical prediction using a Monte Carlo Lorentz code that launches fast ions with an initial spread in real/velocity space and random phases relative to the wave. Measured wave magnetic field data are used in the simulation. Measurements of fast-ion signals on selected fast-ion energies confirm that the particles gain/lose energy from/to the wave.

A multiple magnetic mirror array is formed at the LAPD to study axial periodicity-influenced Alfvén spectra. SAWs are launched by antennas inserted in the LAPD plasma and diagnosed by B-dot probes at many axial locations. Alfvén wave spectral gaps and continua are formed similar to wave propagation in other periodic media due to the Bragg effect. The measured width of the propagation gap increases with the modulation amplitude as predicted by the solutions to Mathieu's equation. A 2-D finite-difference code modeling SAW in a mirror array configuration shows similar spectral features. Machine end-reflection conditions and damping mechanisms including electron-ion Coulomb collision and electron Landau damping are important for simulation.

Chapter 1

INTRODUCTION

1.1 Fast Ions and Alfvén Waves In Plasmas

Fast ions are ions with energies that are much larger than typical thermal energies of plasma constituents. In laboratory experiments, fast ions are produced by neutral or ion beam injection, by ion cyclotron or lower hybrid heating, and by fusion reactions. In astrophysical and space plasmas, instabilities and shocks generate fast ions. Fast ions also are found when a hot plasma merges with a colder background plasma, as when the solar wind collides with the magnetosphere.

Alfvén waves are also pervasive in both natural and laboratory plasmas. Alfvén waves constitute the dominant components of the electromagnetic wave spectra in the solar-terrestrial plasma environments and, consequently, can play crucial roles in mechanisms from solar corona heating to acceleration of charged particles in the solar wind[1, 2], aurora and the Earth's radiation belts. Resonances between energetic particles and Alfvén waves are also suggested as one generating mechanism for the waves.

In many toroidal laboratory devices, Alfvén waves driven unstable by fast ions are observed with an intense fast-ion population. For example, the famous toroidicity-induced Alfvén eigenmode[3, 4] (TAE) is the most extensively studied among numerous other modes excited by energetic particles.[4, 5] Fast ions can also be expelled by

these Alfvén instabilities and damage vessel components in fusion experiments.[6, 7] Resonant heating of fast ions by Alfvén waves well below the ion cyclotron resonance frequency might cause ion heating in toroidal fusion devices[5, 8, 9].

The interaction of fast ions with waves and instabilities is challenging to study experimentally because of difficulties in diagnosing the fast-ion distribution function and the wave fields accurately, in either hot fusion devices or space plasmas. Conventional experimental approaches are limited to non-contact, line or volume averaged methods in a tokamak, such as various spectrometers and edge scintillators/collectors for fast ions[4]. The Interplanetary Scintillation (IPS) array built at the Mullard Radio Astronomy Observatory was a representative remote diagnostics for monitoring the solar wind activities. Expensive spacecraft measurements near the earth can cover but a fraction of the daunting space influenced by the solar wind.

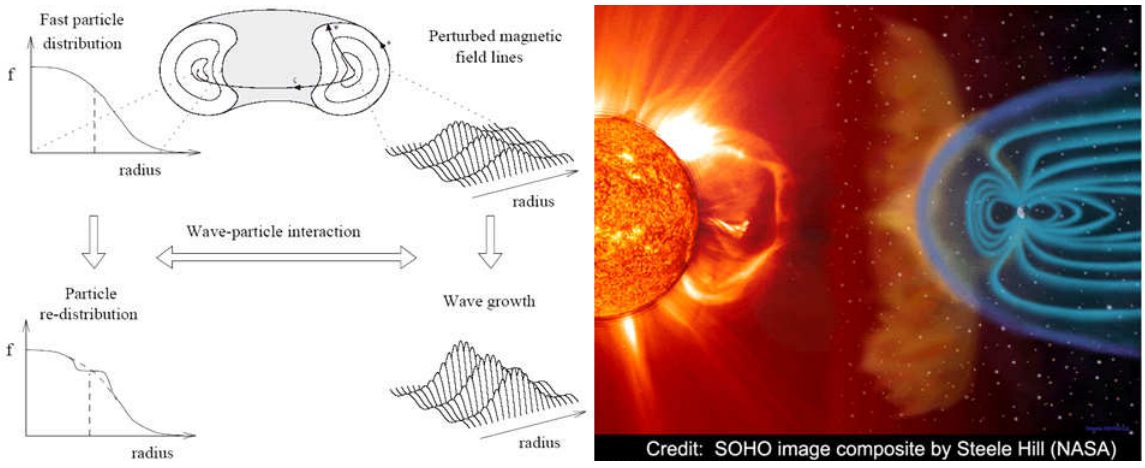

FIG. 1.1. Illustrations of wave-particle interactions in fusion devices and space plasmas.
left: wave-particle interaction in a toroidal fusion device (Pinches, Ph. D. Thesis[10]); right: Solar and Heliospheric Observatory (SOHO) image demonstrating the influence of the solar wind on earth's magnetosphere.

1.2 Fast-ion Transport Project at UC Irvine

Starting from September 2004, this thesis work continues the effort that was awarded $326K from 8/15/2003- 8/14/2006 as DOE grant DE-FG03-03ER54720, entitled "Fast-ion studies in the Large Plasma Device", where the Large Plasma Device (LAPD)[11] at UCLA is a national user facility for basic plasma research. In May 2006, UC Irvine team was renewed to be funded at $100K per year for three years. Fast-ion transport studies are carried out with three phases. Classical fast-ion transport during the afterglow of the LAPD was investigated during Phase I (2003 – 2005, Dr. L. Zhao). Phase II is finished during this thesis work, which concentrates on the interactions between fast-ions and Alfvén waves. Fast-ion nonlinear heating and transport in turbulent fluctuations will be studied during Phase III.

During this thesis work, we have developed two lithium sources that are capable of working at large pitch angles, published an instruments paper on the lithium sources,[22] developed collimated fast-ion analyzers that detect fast-ion signals during the active discharge plasma in the LAPD, published a physics paper on spectral gaps of Alfvén waves in a magnetic mirror array,[12] submitted a physics paper on resonant interactions of fast ions with shear Alfvén waves,[13] established collaborations with research teams from three institutions including UCLA, University of Texas, Austin (UT Austin) and the Ecole Polytechnique Federale de Lausanne (EPFL), and presented papers at various domestic and international conferences.

The fast-ion sources developed are the major pieces of equipments contributed by UC Irvine. The laboratory facilities at UC Irvine provide a valuable testbed for

developmental activities. The Irvine Mirror and Electron-Positron Machine (EPM) have been modified to accommodate the entire source apparatus. New probes and source improvements are conveniently tested at UC Irvine.

As part of their 5-year renewal (2005 – 2010), the LAPD will include two campaigns[14] in their program—a fusion-related and a space-related campaign. These campaigns are supported by personnel and equipment that is supplied by the facility. Approximately one month of experimental runtime will be devoted to each campaign. The fusion-related campaign is led by Professor William Heidbrink and the focus is "energetic ion physics of relevance to fusion research." Many experimentalists, theorists, and modelers from various institutions including UC Irvine and UT Austin have actively participated. This thesis work is part of this fast-ion campaign.

1.3 Previous Classical Fast-ion Transport Study

During Phase I of the fast-ion transport project (2003 – 2005, Dr. Liangji Zhao), classical fast-ion transport during the afterglow of the LAPD is investigated. A 3-cm diameter rf ion gun launches a pulsed, ~300 eV ribbon shaped argon ion beam parallel to or at 15 degrees to the magnetic field in the LAPD. The parallel energy of the beam is measured by a two-grid energy analyzer at two axial locations ($z = 0.32$ m and $z = 6.4$ m) from the ion gun in LAPD. To measure cross-field transport, the beam is launched at 15 degrees to the magnetic field. To avoid geometrical spreading, the radial beam profile measurements are performed at different axial locations where the ion beam is periodically focused. The measured cross-field transport is in agreement to within 15% with the analytical classical collision theory and the solution to the Fokker-Planck kinetic

equation. Collisions with neutrals have a negligible effect on the beam transport measurement but do attenuate the beam current. The beam energy distribution measurements are calibrated by LIF (laser induced fluorescence) measurements[15] performed in the Irvine Mirror.

The **slowing-down** of the fast-ion beam has been measured when the ion beam source was in the direction parallel with the uniform magnetic field in the LAPD. The ion beam deceleration is mainly due to the Coulomb drag by the thermal electrons. The measured energy loss time is in agreement within 10% with the standard theoretical prediction.

The **cross-field diffusion** was measured when the ribbon shape ion beam was launched at 15 degrees to the magnetic field. The cross-field spreading of the beam was observed by scanning over the different planes normal to the magnetic field. The measured diffusion coefficient is consistent within 15% with the classical Coulomb collision theory and the solution to the Fokker-Planck kinetic equation.

The **energy diffusion** was not observed in this experiment. The beam ions in the current experiment move so fast in the parallel direction and the fast-ion travel time is so short ($t \sim 6\times10^{-5}$ sec.) that the parallel velocity diffusion (energy diffusion time $\tau \sim 2$ sec) is obscured by initial energy spreading of the ion beam (~15 eV).

The charge-exchange and elastic scattering with the neutral particles does not have significant effects on the measurements of the fast-ion transport in this experiment, but the beam current decreases exponentially due to the loss of the fast ions caused by the collisions with the neutrals. The observations are consistent with the theoretical (Monte Carlo simulation) predictions.

1.4 Shear Alfvén Waves in the Upgraded LAPD

The LAPD is ideal for studying SAW because its large physical size, and sufficiently high plasma density and magnetic field, allow it to accommodate multiple Alfvén wavelengths. Research on SAW properties in the LAPD dates back to 1994 when a pair of theoretical[16,17] and experimental[18,19] papers were published on SAWs radiated from small perpendicular scale sources in the LAPD. Subsequently, other mechanisms were discovered to generate Alfvén waves including a variety of inserted antennas, resonance between the LAPD cathode and the semi-transparent anode—the Alfvén Maser[20], and a dense laser-produced plasma expansion[21].

Two regimes of plasma parameters for SAW propagation have been investigated for the cylindrical LAPD plasma with uniform axial magnetic field: the Kinetic Alfvén Wave (KAW) for plasma electrons having a Boltzmann distribution in the presence of the Alfvén wave fields and the Inertial Alfvén Wave (IAW) for electrons responding inertially to the wave. The KAW is more relevant to the physics of the interior regions of tokamak plasmas and the IAW to the edge and limiter regions. A dimensionless parameter— $\overline{\beta}_e \equiv \overline{\mathrm{v}}_{te}^2 / \mathrm{v}_A^2$ is a quantitative measure of how inertial or kinetic a plasma region is, where $\overline{\mathrm{v}}_{te} = \sqrt{2T_e / m_e}$ is the thermal electron speed with T_e the electron temperature. If $\overline{\beta}_e >> 1$, the region is kinetic; if $\overline{\beta}_e << 1$, then it is inertial. The standard MHD (magnetohydrodynamic) SAW dispersion relation is

$$k_{//}^2 c^2 = \frac{\omega^2 \omega_{pi}^2}{\omega_{ci}^2 - \omega^2} - \frac{1}{2} k_\perp^2 c^2 + \sqrt{\frac{1}{4} k_\perp^4 c^4 + \frac{\omega_{pi}^4}{(\omega_{ci}^2 - \omega^2)^2} \frac{\omega^6}{\omega_{ci}^2}}\,, \tag{1.1}$$

which can be reduced to the following form in the limit of $k_{//} << k_{\perp}$,

$$\omega^2 / k_{//}^2 = \mathrm{v}_A^2(1-\bar{\omega}^2), \tag{1.2}$$

where $\bar{\omega} = \omega / \omega_{ci}$ and $k_{//}$ is the component of the wave vector parallel to the background magnetic field. The corrections to the dispersion relation for the KAW are proportional to $k_{\perp}^2\rho_s^2$, where $k_{\perp}$ is the perpendicular wave number and ρ_s is the ion sound gyro-radius $\rho_s = c_s / \omega_{ci}$ with $c_s = \left(T_e / m_i\right)^{1/2}$. The IAW correction is proportional to $k_{\perp}^2\delta_e^2$, where δ_e is the electron skin depth, $\delta_e = c / \omega_{pe}$ with $\omega_{pe} = \sqrt{\frac{n_e e^2}{\varepsilon_0 m_e}}$ as the plasma frequency. In this experimental work, both correction factors are on the order of 0.1 and thus negligible.

An important departure from MHD is that a component of the wave electric field may be sustained parallel to $\mathbf{B_0}$ due to finite electron pressure (KAW) or inertia (IAW). This parallel electric field can lead to energization of the background electrons and thus excite the wave, which can be done by direct application of an oscillating charge density to a flat, circular mesh "disk antenna"[26] within the plasma, or it may be excited inductively using a "blade antenna"[15, 16] which is an externally fed current with one leg within the plasma parallel to the background field. For either excitation mechanism, there are some general characteristics of the radiated wave field patterns which may be illustrated by considering the disk exciter in detail. Within or close to the inertial regime, a single SAW cone can be excited from both antennas. Assuming azimuthal symmetry, the wave magnetic field has one dominant component $\tilde{B}_{\theta}$ as a function of *r* and *z*:[16]

$$\tilde{B}_{\theta} \propto \frac{I_{ant}}{a}\int_0^{\infty} dk_{\perp}\,\frac{\sin k_{\perp}a}{k_{\perp}}\,J_1\left(k_{\perp}r\right)\exp\left[ik_{//}z\right], \tag{1.3}$$

in which I_{ant} is the antenna current amplitude and a is the radius of the antenna cross-section. There are three characteristic features of the radial profiles: 1) the field is always zero at the disk center; 2) it increases with the radial distance away from the disk center until reaching a peak value, the radial location of which increases with axial distance away from the exciter; 3) upon reaching the position, r_{edge} (the location of the outer Alfvén cone), defined by

$$r_{edge} = \left(\frac{\omega}{v_A} \delta_e z / \sqrt{1-\bar{\omega}^2} \right) + a , \tag{1.4}$$

the wave magnetic field decreases as *1/r*.

1.5 Content of Thesis

This thesis is composed based on two major experiments. The first experiment launches test-particle fast-ion beams in the LAPD with a narrow initial distribution function in phase space using plasma immersible fast-ion sources[22, 23]. The unique LAPD provides a probe-accessible plasma that features dimensions comparable to fusion devices, which can accommodate both large Alfvén wave lengths and fast-ion gyro orbits. The fast-ion beam is readily detected by a collimated fast-ion analyzer. With resonance overlap of fast ions and shear Alfvén waves, resonant beam transport in addition to the well calibrated classical transport is analyzed with good phase-space resolution.

The second experiment studies shear Alfvén wave (SAW) propagation and forbidden gap formation in a periodic magnetic mirror array. The experiments are performed in the Large Plasma Device (LAPD). Although the number of mirror cells is limited, the LAPD is capable of generating a magnetic mirror array resembling the multi-mirror magnetic

confinement fusion devices[24, 25] in Novosibirsk, Russia. An advantage of the low-temperature plasma in the LAPD is its accessibility to a variety of probes. Alfvén wave propagation and interference can be studied with spatial resolution of ~ 1 – 10 mm. To further investigate the Alfvén spectral gaps and continua, a cold-plasma wave code[26] is adapted to launch Alfvén waves in a virtual LAPD with the number of mirror cells ranging from a few to infinite. Measured plasma parameters are used in the code to simulate wave spectra which are compared with experimental observations.

The arrangement of this thesis is as follows. Most of the important experimental hardware including the lithium fast-ion sources, detectors and the LAPD facility are introduced in *Chapter 2*. The results of fast-ion Doppler-shifted cyclotron resonance experiment are presented in *Chapter 3* and the phenomenon of SAW spectral gaps in the LAPD mirror array is discussed in *Chapter 4*. A conclusion to the Phase II of the fast-ion transport project and future work in the coming Phase III are stated in *Chapter 5*.

[1] Joseph V. Hollweg and Philip A. Isenberg, J. Geophys. Res. **107** (A7), 1147 (2002).

[2] Valentin Shevchenko, Vitaly Galinsky, and Dan Winske, Geophys. Res. Lett. **33**, L23101 (2006).

[3] C. Z. Cheng, L. Chen, and M. S. Chance, Ann. Phys. **161** (1985) 21.

[4] W.W. Heidbrink, Phys. of Plasmas, **15**, 055501 (2008)

[5] King-Lap Wong, Plasma Phys. Cont. Fusion **41.** R1 (1999).

[6] H. H. Duong, W. W. Heidbrink, E. J. Strait, *et al.,* Nucl. Fusion **33,** 749 (1993).

[7] R. B. White, E. Fredrickson, D. Darrow *et al.,* Phys. Plasma **2,** 2871 (1995).

8 L. Chen, Z. H. Lin, and R. White, Phys. Plasmas **8**, 4713 (2001)

9 R. White, L. Chen, and Z. H. Lin, Phys. Plasmas **9**, 1890 (2002).

[10] S. D. Pinches, Ph. D. thesis, University of Nottingham, 1996, http://www.rzg.mpg.de~sip/thesis/node1.html.

[11] W. Gekelman, H. Pfister, Z. Lucky, J. Bamber, D. Leneman, and J. Maggs, Rev. Sci. Instrum. **62**, 2875 (1991)

[12] Yang Zhang, W.W. Heidbrink, H. Boehmer, R. McWilliams, Guangye Chen, B. N. Breizman, S. Vincena, T. Carter, D. Leneman, W. Gekelman, P. Pribyl, B. Brugman, Phys. Plasmas, **15**, 012103 (2008)

[13] Yang Zhang, W.W. Heidbrink, H. Boehmer, R. McWilliams, S. Vincena, T. Carter, W. Gekelman, D. Leneman, P. Pribyl, Phys. Plasmas, submitted, 2008

[14] http://plasma.physics.ucla.edu/bapsf/pages/current.html

[15] D. Zimmerman, Master thesis, University of California, Irvine (2004)

[16] G. J. Morales, R. S. Loritsch, and J. E. Maggs, Phys. Plasmas **1**, 3765 (1994).

[17] G. J. Morales and J. E. Maggs, Phys. Plasmas **4**, 4118 (1997).

[18] W. Gekelman, D. Leneman, J. Maggs, and S. Vincena, Phys. Plasmas **1,** 3775 (1994).

[19] W. Gekelman, S. Vincena, D. Leneman, and J. Maggs, J. Geophys. Res. **102**, 7225 (1997).

[20] J. E. Maggs, G. J. Morales, and T. A. Carter, Phys. Plasmas **12**, 013103 (2005).

[21] M. VanZeeland, W. Gekelman, S. Vincena and G. Dimonte, Phys. Rev. Lett. **87** (10), 2673 (1999).

[22] Y. Zhang, H. Boehmer, W. W. Heidbrink, R. McWilliams, D. Leneman and S. Vincena, Rev. Sci. Instrum. **78**, 013302 (2007).

[23] H. Boehmer, D. Edrich, W.W. Heidbrink, R. McWilliams, and L. Zhao, Rev. Sci. Instrum., **75**, 1013 (2004).

[24] A. A. Ivanov, A. V. Anikeev, P. A. Bagryansky, V. N. Bocharov, P. P. Deichuli, A. N. Karpushov, V. V. Maximov, A. A. Pod'minogin, A. 1. Rogozin, T. V. Salikova, and Yu. A. Tsidulko, Phys. Plasmas **1** (5), 1529 (1994).

[25] E. P. Kruglyakov, A. V. Burdakov, and A. A. Ivanov, AIP Conf. Proc. **812**, 3 (2006).

[26] Guangye Chen, Alexey V. Arefiev, Roger D. Bengtson, Boris N. Breizman, Charles A. Lee, and Laxminarayan L. Raja, Phys. Plasmas **13,** 123507 (2006).

Chapter 2

EXPERIMENTAL APPARATUSES

For modern experimental physicists, conventional apparatuses and emerging electronic devices are necessities for a successful experiment. Computational models on the other hand are often regarded as theorists' specialty tools. This thesis work requires applications of all of the above. This chapter discusses hardware tools used in this project:

- Sec. 2.1: The upgraded LAPD, the discharge plasma;
- Sec. 2.2: Irvine Electron-Positron chamber—the test bed in Irvine;
- Sec. 2.3: Fast-ion sources developed at UC Irvine;
- Sec. 2.4: Shear Alfvén wave antennas;
- Sec. 2.5: Diagnostic tools for plasma, fast ions and Alfvén waves.

2.1 Basic Plasma Science Facility at UCLA—the Upgraded LAPD

The Basic Plasma Science Facility at UCLA commenced in August of 2001. It is a frontier plasma research user facility. The core of the facility is a modern, large plasma device (the LAPD) constructed by Professor Walter Gekelman (the facility director) and

his staff of reserch scientists and technicians. The first plasma was achieved in July, 2001 and the machine is now in operation. Usage of the facility is available to scientists from national and international institutions, as well as industry. The unique nature of the LAPD enables understanding of topics on the fundamental properties of plasmas related both to fusion energy and space science.

The cylindrical vacuum chamber of the LAPD is one meter in diameter, ~ 20 m long, and has excellent diagnostic access. The device produces reproducible plasmas at 1 Hz continuously. The magnetically confined, linear plasma is generated by applying a 50 – 100 V voltage pulse between a 75 cm diameter Barium Oxide cathode and a grid anode with a ~ 2 kA discharging current pulse at a 1 Hz repetition rate. Operating gases include hydrogen, helium, argon and neon with partial pressures controlled by individual leak valves and monitored by a central Residual Gas Analyzer (RGA). During the discharge of 8 - 10 ms duration, the plasma density can reach 5 x 10^{12} cm^{-3} with an electron temperature of 10 eV. The plasma density decays in the afterglow with an initial time constant of ~10 ms; the plasma temperature drops within ~100 μs. While the plasma contains various modes of turbulence during the discharge, it is quiet in the afterglow. Normally, a uniform, ~1 kG magnetic field is employed but reconfiguration of the coils and higher field strengths are possible. Plasma parameters and fluctuations are diagnosed with a millimeter wave interferometer (at port 23), Langmuir probes of various configurations and three axis *b-dot* probes for the measurement of magnetic field fluctuations, for example of Alfvén waves. A sophisticated data acquisition system consisting of computer-controlled actuators, digitizers, and workstations accommodate automated probe scans.

For this thesis work and the planned fast-ion investigations of plasma turbulence, helium is the major working gas. It will primarily focus on fast-ion interactions with waves and turbulence during the high-density discharge, when the fast-ion beam density of 5.0 x 10^{8} cm^{-3} is typically four orders of magnitude smaller than the plasma density during the discharge.

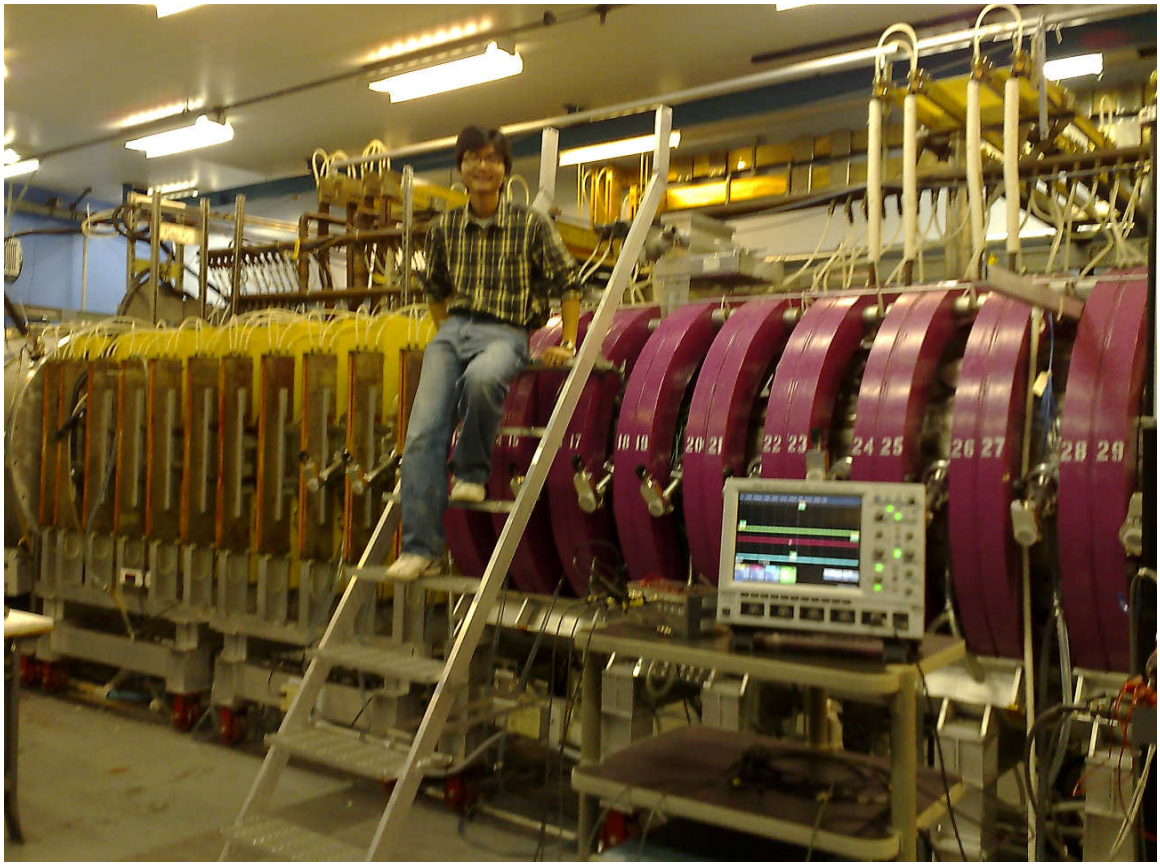

FIG. 2.1. A photograph of the LAPD machine and the experimenter.

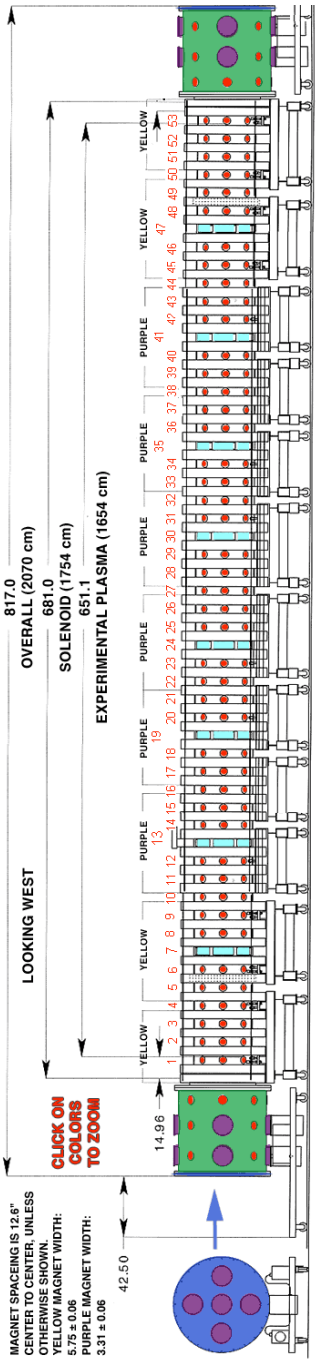

FIG. 2.2 Diagram of the upgraded LArge Plasma Device (the LAPD)[*] with port numbers labeled. Port 7, 13, 35, 41 and 47 are currently installed with a top rectangular port large enough for fast-ion sources and SAW antennas installation. Port 35 has a side-access rectangular port in addition.

[*] http://plasma.physics.ucla.edu/bapsf/pages/diag2.html

The LAPD has excellent access for probes and optics. There are 450 radial ports, 64 of which are rectangular quartz windows, allowing a nearly 360 degree view of the plasma in 8 locations along the machine length[1]. There are sixty rotatable "ball valve" flanges, which allow probe placement anywhere in the plasma volume between pairs of axial field magnets. Large devices can be introduced through the rectangular ports at seven locations using custom-built square valves.

Aside from the large size and excellent accessibility, the LAPD has other attractive features:

- Programmable confining magnetic field can be up to 3.5 kG with error less than 3%.
- Three portable cryo-pump vacuum stations and numerous gate valves for differential pumping when probes or other devices are moved in and out of the system without breaking vacuum.
- Computer controlled 2D stepping motors can move probes with 0.5 mm accuracy throughout the plasma column.
- Data acquisition system with 12 channels of 8 bit, 5 *GS/s* digitizers, and 32 channels of 14-bit, 100 *MS/s* digitizers.
- Plasma density diagnostics include a 56 *GHz* microwave interferometer for line-integrated density measurements and four newly-installed interferometers located at port 15, 23, 32 and 40.
- Fifteen Digital Oscilloscopes ranging from 2 channel-175 MHz/channel to 4 channel-2 GHz/channel, 6 Stanford digital delay generators (1 ps accuracy), 2 BNC 8 channel pulse generators (1 ns accuracy), 1 LeCroy arbitrary waveform

generator (10 MHz), 2 Agilent arbitrary waveform generators (80 MHz), HP 8568B spectrum analyzer, 3 LeCroy 1820A Differential Amplifiers/Filters, Agilent Network Analyzser (to 180 MHz), 2 four channel Tektronix-Sony 100 MHz optical isolators, 2 microscopes for probe construction (one with micro-manipulators).

2.2 Irvine Electron-Positron Chamber

The Irvine Electron-Positron chamber is located in the McWilliams Plasma Laboratory at UC Irvine. The machine was used for electron-positron plasma study by Dr. H. Boehmer because of its high-vacuum capability (down to 8.0×10^{-9} torr) with a Varian Turbo-450 pump system (Model: 969-9042). A photo of a typical setup of the chamber is shown in FIG. 2.3. Most of the developing and testing of the lithium fast-ion sources, including the initial activation of a lithium aluminosilicate source, the beam radial-profile and energy scan measurements, and other equipment checks for a coming LAPD run, are conducted in the Electron-Positron chamber.

The Electron-Positron chamber has been modified to a versatile test bed of equipment. The original chamber is about 15 cm in diameter and has three sections connected using conflat copper o-rings for excellent vacuum sealing. The total length is about 1.2 m. A 13 cm diameter stainless steel collector and a small 0.3 cm diameter rotary probe are mounted on top of the center section. The turbo pump inlet is connected to the bottom of the center section with a screen in between to protect the blades in the turbo pump. A new cross section is added to extend the original chamber. The newly developed lithium source re-coating device is currently installed in the cross. An aluminum square spool

similar to the rectangular port on the LAPD is connected with the cross through a KF-50 quick-disconnect valve. This spool can accommodate either the 0.6” lithium source or the RF source. There are two sets of water cooled magnets to provide a mirrored background magnetic field in the vacuum chamber if necessary. The magnetic field can be up to 2.4 kG at the center of the magnets and 1.2 kG at the center section with 100 A coil current.

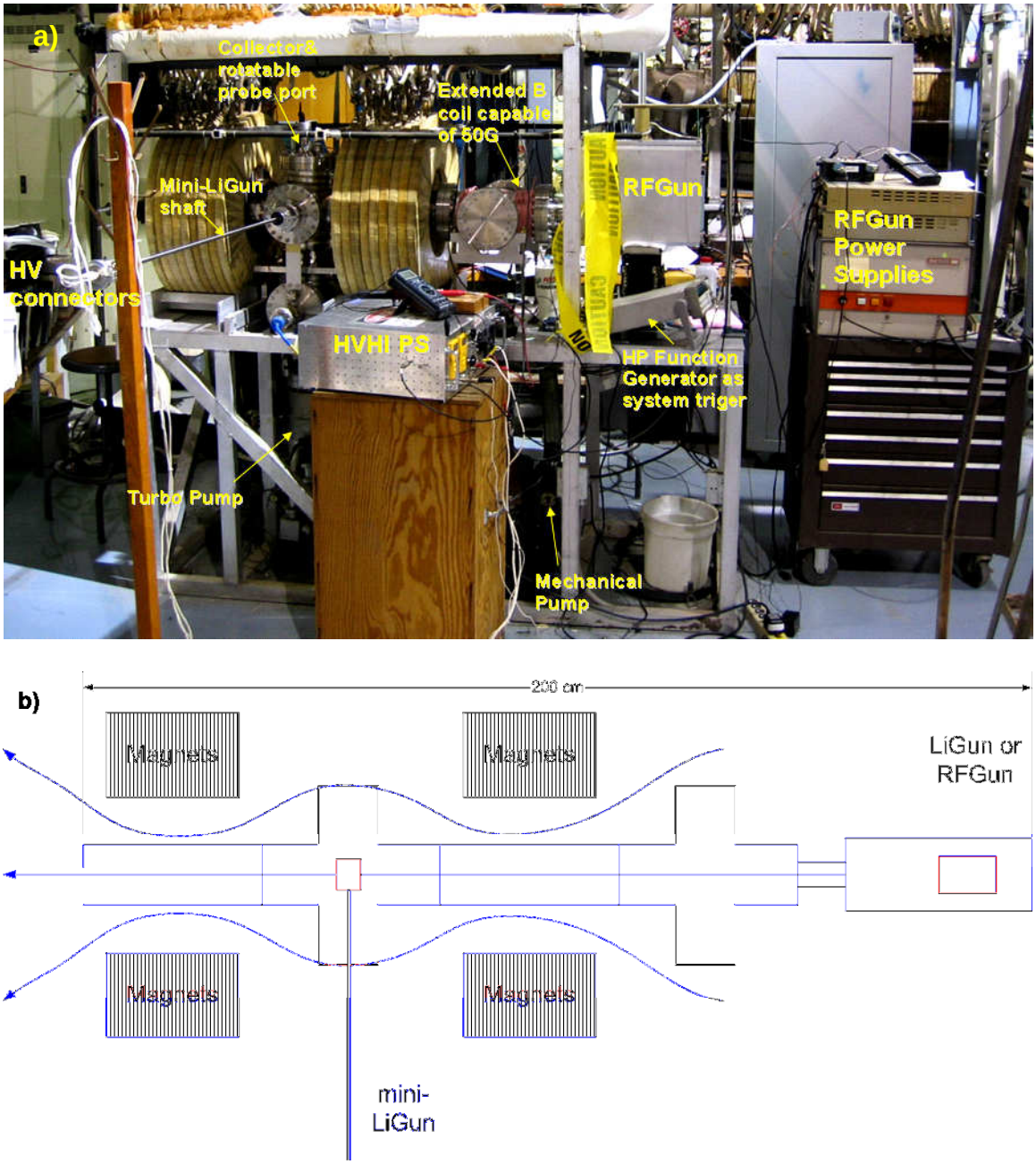

FIG. 2.3. Electron-Positron chamber of UC Irvine
a) Setup of UC Irvine Electron-Positron chamber with the RF fast-ion source in the square spool and the Mini-LiGun from side KF-50 port; b) Schematics of the Electron-Positron chamber.

2.3 Irvine Fast-ion Sources

The proposed investigations and the fact that the ion source has to be immersed in the plasma put severe constraints on the properties of the ion gun. An ideal source for this research should have these features (Table 1):

- Wide energy range (400 – 2000 eV) to investigate the energy dependence of the interaction;
- Low beam ion mass to be able to match the phase velocity of Alfvén waves in helium plasmas;
- Operation at magnetic fields up to 4 kG and at any pitch angle;
- Low beam divergence to make the beam observable over large distances;
- Small energy dispersion;
- High current density to facilitate diagnostics, but small enough to prevent collective wave excitation (test particle investigation);
- Small gas load;
- Source operation independent of plasma conditions (density, temperature, etc.);
- Small size to minimize the perturbation of the background plasma;
- No magnetic material.

Properties	FI source			Ideal source for FI experiments
	rf source	0.6 in. emitter Li source	0.25 in. emitter Li source	
Source type	Plasma type (argon)	Surface ionization (lithium)	Surface ionization (lithium)	No preference
Power input/type	20–100 W (~18.5 MHz)/ rf power	80–100 W (~11 A)/ dc power	12–22 W (~2.2 A)/ dc power	No preference
Physical size (in.) (Cross sectional)	~9.5×4.25 in.^{2}	~4×3 in.^{2}	~1.6×1.3 in.^{2}	Small to minimize plasma perturbation
Beam extraction	Screen (+50–600 V), accelerator (–100–600 V)	Emitter (500–2000 V), grid (–0–2000 V), second grid (floating)	Emitter (500–2000 V), first grid (–0–2000 V), second grid (floating)	Wide energy range (50–3000 eV)
Modulation type/purpose	Modulate rf power /to prevent source overheating	Modulate extraction biases /to preserve emitter lifetime and increase beam extraction	Modulate extraction biases /to preserve emitter life time and increase beam extraction	No preference
Beam profile	Adjustable, up to 3 cm max diameter	Adjustable, up to 1.5 cm max diameter	Adjustable, up to 0.6 cm max diameter	>0.32 cm diameter (size of a standard probe collector)
Beam current	2.0 mA/cm^2	1.0 mA/cm^2	1.0 mA/cm^2	~1.0 mA/cm^2
Beam energy/spread	<10%	<4%	<4%	<10%
Beam divergence	3°	~3°	~3°	<3°
Pitch angle	0–25°	20–90°	17–90°	0–70°
Ambient magnetic field	<1.0 kG	Up to 4 kG	Up to 4 kG	Up to 4 kG
Consumable	None	0.6 in. Li emitter	0.25 in. Li emitter	Economical
Maintenance	Remove coating on discharge chamber and grids	Replace emitter	Replace emitter	Minimal
Influence on LAPD plasma	Argon neutral leak	Minimal out gassing	Minimal out gassing	Modest to minimize neutral collisions
Influence by LAPD plasma	Neutralizing electrons aid fast ion extraction	Electron saturation current on emitter increases HVPS current load	Electron saturation current on emitter increases HVPS current load	Modest to maintain steady beam output

Table 1. Overview of fast-ion sources employed by the UC Irvine fast-ion group in comparison with the ideal source.

Initially in this program, a commercial argon ion gun from IonTech, featuring a RF discharge as the ion source, was modified for operation in the LAPD[2] and used to investigate classical transport[3] and for preliminary turbulent transport measurements[4] (Sec. 2.3.2). Although fairly reliable in operation, it could not be operated at pitch angles larger than 25^{o} and only at magnetic fields of ~ 1 kG or less. Furthermore, it has much reduced beam production with helium compared to argon, because the higher ionization potential prevents the formation of a sufficiently high plasma density in the source RF coil. A new fast-ion source with features compensating the RF source is necessary, and presumably with different mechanism in fast-ion generation.

2.3.1 Thermionic Lithium Aluminosilicate Ion Sources

Alternatives to plasmas discharges as charged particle source are the solid-state thermionic emitters. While they are widely used as electron emitters, they are used infrequently as ion sources because of their limited current density. Of particular interest as a thermionic ion emitter for the fast-ion program is lithium aluminosilicate (LAS). The type of aluminosilicate used in this article is Beta Eucryptite[5,6]. Apart from lithium, these ceramics are also available for other alkali ions: sodium, potassium and cesium. Because of their ceramic nature, these emitters are inert to atmospheric constituents at room temperature, but deteriorate in the presence of oxygen, vacuum oil, etc. at operating conditions (1000 – 1200º C).

LAS sources have been used before in plasma related experiments. A small gridded

lithium ion source was used to investigate ion drift orbits in the vacuum magnetic field of the Compact Auburn Torsatron[7]. Lithium ion and neutral beam sources, placed externally to the plasma chamber, are also used for optical and beam probe diagnostics in tokamak and stellarator configurations[8,9,10,11,12]. Since these sources are operated in the absence of plasma electrons and system magnetic fields, they can employ a Pierce configuration[13], which generates low emittance, high current density beams.

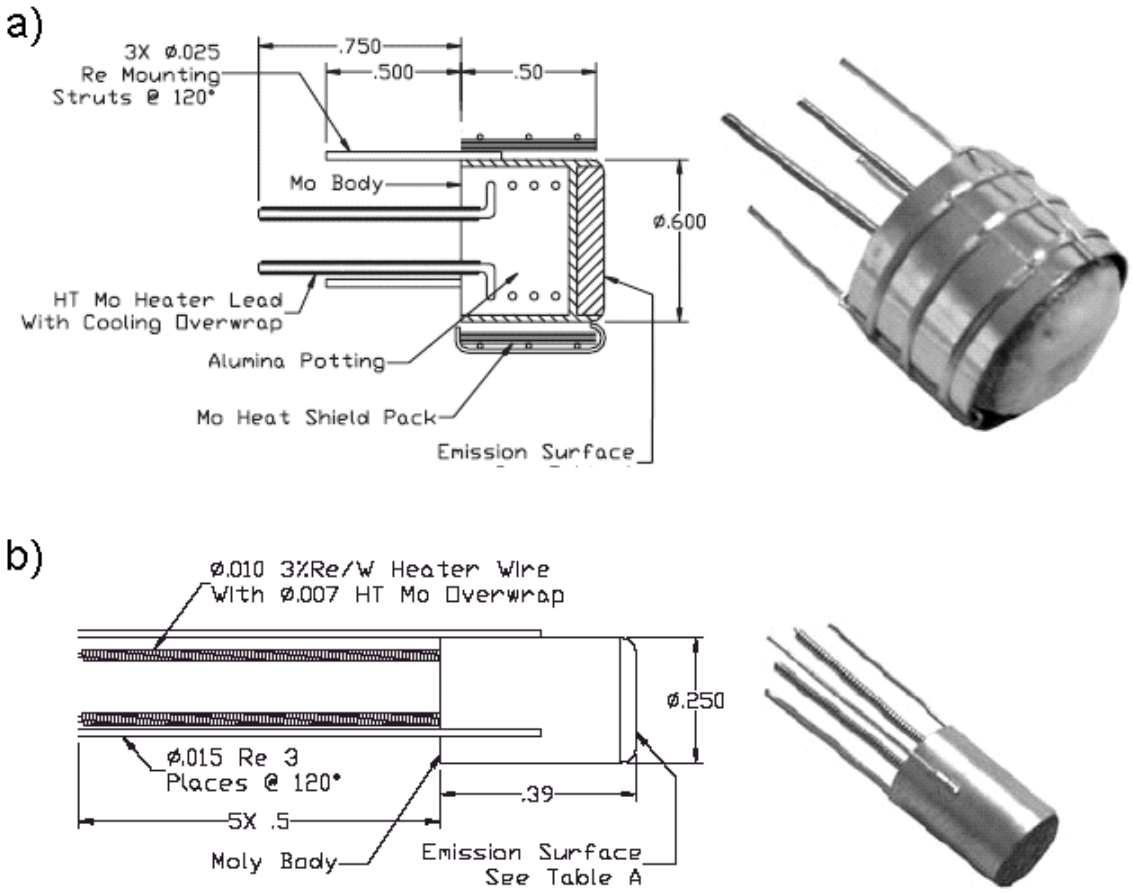

FIG. 2.4. Schematics and photographs of lithium ion sources from Heat Wave Inc. (a) Model 101142 0.6" Dia. Ion source; (b) Model 101139 0.25" Dia. Ion source. http://www.cathode.com/i_alkali.htm

A. Lithium Ion Source Design And Characterization

The Pierce geometry is the ideal configuration for charged particle sources since it has no beam perturbing grid structures. Unfortunately, it can not be used for the investigations of fast-ion behavior in plasmas because the background plasma constituents streaming into the gun will modify the vacuum electric field of the electrodes. In addition, the external magnetic field will modify the beam orbits within the large physical structure of a Pierce source. Therefore, a gridded gun configuration was chosen in which the emitter – extraction grid separation was small enough to render beam orbit modifications within the gun structure by $\mathbf{v}\times\mathbf{B}_0$ and $\mathbf{E}\times\mathbf{B}_0$ forces insignificant.

Two lithium ion guns with lithium aluminosilicate as thermionic emitters of different sizes (0.6" and 0.25" diameter, Heat Wave Inc.[14]) were designed, constructed and characterized at UC Irvine. Lithium emitters with typical isotope concentrations of 92.5% Li-7 and 7.5% Li-6 are chosen for testing the fast-ion sources. Li-7 isotopically purified emitters are used for the fast-ion transport experiments (Chapter 3). The cross section of a generic lithium ion gun is schematically shown in FIG. 2.5. The actual configurations are scaled to the two different emitter sizes (Appendix C). While the gun with the 0.6" emitter is the prototype, the smaller gun was developed to decrease the perturbation of the LAPD plasma by the gun housing and to be able to use standard 50 mm diameter vacuum interlock valves of LAPD. Both guns were tested first in the Electron-Positron chamber's ultrahigh vacuum environment.

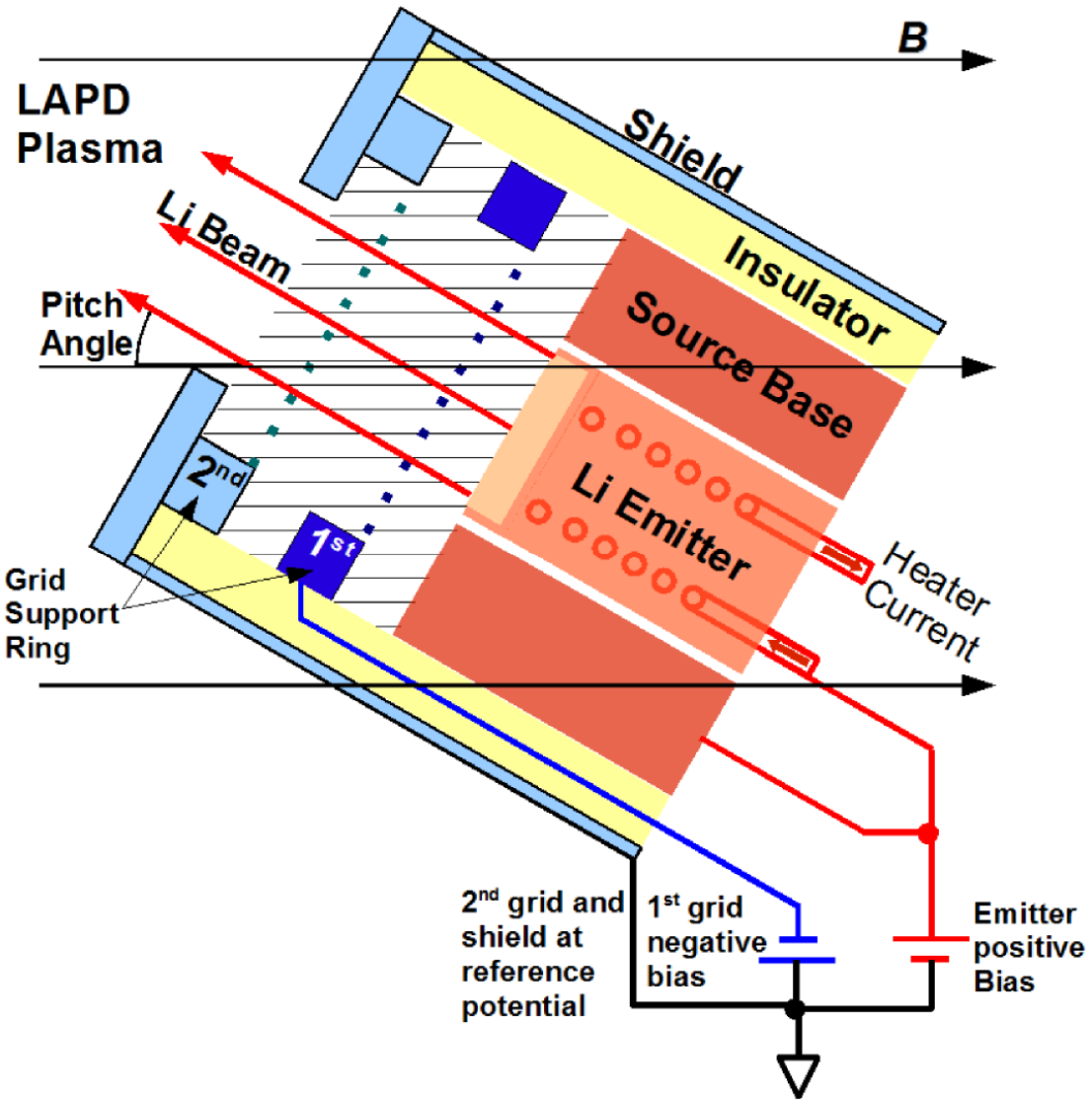

FIG. 2.5. Cross sectional view of a generic lithium ion source in the LAPD plasma at a pitch angle of 30˚.
Shaded area corresponds to the beam extraction region, which is also the domain used to simulate the field line configuration in FIG. 2.10.

Since the ion emission from LAS is not purely a thermally activated process but can be enhanced by an external electric field (Schottky effect), it is desirable to have a high potential difference between the emitter and the first grid. Therefore, to produce sufficient beam currents even at low beam energies, an acceleration–deceleration strategy is employed where the emitter is biased positive (with respect to the gun housing and the second grid) to the desired beam energy while the first grid is biased to an appropriately high negative potential. Measured by a laser beam, the optical transparency of the grid-system poses an upper bound for the beam transmission efficiency (collection current/emission current). Strong field line distortions or space charge effect will cause the beam transmission efficiency to decrease from the optical transparency.

The ion guns are first tested in the Electron-Positron chamber, usually without the presence of a plasma to neutralize the beam space charge. The distance from emitter to exit, respectively, is 1.88 cm for 0.6” emitter source and 1.45 cm for 0.25” emitter source. During vacuum operations, it was observed that the collector and the probe have to be within a few centimeters from the source exit to measure the beam current. As indicated in FIG. 2.2 a), a collector plate, a radial rotary probe and a Faraday cup are all installed on the top flange of the center section. The probe can be rotated manually to cross the center of the beam for measurement, or kept away from the beam while using the collector or the Faraday cup.

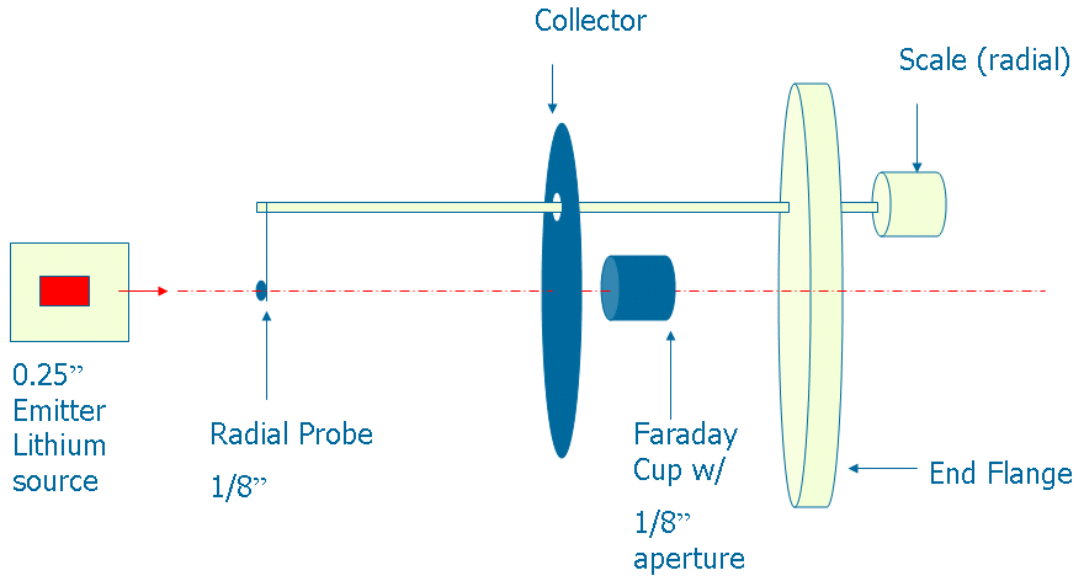

FIG. 2.6. Beam diagnostics installed in the Electron-Positron chamber.

To test the basic performance of the ion guns, the emission current was monitored as a function of emitter temperature as measured by an optical pyrometer viewing the emitter through a quartz vacuum window at one end of the Electron-Positron chamber. The emissivity of the emitter surface, assuming ε = 0.8, could cause ~ 65 ºC of temperature underestimate. In this work, the emitter temperature is recorded without emissivity corrections and serves as a relative indicator of beam current performance.

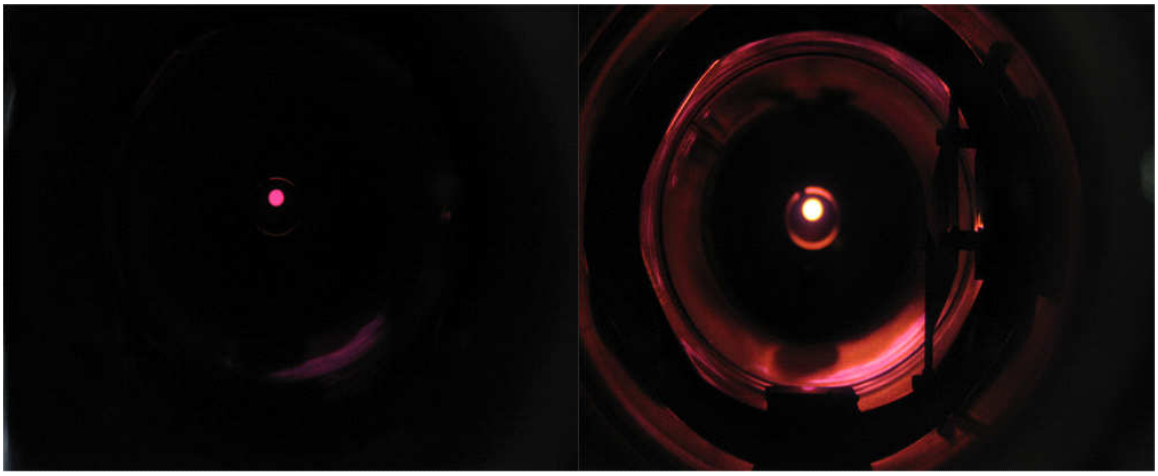

FIG. 2.7. Photograph viewing from Electron-Positron chamber end port.
0.6” emitter lithium source heater on: 5.0 V, 8.4 A (left) and 5.68 V, 9.24 A (right).

For the 0.6” emitter at 1150 ºC and biased to 2 kV, the observed current is 2 mA which corresponds to a current density of 1 mA/cm^2. Because the 0.6” diameter beam is more than sufficient for this fast-ion transport investigation, to achieve a better spatial resolution, this gun is usually operated with a 5 mm diameter circular aperture. The secondary electron emission from the 1st grid is measured to be less than 1% of emission current, which causes less than 10% of ion transmission overestimate. With two 40 lines per inch (lpi), 91% transmission Molybdenum grids, the optical transparency is 81%. FIG. 2.8 compares the emission current and the current to an outside collector (2.5 cm from the emitter) as a function of extraction voltage with the emitter temperature at 1050 ºC. The space charge limit at 1000 V of extraction voltage is ~200 μA, which indicates that most of the current levels are limited by thermionic emission instead of space charge effect. On average, near 80% of the ion beam is transmitted through the grid holes with the acceleration voltage above 500 V. Positioning the gun axis at an angle of 45^o with respect to an external magnetic field of up to 4 kG did not result in a change of emission current. FIG. 2.9 (a) shows the beam cross-section 5 cm outside the gun in the UC Irvine chamber, using a 3 mm diameter disk collector, demonstrating good beam optics. It should be noted that in FIG. 2.9, the emitter current was intentionally kept low at (a) ~ 0.1 mA and (b) ~ 10 μA to reduce radial space charge modification of the beam profile. In FIG. 2.9 (b), the beam radial profile is still widened by ~ 10% from the radial expansion.

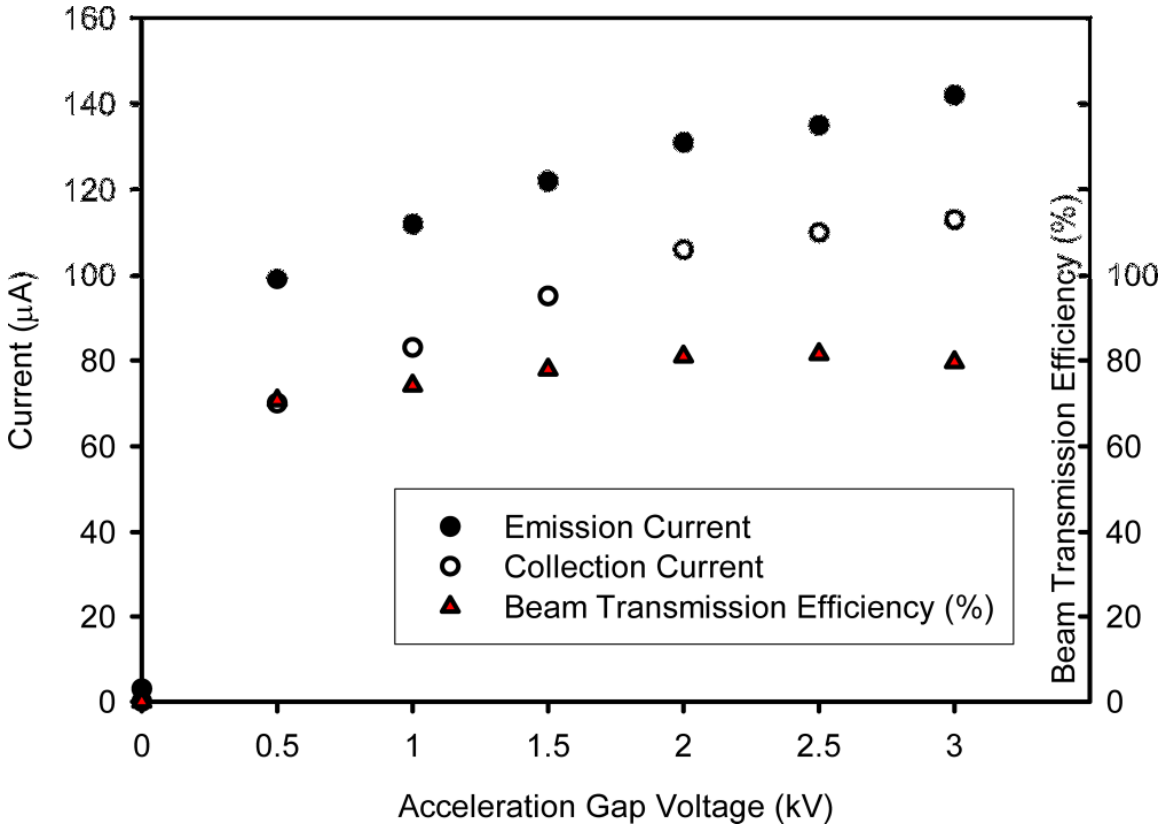

FIG. 2.8. 0.6" emitter gun emission and collection current versus acceleration gap voltage.
Beam transmission efficiency is calculated for each pair of current levels. (Total grid optical transparency is 81%.)

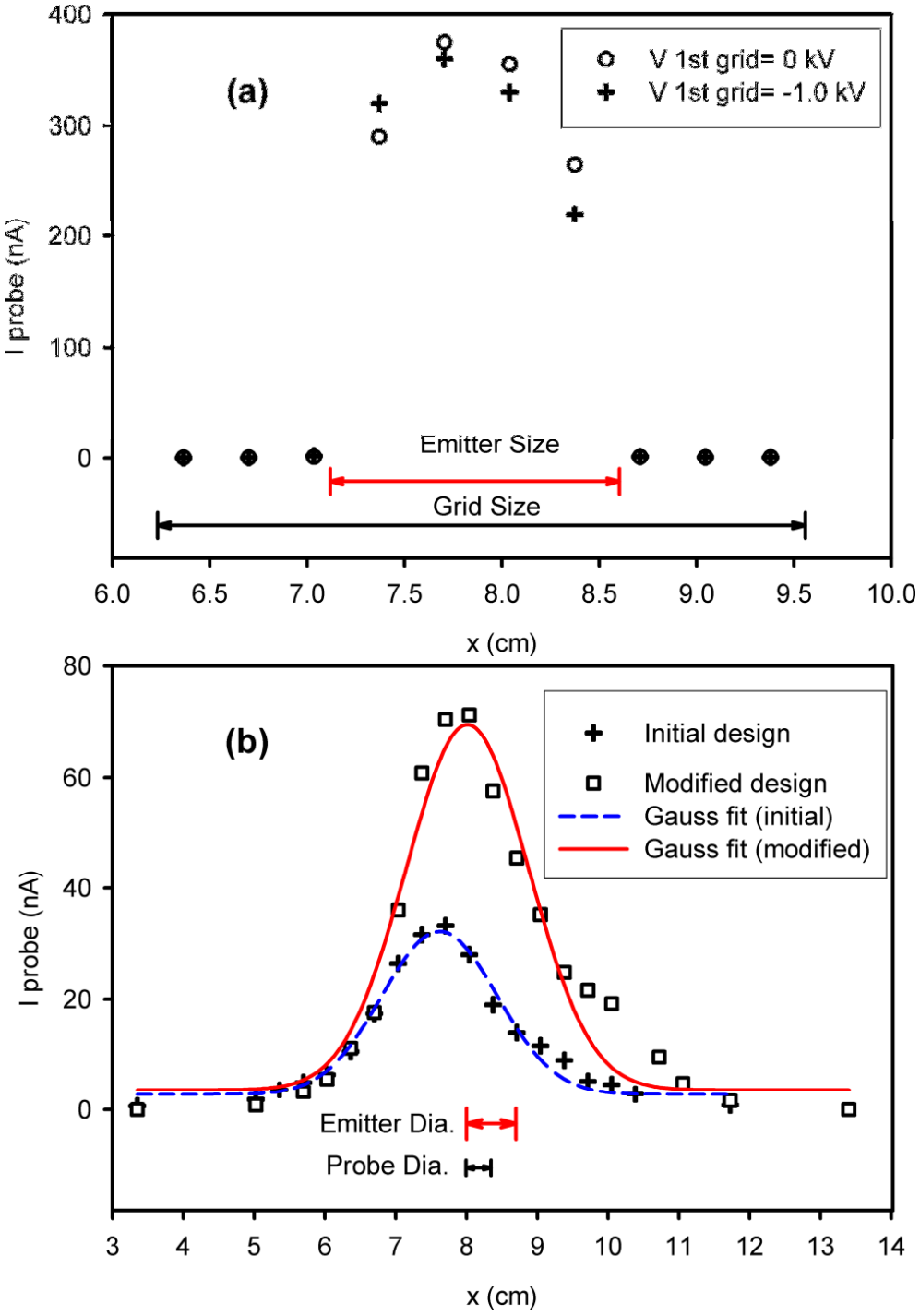

FIG. 2.9. Emitted beam profiles of lithium sources.
(a) 0.6" emitter gun beam profile across beam center collected 5 cm away from the beam exit. Profiles are taken with +2.0 kV emitter bias and 1050˚C emitter temperature; (b) Comparison of 0.25" emitter gun beam profiles before and after modifying 1st grid structure. Profiles are taken with +600 V emitter bias, –100 V 1st grid bias and 1050˚C emitter temperature.

Distortion of the ion orbits within the gun structure can be caused by the fringing fields at the edge of the emitter and the grid support rings as well as by equipotential surface deviations from being strictly parallel in close vicinity of the grid wires. These effects are more prevalent for the small diameter emitter. Furthermore, care must be taken to place insulating structures in such a way that accumulated charges will not distort the field. To visualize the electric field pattern within the actual gun structures, the Femlab software (COMSOL, Inc.) is used to calculate the 2D equipotential lines in cylindrical coordinates and estimate the space charge effect (FIG. 2.10 (a), (b) and (c)). The models' boundary conditions are set at typical operating conditions. Since Femlab lacks a poisson solver, the space charge effect of the beam is estimated by imposing uniformly distributed space charge along the beam path. A 0.1 mA/cm^2, Li ion beam at 600 eV energy corresponds to a reference charge density of ρ_0 (7.23×10^{-6} C/m^3). A potential barrier comparable to the beam energy does not appear in the source until the imposed charge density is increased to $100\rho_0$. It can be seen that for the 0.6" emitter gun (FIG. 2.10 a) the fringing fields and the field distortions around the grid wires are minimal. Since this ion gun is usually operated with a 0.5 cm aperture, sampling only the center part of the beam, it produces a high quality beam. In contrast, the 0.25" emitter gun, where, to reduce edge effects, the emitter – grid spacing was reduced from 2.50 to 1.25 mm, these effects are more severe. FIG. 2.10 b) shows the field pattern for the 0.25" emitter gun initial design using a 40 lpi first grid. Because the grid is much closer to the emitter, the equipotential lines are greatly distorted around the grid wires, compared to FIG. 2.10 a) where the same grid size but a larger spacing was used. In addition, in the deceleration stage, the fringing field in the grid support ring reaches to the center of the

beam. As a result of both effects, the radial beam profile for this gun is wider than the emitter diameter (FIG. 2.9 (b)) and the transmitted beam current is greatly reduced (~ 30% of emission current). To improve the beam quality, a 90 lpi first grid was installed and an additional 40 lpi grid was installed on the opposite side of the grid support ring with a wider aperture (0.40" I.D.). The improvement of the field pattern is evident from FIG. 2.10 c). Although the radial distribution of the beam (FIG. 2.9 (b)) is similar, the transmitted beam current doubles with the modified design, in spite of the total optical transparency dropping from 81% to 64%. The beam transmission efficiency is also improved to be ~ 49 – 66 % (uncertainty caused by possible secondary electron emission) that is comparable to the optical transparency.

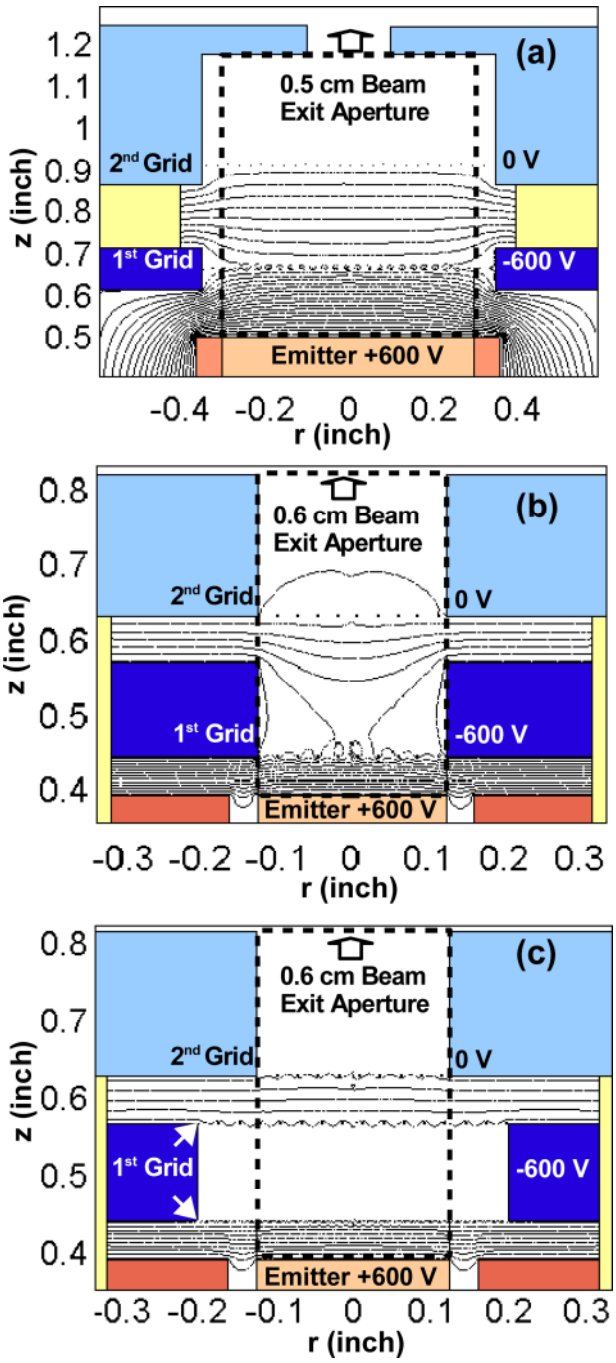

FIG. 2.10. Electrostatic potential lines calculated according to different gun configurations.
(a) 0.6" emitter gun; (b) 0.25" emitter gun initial design with a single 1st grid next to the emitter; (c) 0.25" emitter gun modified design with two 1st grids biased negatively. Cylindrical symmetry is assumed in simulations and all grid sizes are to scale (may appear to be a single dot). Dashed boxes show where space charge is uniformly distributed along the beam paths. Simulations are powered by Femlab (COMSOL, Inc.).

The large diameter planar collector that measures the total emitted beam current was used to acquire the energy distribution of the beam by taking the derivative of the collected current with respect to the collector bias. FIG. 2.11 gives examples of the beam energy distributions for the 0.25" emitter gun. The width is about 4% of the beam energy without deconvolving the energy resolution of the collector[15]. For these LAS emitters , the actual energy spread of a near zero energy beam is given by a Maxwellian distribution determined by emitter temperature, which is about 0.25 eV. The low energy tail of the distributions, becoming more prominent with increasing beam extraction voltage, is likely due to the field line deviations from directions perpendicular to the emitter, e.g. those around the wires of the extraction grids, as well as increased resolution width of the collector at higher beam energy.

From these results it is evident, that great care has to be taken in the design of gridded guns for good performance, and that the equipotential surfaces in the acceleration and deceleration stages of the gun should deviate from planes as little as possible since these field errors influence both the energy spread and the divergence of the beams. Edge effects can be minimized by extending the parallel planes defined by emitter and first grid to larger radii. In the acceleration stage, this is accomplished by providing a shield structure around the emitter and by the grid support ring. In the deceleration stage, again to provide flat equipotential planes, extra grids are sometimes necessary even though they decrease the total optical transparency.

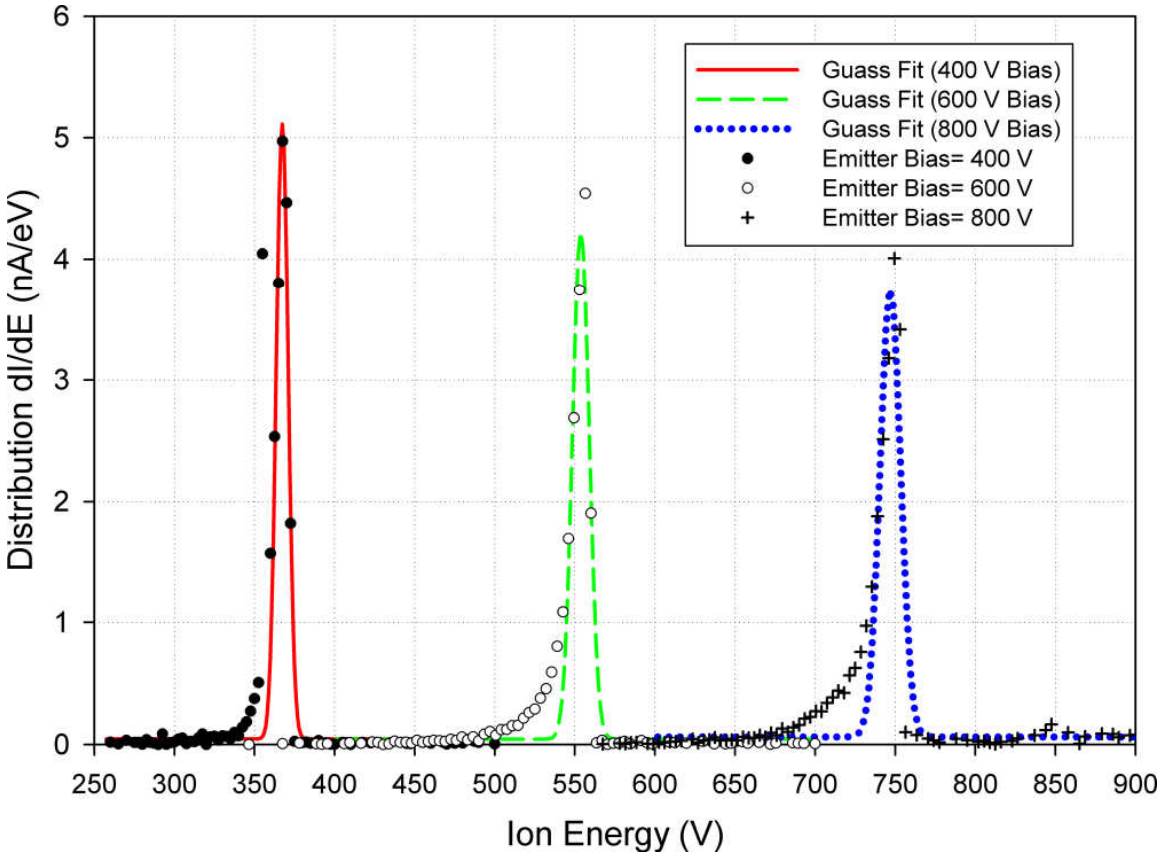

FIG. 2.11. Energy distributions from 0.25" emitter gun with different emitter biases. Data taken with – 100 V 1st grid bias and 1100 ˚C emitter temperature.

With a specially fabricated power supply (Appendix C) for high voltages and heater current, the ion guns can be operated either in the DC mode or pulsed at the 1 Hz repetition rate of the LAPD plasma using a minimum 15 ms pulse length. From the experience of operating the larger gun at LAPD, the emitter lifetime was found to be about 20 hours for an average beam current density of 1 mA/cm^2. In a high vacuum environment, the lifetime is considerably longer according to Heat Wave Labs, Inc.

B. Operation Of Lithium Sources In The LAPD

The introduction of the lithium fast-ion sources into the LAPD machine is a time consuming process, mainly due to the out gassing of the heater. The lithium sources are transported to UCLA with freshly replaced emitter pre-installed. Several layers of tight bagging are convenient to prevent excessive water vapor during transportation. Taking # 35 side rectangular port on the LAPD as an example, 0.6" emitter source is first mechanically installed on the spool, pumped down to ~ 5 x 10^{-6} torr using a cryo-pump system in about two hours. Then the source needs to be out gassed at ~ 5.0 A and monitored by an RGA for H_2O partial pressure since oxygen is a major poison for the LAPD cathode. The H_2O partial pressure will first rise up then drop down to ~ 6 x 10^{-6} in another two hours before opening the gate valve. It is advisable to coordinate the whole process with other activities for efficiency.

Supported by stainless steel tubes that also carry the heater and high voltage cables, the ion guns are placed into the LAPD vacuum chamber at various points along the axis of the system. Differentially pumped chevron seals allow radial motion and rotation of the guns without vacuum leaks. The ion gun and power supply system can be separated electrically from the vacuum chamber ground. This allows the ion gun to float at the plasma potential, decreasing the perturbation of the plasma by the ion gun housing. The plasma – ion gun configuration at LAPD is shown schematically in FIG. 2.12.

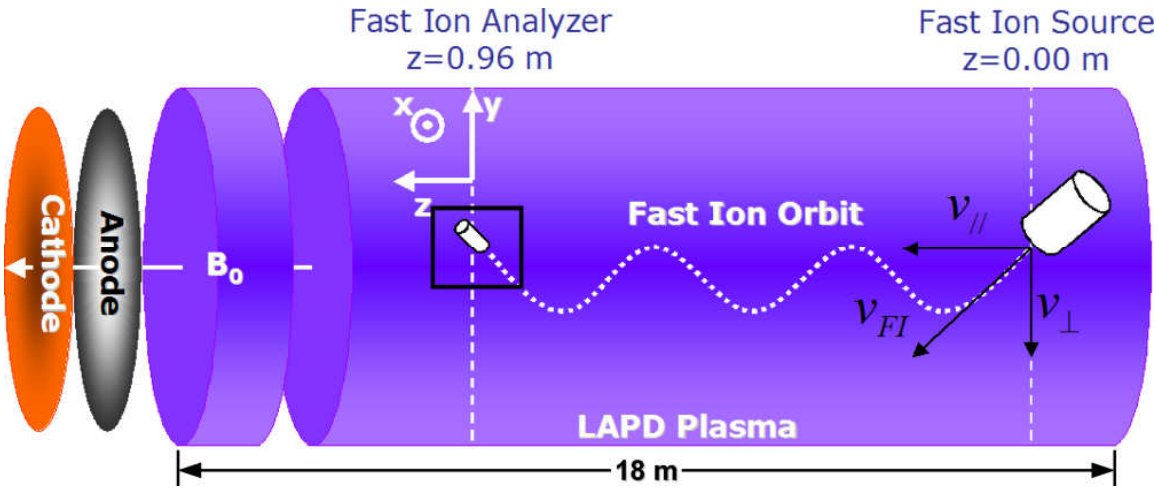

FIG. 2.12. Fast-ion experimental configuration in the LAPD plasma (schematic). Figure shows that fast ion completes three cyclotron orbits before being collected by the fast-ion analyzer three ports away from the source (0.96 m). The analyzer scans in x-y plane for beam spatial profile.

Operation of these ion guns inside a plasma environment has pros and cons compared to operation in a vacuum field chamber. In the LAPD plasma, the beam with the maximum current output is charge neutralized by the plasma electrons since the plasma charge density, even during the afterglow, exceeds that of the beam by three orders of magnitude, which is an obvious benefit for the fast-ion beam orbit studies. There are also issues to be aware of when the source is immersed in a plasma. Firstly, since the ion sources are often floated to reduce plasma perturbation, the exiting fast-ion energy is referenced to plasma floating potential, which is subject to change of plasma conditions. For example the floating potential in the discharge is ~10 V higher than that in the afterglow, which causes ~10 eV of difference in beam energy given identical extraction grid biases. Secondly, because the emitter is at the positive beam voltage and because the grid holes, for any useful plasma density, are large compared to the Debye length, plasma electrons can reach the emitter electrode of the ion gun. For operation in the afterglow phase of the LAPD plasma, this just adds a few mA to the load of the high

voltage power supply, but otherwise does not impair the function of the ion gun. On the other hand, during the high-density discharge, this current becomes excessively large. In this case, the ion gun must be positioned at a sufficiently large pitch angle so that the plasma electrons, tied to the magnetic field lines, are prevented from reaching the emitter, which is schematically indicated in FIG. 2.5.

C. Experimental Determination of Lithium Isotope Concentration

The natural abundance of lithium-7 is 93%, with the remaining fraction to be lithium-6. HeatWave Labs Inc. claimed their isotopically purified lithium-7 sources reach 99.99% grade of purity. To be objective about this number, a separate experiment was conducted to determine the bottom line of the lithium-7 purity in a commercial 0.6” Dia. lithium-7 source—using the LAPD as a large mass-spectrometer chamber (data set indicated in Appendix B).

The plasma-fast-ion parameters are based on the Doppler resonance case (III) used in Chapter 2. At first, a theoretical calculation predicts a ~ 90º difference in the collected gyro phase between the Li-7 peak and Li-6 peak. The typical beam spread along the gyro direction is ~ 40º, which means a weak Li-6 peak would has negligible effect on the main Li-7 spot. Then in the experiment, a Li-7 spot is scanned with B_0 = 1200 G, followed by another scan with B_0 changed to 1110 G, which would move the Li-6 spot, if any, to the center of the same grid. The lithium source is pulsed on for ~ 20 ms with a initial rising time of ~10 ms and a eventual decaying time of > 50 ms.

The data with the flat-energy duration (FIG. 2.13 b) of the lithium source pulse shows

> 91% purity. Averaged fast-ion net signal over the flat-energy time slot and the area of the beam spot is calculated for 1200 G and 1110 G data. The 1200 G data show a strong Li-7 spot as expected with the correct energy; the 1110 G data has a strong influence from the Li-7 spot with lower beam energies (~ 575 eV) but a weak Li-6 spot does show up towards the end of the flat-energy duration.

The slow decaying duration of the emitter bias is very useful for calibrating the fast-ion energy, as shown in FIG. 2.13 a). Fast-ions traveled different numbers of gyro-cycles with different initial energies at the collection plane, which corresponds to multiple peaks shown in a). The energies of the peaks and the theoretical gyro-cycles match in FIG. 2.13 c), which facilitates the identification of a lithium-6 center. This technique yields a lithium-7 purity estimation of 97 $\pm$ 1.5 %.

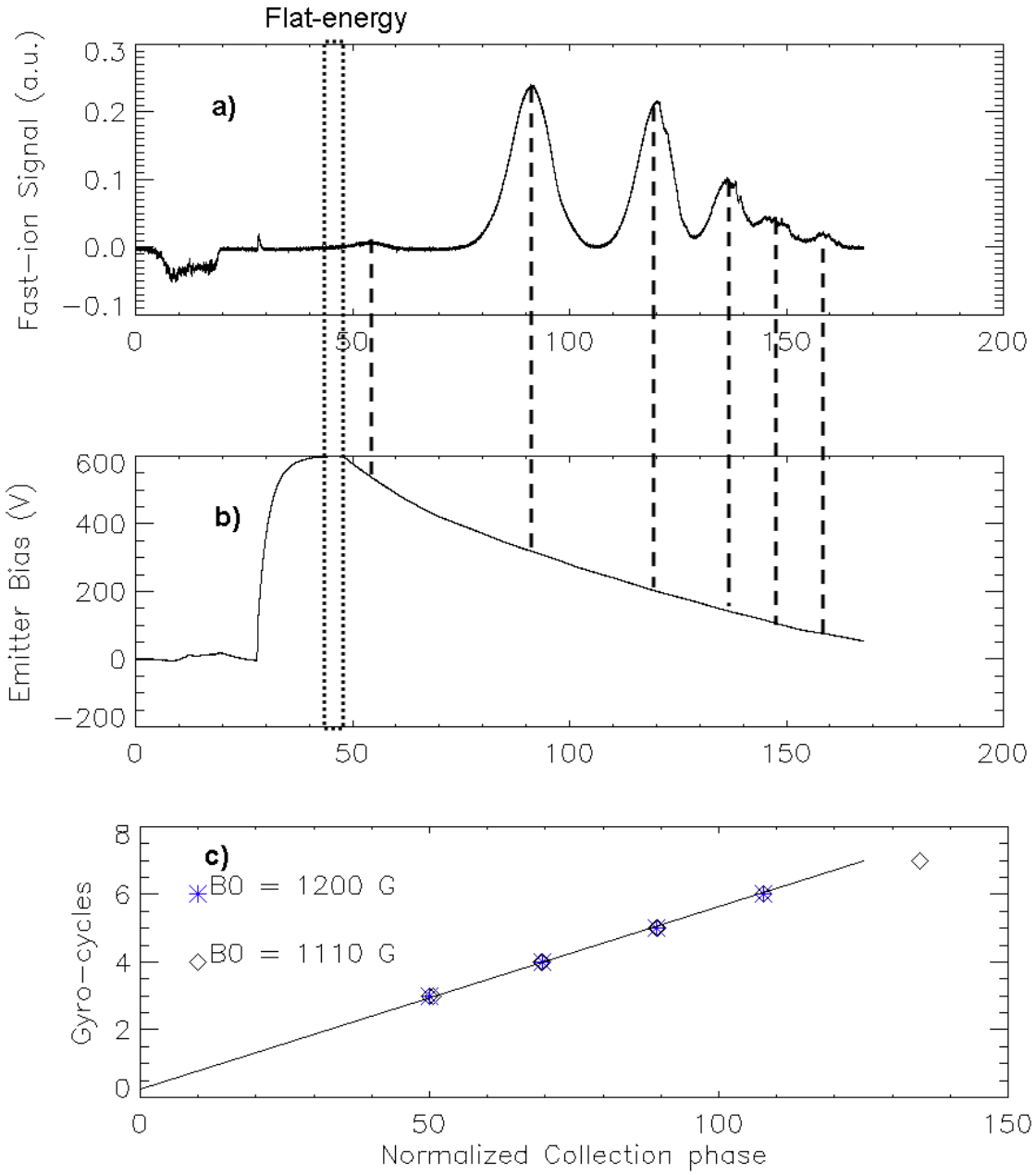

FIG. 2.13. Experiment for lithium-7 isotope purity.
(a) Fast-ion signal with multiple energy beams during the bias decaying time; (b) Emitter bias corresponding to the beam instant energy; (c) calibration using fast-ion beams traveled various numbers of gyro-cycles before collection.

D. Lithium Aluminosilicate Source Re-coating Project

Due to the finite source life time (~ 20 hrs) and high price marks (> 1100 $ for a new 0.6” Dia. Source), options were researched for alternatives, including having Heat Wave Labs Inc. “re-imp” (company preferred jargon for re-coating) the depleted sources, and a project to perform re-coating in the Electron-Postron chamber at UC Irvine.

Heat Wave Labs Inc. offers ~ 50% discount if a depleted source is sent and re-coated there. The Sep. and Dec. 2007 LAPD data run proved the similar lifetime for the refurbished sources. During a data run, it is important to have two refurbished sources ready before the experiment. The Dec. 2007 run did require the back-up source since the first one had a grainy emission surface that caused excessive beam divergence. Before requesting a re-coating from the company, it is recommended to remove the depleted material (Dremel tools) before sending the package and to emphasize “polish emission surface at best effort”.

An independent heating device was designed (Appendix C) and installed in the Electron-Positron chamber. The goal is to uniformly heat up the raw lithium aluminosilicate powder (Heat Wave labs Inc. #101151-05) in the container of an empty lithium 0.6” emitter. The original heater inside the source and an auxiliary tungsten heater are used to increase the sample temperature to 1200 – 1300ºC. The closeness of the melting temperature and the boiling temperature of the powder makes it critical to maintain the temperature within the small gap. Once one fill of the powder is melted down to form a glassy structure as preferred, the whole device is cooled down slowly

over a two hour range to prevent cracking of the glassy structure. Another fill is repeated by the same process until the whole cap of the emitter is filled with fresh emission material. A method to grind the surface flat is needed in the near future before completely relying on this re-coating technique.

E. Calibration of a Time-of-Flight Neutral Particle Analyzer—Another Application of the Lithium Fast-ion Source (0.25” Dia.)

The energy calibration of a time-of-flight (TOF) diagnostic (Wayne Harris) implemented on the Irvine Field Reversed Configuration (IFRC) was accomplished with the 0.25” Dia. Lithium fast-ion source (mini-LiGun). The purpose of the TOF diagnostic is to obtain an energy distribution function from charge-exchanged neutral hydrogen. The diagnostic includes a 13cm radius slotted disk rotating at 165Hz in vacuum which chops the emitted neutrals at a rate of 26 kHz. In-situ timing verification was performed with a DC xenon discharge lamp with an uncertainty less than 100ns for a 38μs chopping period.

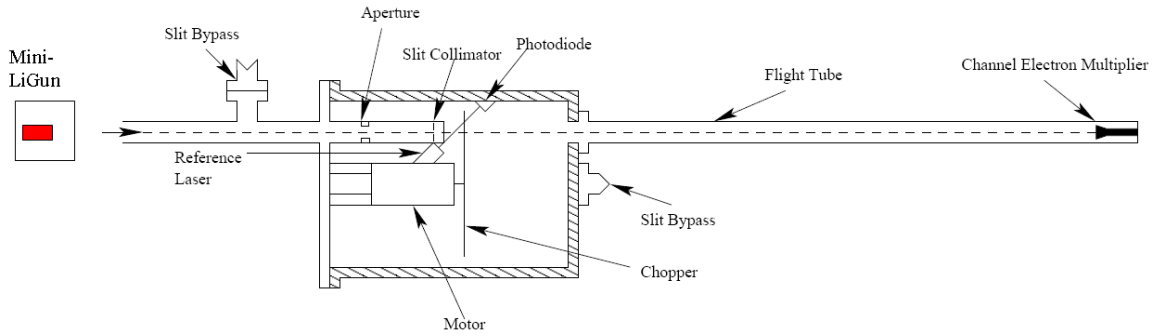

FIG. 2.14. Illustration of the mini-LiGun and the TOF diagnostic

Using a 500V emitter bias for the source, energy of 500eV was assumed to be correct

to calculate the slot open time. The lithium source produces a beam current of 0.1-1mA/cm2, which corresponds to a maximum of 1.8×10^{15} ions/s. Taking into account the beam divergence of 3º and the flux reduction due to the slit geometry, the maximum expected ion rate was around 9 ions/µs. The measured count rate was low enough to detect individual particles. A sample shot is shown in FIG. 2.15.

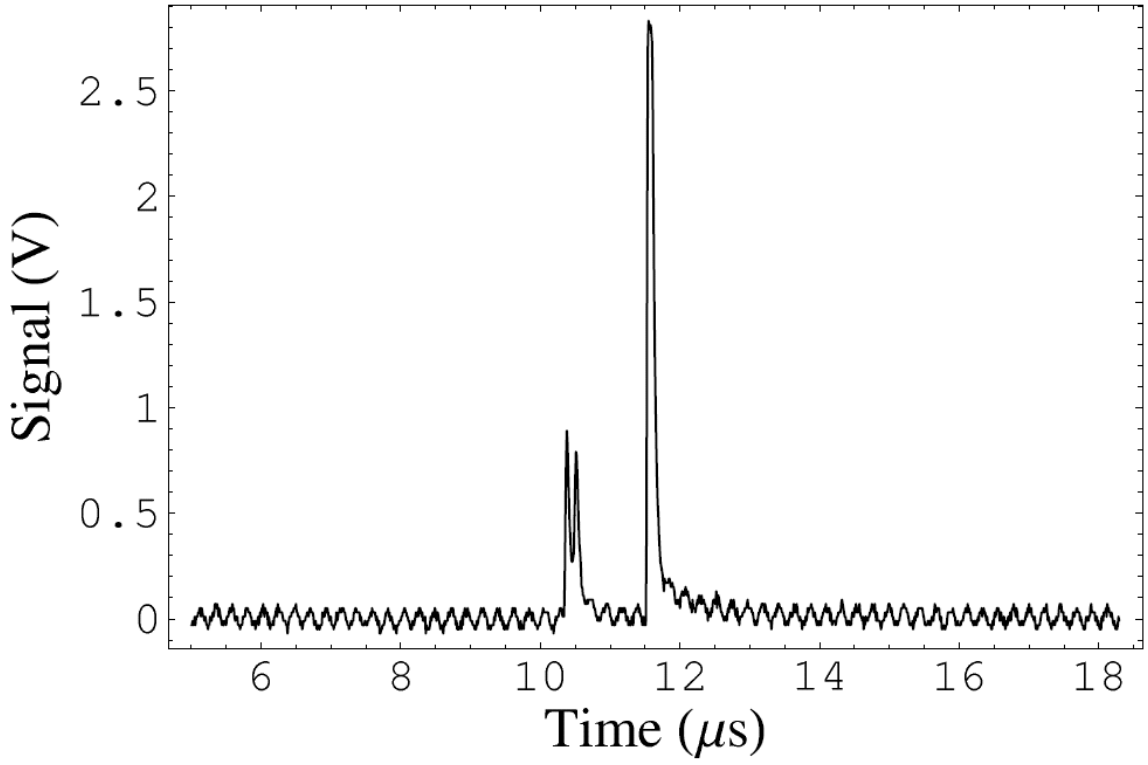

FIG. 2.15. Individual Pulses from lithium ion source.
Emitter Bias 800V, Chop Frequency 26 kHz

The ion source bias voltage was varied from 300V to 1500V for an energy scan. The oscilloscope was triggered off of the TTL signal generated from the reference laser and the pulse times were all measured from the point at which the signal was 5% of the maximum on the leading edge. For the data shown in FIG. 2.16, the delay between the reference laser and the average pulse position was measured for a 500V emitter bias on the ion source. The delay between the slot open time and the reference laser signal was

used to calculate the slot open time for various ion energies as the emitter bias was scanned. The standard deviation of the 500V bias data was 1.06μs and can be attributed to the finite slit open time. As shown, the fitted line of the averaged data differs from the expected energies by only 2%.

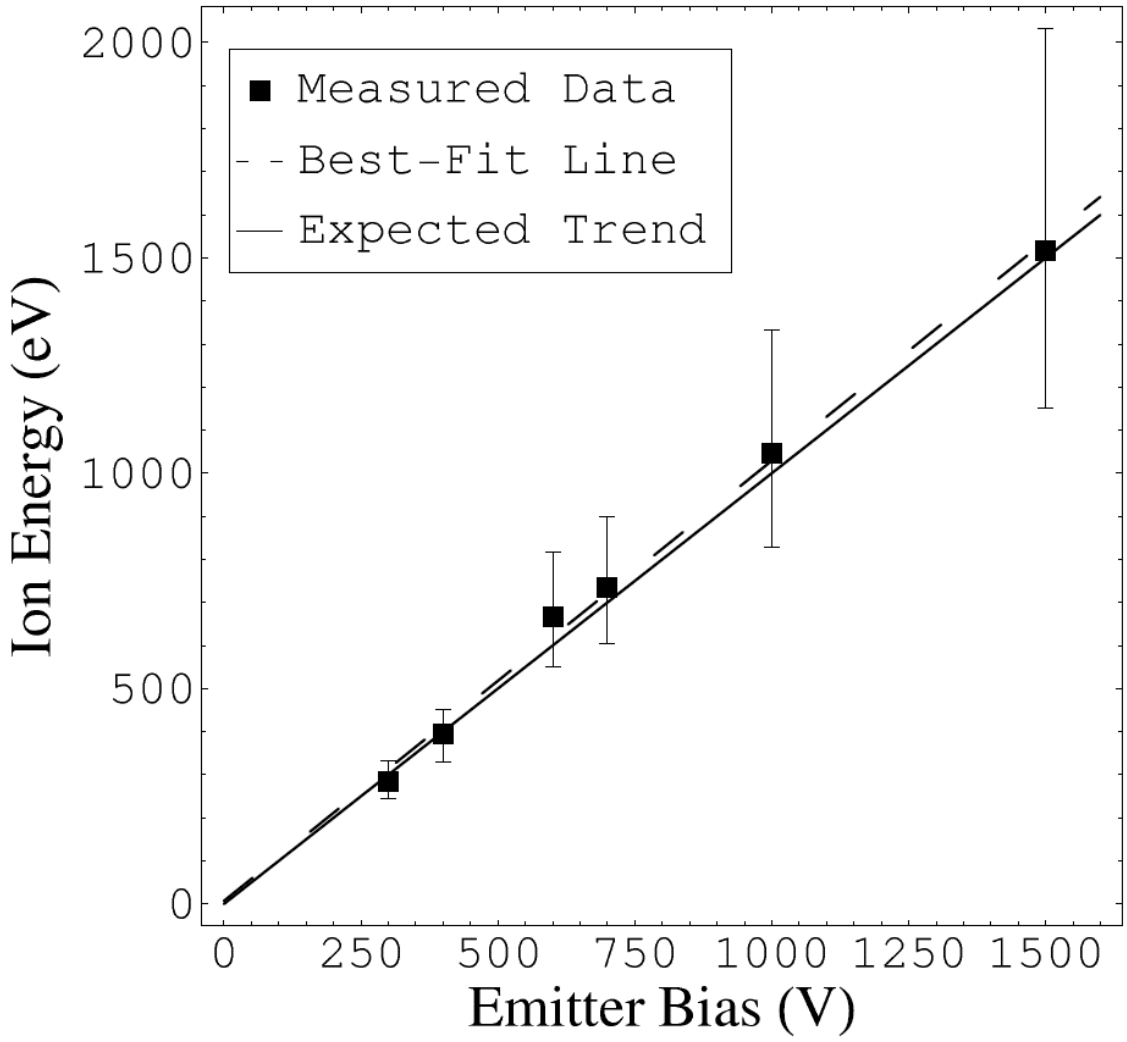

FIG. 2.16. Lithium ion energy scan.
Expected trend (solid) represents a 1:1 correspondence between ion energy and emitter bias. Best-fit line (dashed) falls within error bars. Error bars calculated by the deviation from the mean at each bias voltage.

To determine the lithium energy distribution function, 650 pulses were sampled at an 800V emitter bias and binned according to the time difference between the reference laser

and the arrival time as shown in FIG. 2.17. The expected flux from a drifting Maxwell-Boltzman distribution with peak energy of 800eV and temperature of 60eV is shown for comparison, in addition to data taken from the biased planar collector in the Electron-Positron Chamber. The Maxwell-Boltzman distribution and the collector data have both been transformed to the time-domain and convoluted with the aperture function in order to compare with the TOF data. As discussed earlier, the 60 eV empirical beam temperature is largely due to the resolution of the diagnostics—the TOF or the collection plate. The theoretical initial temperature of the lithium sources are still around 0.25 eV determined by the surface temperature.

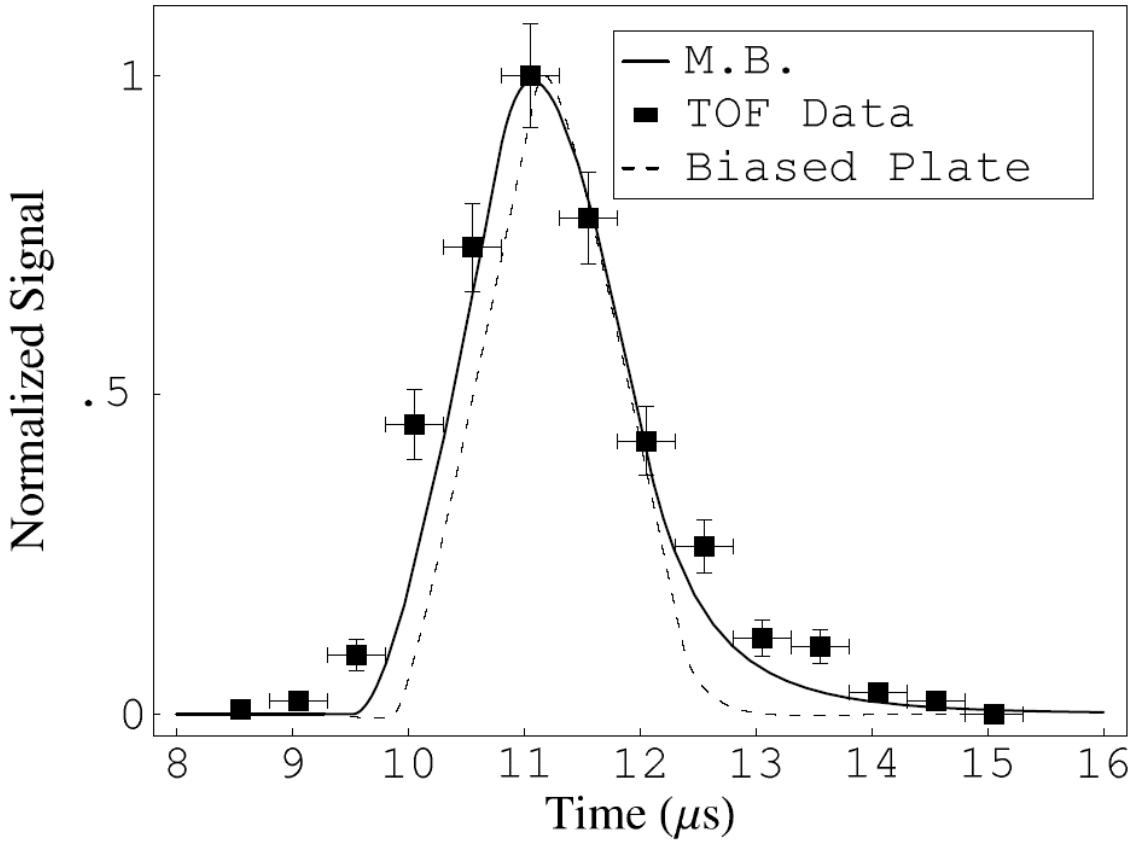

FIG. 2.17. Lithium ion distribution function.
For 800V bias in time domain as measured by TOF diagnostic (boxes) where data are binned into 500ns intervals. Maxwell-Boltzman distribution comparison (solid) with 60eV temperature and 800eV drift convoluted with aperture function and compared with convoluted data from ion beam energy distribution from FIG. 2.11.

2.3.2 3-cm RF Ion Source Modification

The 3-cm RF fast-ion source used to have the vacuum feedthroughs on Teflon o-ring seals, which developed a critical leak during an LAPD run. The final solution was to replace the bottom of the cylindrical chamber for matching capacitors next to the RF coil with a detachable flange (Appendix C). Four feedthroughs including a Swagelok for gas feed are welded on to the flange. The original three capacitors are enclosed in the cylindrical chamber with replaceable o-rings on both the front and the bottom flange. A new RF matching efficiency curve (P_{forward} / P_{total}) is shown in FIG. 2.18, with best efficiency up to 95% at ~ 20 MHz frequency. The RF source has its own features as been able to operate at 0 to 20 degrees pitch angle and high throughput (> 10 mA ion current) which is suitable for proposed test-particle Landau resonance experiment in the future (Sec. 5.3).

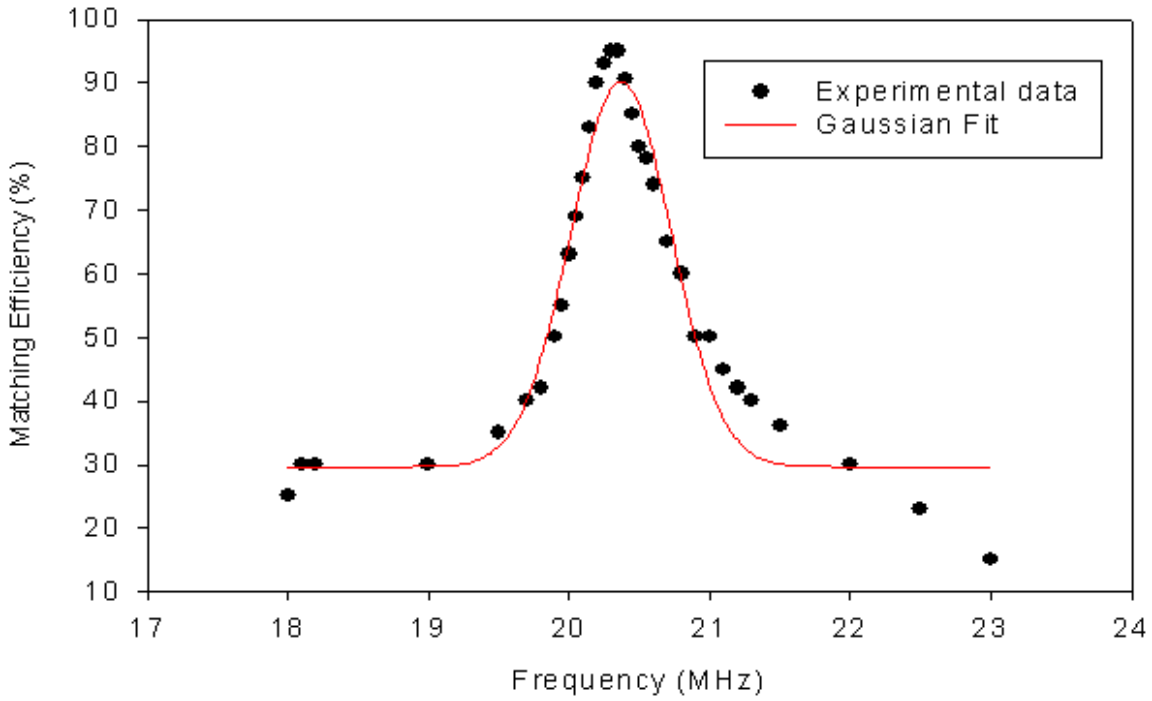

FIG. 2.18. Matching efficiency curve of the modified connection of the RF source. Data taken 3.12.2006

2.4 Shear Alfvén Waves Antennas

In order to launch magnitude and frequency controllable shear Alfvén waves in the LAPD, a total of three different antenna designs are used in this experiment for different azimuthal mode numbers (m). For m = 0, the disk antenna is the standard small source with a diameter (1.0 cm) comparable to the electron skin depth (δ_e ~ 0.5 cm). A phase locked rf tone burst at a variable frequency (below the minimum cyclotron frequency at B_0) is fed to the positively-biased disk to drive SAW. The field aligned blade antenna is made of a solid copper cylinder 0.96 cm in diameter. A sinusoidal rf current of ~ 2.0 A (rms) flows in the long leg aligned along z axis and azimuthally inductively coupled to the plasma with minimal influences from the two radial legs. To launch an m = 1 mode, a rectangular loop antenna containing two parallel current channels can be used. The resulting field

pattern resembles two small disk or blade antennas separated by a small distance only in perpendicular plane and driven with currents 180^{o} out of phase[16, 17]. Two intersecting Alfvén cone structures constructively interfere with each other to form a linearly polarized wave field propagating through the loop antenna axis that also aligns with the background magnetic field. Due to different preferences, the loop antenna is used in the fast-ion Doppler resonance experiment, and the field aligned blade antenna and the small disk antenna are most frequently used in the SAW spectral gap experiment.

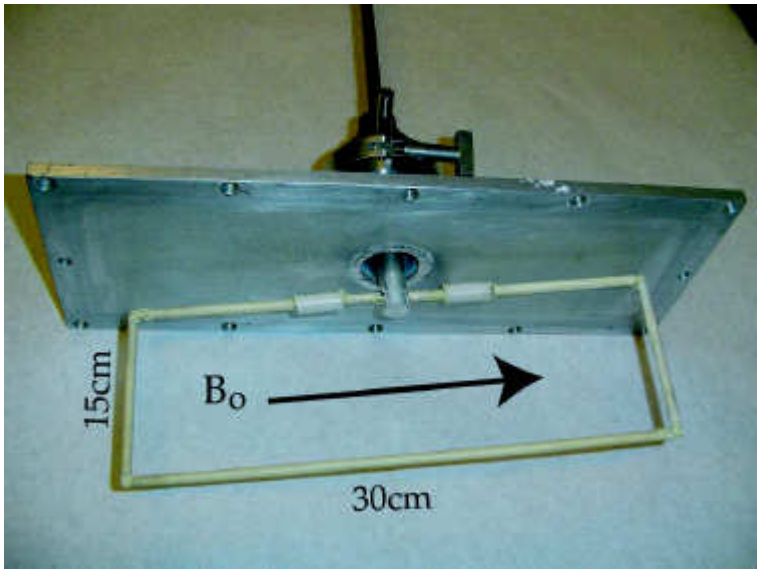

FIG. 2.19. Photograph of the loop antenna. (T. Carter, B. Brugman, UCLA)

2.5 Diagnostic Tools

Apart from the fast-ion sources and SAW antennas, the diagnostic tools are indispensable in detecting the desired fast-ion signals, ensuring plasma and waves behave normally, and guiding the improvement of the experiments. They are really the “eyes” of an experimentalist to “see” the invisible fast-ion beams and SAWs.

2.5.1 Collimated/Gridded Fast-ion Analyzers

Several probe designs to determine the position and energy distribution of the ion beam in the LAPD plasma were tested. To have good spatial resolution as well as sufficient collecting area, the probe collector has a diameter of typically 3.2 mm. With a beam current density considerably less than 1 mA/cm^2 typical probe current signals are in the 0.1 - 1 μA range at large distances from the ion gun. Detection of these small signals at the LAPD, particularly during the discharge, is challenging. The kiloamp level plasma discharge current pulse causes stray signals due to ground loops and capacitive as well as inductive coupling, which have to be eliminated by proper grounding and shielding. More important is the influx of background plasma ions and electrons into the detector/analyzer. Fast-ion analyzers taking advantage of either electrical or geometrical[16] shielding have been developed but none of them can detect fast-ion signals during the discharge. The best design combines both shielding techniques together to detect fast-ion signal successfully in the discharge (FIG. 2.20).

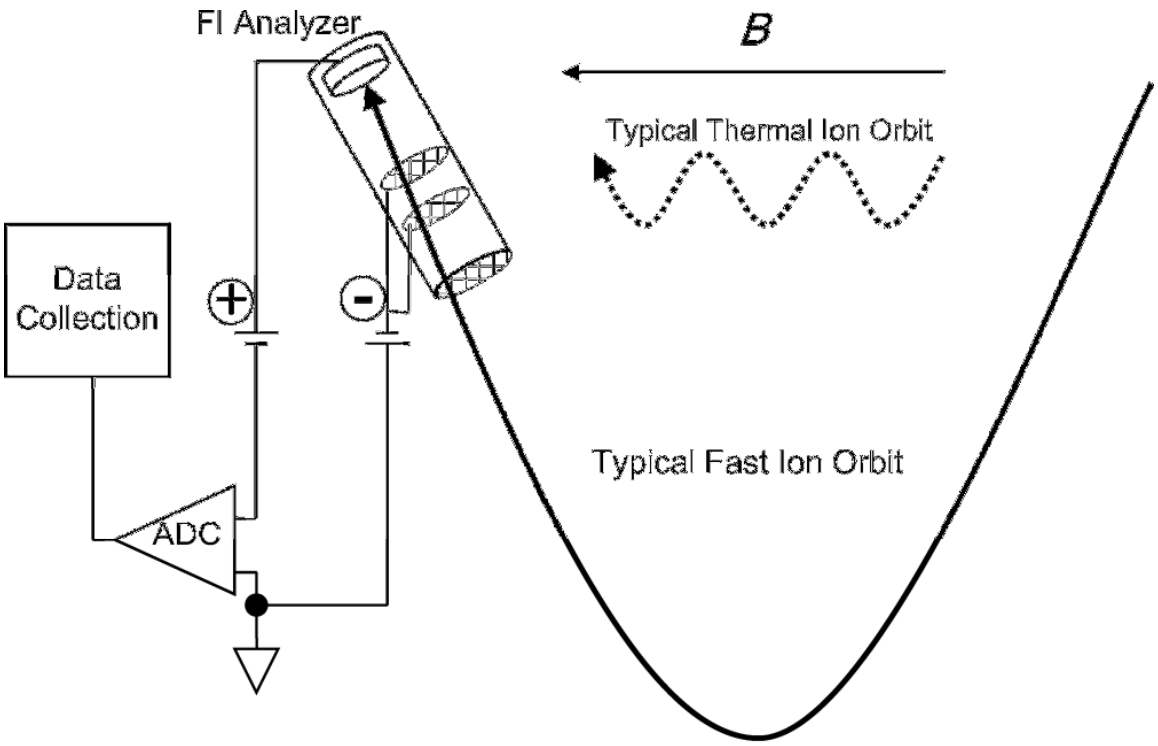

FIG. 2.20. Illustration of the Fast-ion Analyzer that distinguishes Fast-ion signals from thermal particles.

The collector of the fast-ion analyzer is biased positively at various voltages to obtain the energy distribution of the ion beam in the LAPD plasma. For a 600 eV beam with a pitch angle of 28º, measured 1" away from the beam exit in the LAPD afterglow plasma, the energy spread (3%) is similar to that measured in a vacuum magnetic field. A continuous low-energy tail is observed in the distribution.

For small pitch angles (<15˚), the collector of the fast-ion Analyzer is biased sufficiently positive (~+50 V) to reject plasma ions. Since this would result in the collection of plasma electrons, an intermediate grid is biased negative (~ - 50 V). In the discharge plasma, the Debye length (~15 μm) is smaller than the grid holes (~70 μm) that become partially transparent for electrons. Since grids with sufficiently small holes are not practical, two successive grids on the same potential were employed, the first grid reducing the plasma density and therefore increasing the Debye length for the second grid to become effective. For larger pitch angle (>15˚) beams, the tubular housing surrounding the recessed collector is directed parallel to the local ion beam trajectory. The collector is recessed in the housing by more than the plasma electron and ion Larmor radii (FIG. 2.20) to shield the collector from thermal particles geometrically. Thus one of the advantages of choosing a large pitch angle (>15˚) beam for this research is obvious: both electrical and geometrical shielding can work together to maximize the fast-ion signal to noise ratio. The acceptance angle of the probe is also ~ 15˚, which defines the angular resolution of the probe. During an experiment, the pitch angle of the probe can be optimized by maximizing the fast-ion signal on a scope.

FIG. 2.21 shows signal traces of a typical large pitch angle beam diagnostics. They are, as in four separate plots, the temporal evolution of the LAPD plasma line density, the voltage pulse applied to the emitter, the emitter current and the probe current for gun operation in the afterglow and during the discharge. The afterglow and the discharge traces are scanned independently but presented here together according to their timings relative to the LAPD plasma discharge. Both time windows, (1) and (2) in the figure, start from 20 ms after each emitter bias trigger and last for 6 ms, during which time the plasma conditions and ion gun performance are steady. The gun is operated at an angle of 28° with respect to a 1.5 kG magnetic field. The beam signals are measured one port from the gun (32 cm) where the ion beam has performed one cyclotron orbit. The probe signal carries some residual fluctuations due to the plasma pulse especially in the discharge, but the net signal is clearly revealed after subtracting the beam-off signal from the beam-on signal.

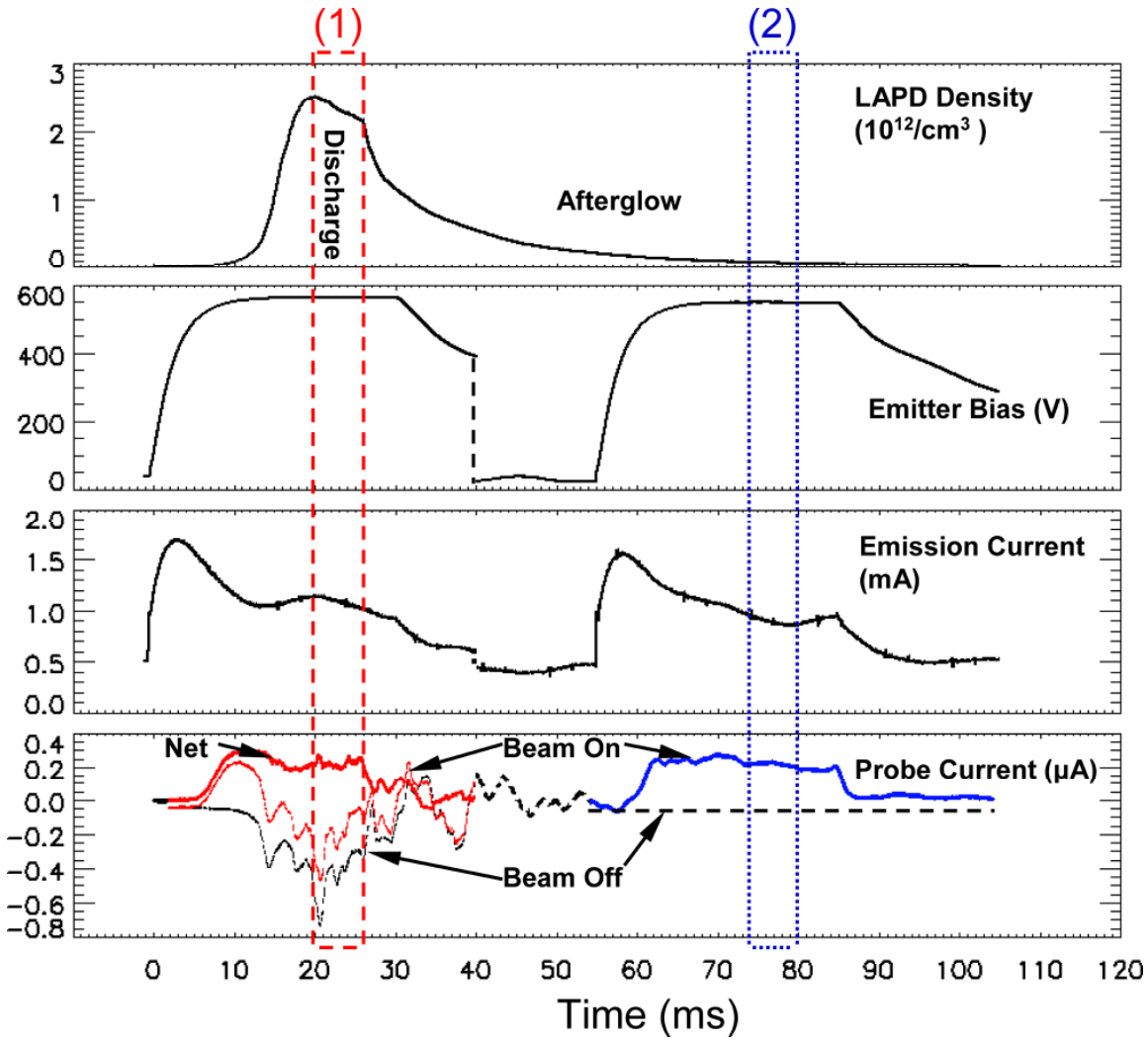

FIG. 2.21. Typical Fast-ion Analyzer collected signal with reference to LAPD plasma density and lithium source properties (0.6" emitter gun).
Conditions: B=1.5 kG; peak emitter bias=554 V; 1st grid bias= -100 V; analyzer axial distance from source=32 cm; analyzer grids biases are +50 V, -50 V. Two different time windows: (1) Discharge (averaging every 15 shots and every 128 continuous samples; sample rate at 50 MHz; 6 ms duration). Beam-on (red-dashed) signal is compared to beam-off (dashed). Net signal is shown as beam-on minus beam-off; (2) Afterglow (averaging every 3 shots and every 128 continuous samples; sample rate at 25 MHz; 6 ms duration). Beam-on (blue) signal is compared to beam-off (dashed).

Measurements of the beam profile in the LAPD plasma are shown in FIG. 2.22 where the fast-ion analyzer is scanned in the x-y plane (FIG. 2.12) with spatial steps of 1.0 mm in x and 2.0 mm in y. In all cases, the 0.6" emitter ion gun is operated with a 5 mm

aperture. FIG. 2.22 (a) displays the transverse beam profile for a zero pitch angle beam in the afterglow plasma, 2.5 cm from the ion gun. FIG. 2.22 (b) is a beam contour taken during the afterglow plasma [time window (2) in FIG. 2.21]. It was found in our previous fast-ion beam investigations [2] with argon ions, that, for helical beams, the slightly divergent beam emanating from the gun is refocused at integer numbers of gyro orbits. Therefore, orbits are always selected to complete integer numbers of gyro orbits that coincide with the location of diagnostic ports. In FIG. 2.22 (b) the beam has completed approximately one gyro orbit before reaching the analyzer at one port away (32 cm) along the z direction. The beam spot is elongated in the direction of gyro motion. A likely explanation for this effect is that, due to a finite energy spread, ions with different axial velocities take different amounts of time to reach the z position of the detector. The gyro phase ϕ at the detector is $\frac{\Omega_f \Delta z}{\mathrm{v}\cos\theta}$, where Ω_f is the cyclotron frequency, Δz is the fast-ion traveled distance in the z direction, v is the fast-ion speed and θ is the fast-ion pitch angle. Since Ω_f is independent of energy, ions with different energies reach the detector with different gyro phases. The variation in gyro phase with energy, $\Delta\phi$, can be expressed as

$$\Delta\phi = \sqrt{\frac{m_f}{8E^3}}\frac{\Omega_f \Delta z}{\cos\theta}\Delta E\,, \qquad (1)$$

where m_f is the mass of lithium fast-ion and ΔE is the variation of fast-ion energy. For a 20 eV beam energy spread, using parameters in FIG. 2.22 (b), the variation is 6.5 degrees in gyro phase and 0.31 cm in beam height along the gyro orbit. This results in the extra spread along the gyro direction. In contrast, the radial beam width is determined primarily by the emitted radius of the beam.

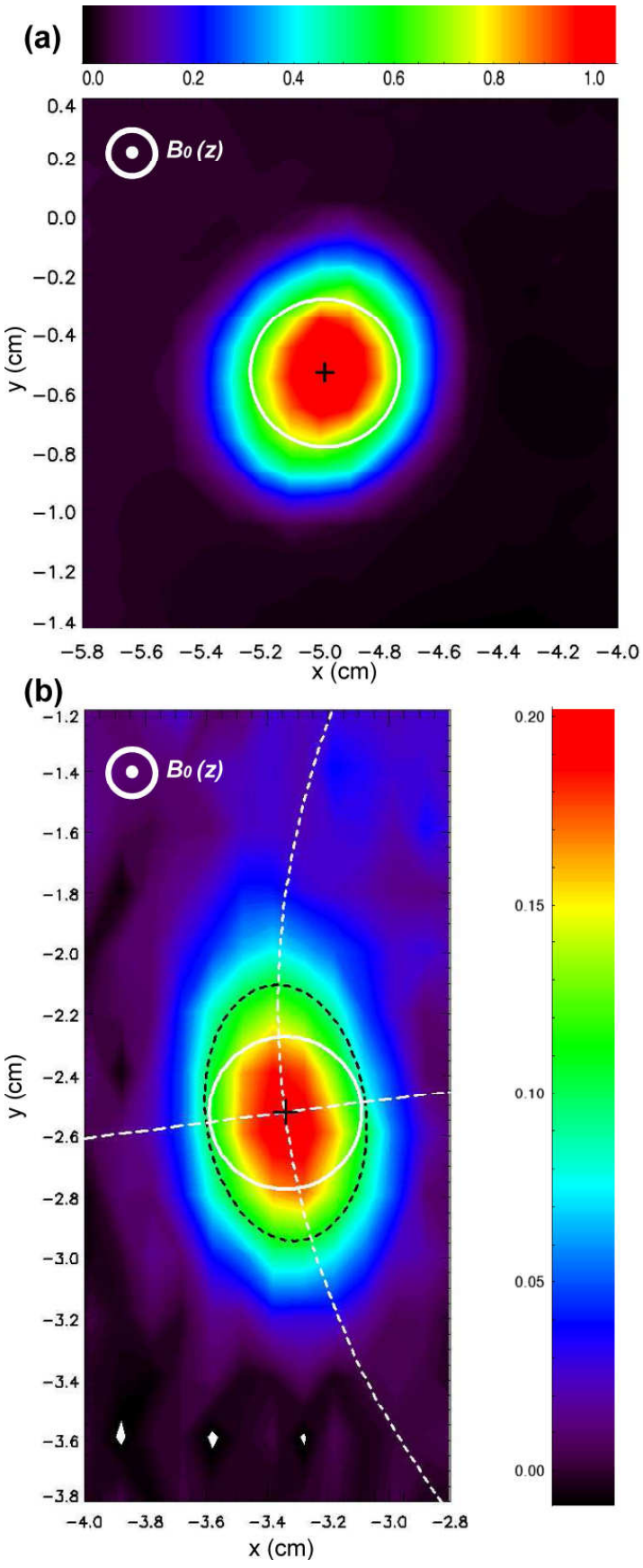

FIG. 2.22. Contours of 0.6" emitter gun beam profile in the LAPD plasma (color bars in μA; origin at LAPD machine center).
White solid circle: 0.5 cm diameter aperture (ideal beam spot); Black cross hair: beam center; Black dash ellipse: ellipse with semimajor and semiminor axes calculated from 2D Gaussian fit of beam contour; White dash curve: part of the beam orbit projection of x-y plane with theoretical radius of 2.73 cm; White long dash line: radial line connecting beam center and orbit center.

The curvature of the gyro orbit at the beam collection point causes a small portion of the beam to be absorbed on the probe wall before reaching the recessed collector, which is the vignetting effect discussed in Ref. [18]. Since the analyzer is always rotated in the y-z plane to match the incoming beam, the collector effective aperture in the y direction is close to the collector diameter of 3.2 mm. The collector effective aperture in the x direction is determined to be ~ 2.7 mm by a simulation of an ensemble of fast-ion orbits in the analyzer geometry in the x-z plane. If a perfect 5 mm diameter beam is collected in this manner, the widths of the beam along the x and y directions, convoluted with the collector effective aperture, are 5.7 mm and 5.9 mm respectively.

To analyze the radial beam profile, the white dash curve is first fitted in FIG. 2.22 (b) to indicate the beam trajectory in the x-y plane with a radius of 2.7 cm that is calculated from the beam launching conditions. Then the profile data are extracted along radial lines and fitted to Gaussian distributions with the goodness of fitting (χ^2) recorded as statistical weights [3]. An example of a radial line is shown in FIG. 2.22 (b) connecting the cross hair and the orbit center.

Radial profiles of the beam are shown in FIG. 2.23 for the discharge and the afterglow signals. Both profiles are weighted averages of all the available radial lines with sufficient signal intensity. The profiles are accurately represented by Gaussian distributions. The error bars correspond to temporal fluctuations of beam local intensity and they are calculated by taking standard deviations (STD) of 60 continuous time bins (0.1 ms) of beam intensity at each radial location. The discharge beam signal is noisier than the afterglow signal. The full width at half maximum (FWHM) for each curve is close to the expected beam collection width.

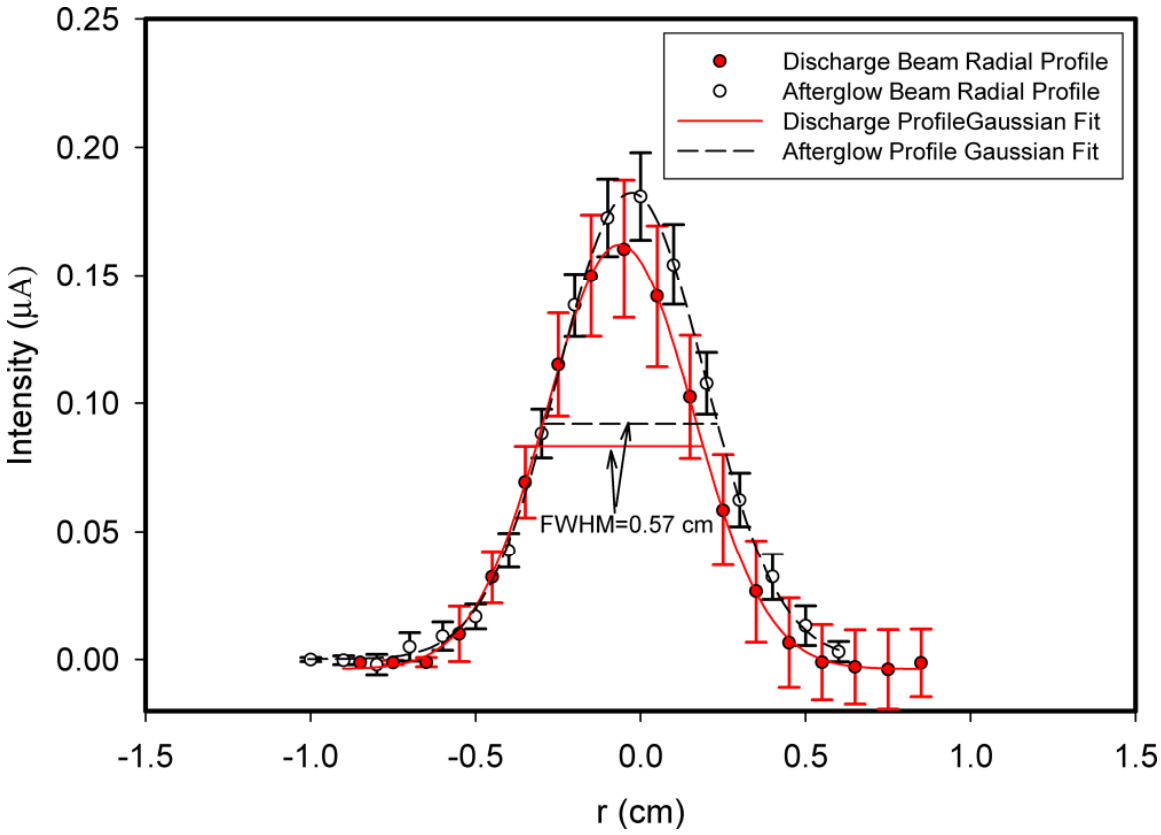

FIG. 2.23. Weighted average radial beam profile in the discharge and the afterglow.
r=2.7 (cm) corresponds to the predicted center of the gyro orbit. The horizontal line indicates the FWHM for each curve.

2.5.2 B-dot Probes for Wave Magnetic Field

The wave magnetic field is measured by a set of identically designed *b-dot* probes featuring three orthogonal induction coil-pairs which are sensitive to the time derivative of the wave magnetic field[19]. Each coil-pair is connected to a differential amplifier to select magnetic signal and reject common mode noise. The calibration information of the ten *b-dot* probes is in Appendix D. During the experiments, the magnetic coils are oriented so that the three components of the wave field align with the LAPD coordinate system.

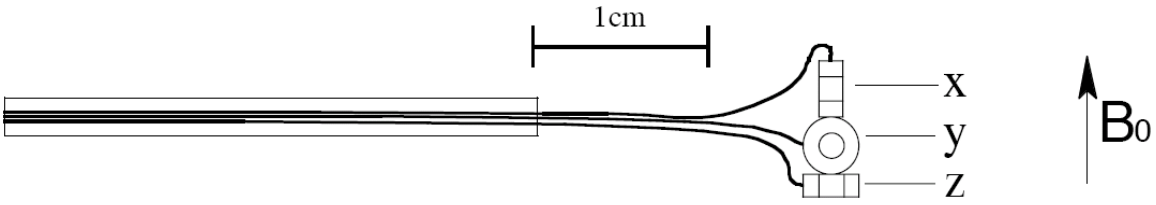

FIG. 2.24. An example of the orthogonal coils in a *b-dot* probe.
(Figure from S. Vincena Ph. D. thesis)

[1] http://www.cscamm.umd.edu/cmpd/lapd.htm

2 H. Boehmer, D. Edrich, W.W. Heidbrink, R. McWilliams, and L. Zhao, Rev. Sci. Instrum., 75, 1013 (2004).

3 L. Zhao, W.W. Heidbrink, H. Boehmer, R. McWilliams, Phys. Pl. **12**, 052108 (2005).

4 Y. Zhang et al., Bull. Am. Phys. Soc. FP1.00075 (2005).

5 M. Sasao, K. A. Connor, K. Ida, H. Iguchi, A. A. Ivanov, M. Nishiura, D. M. Thomas, M. Wada, and M. Yoshinuma,IEEE Trans. Plasma Sci., **33**(6), 1872(2005).

6 J. P. Blewett, Ernest J. Jones, Phys. Rev., **50,** 464(1936).

7 G. E. Sasser, S. F. Knowlton, R. F. Gandy, H. Lin, E. E. Thomas, and M. A. Owens, Rev. Sci. Instrum., **66**(1), 324 (1995).

8 D. C. Pritchard, R. F. Gandy, J. D. Hanson, S. F. Knowlton, H. Lin, G. E. Sasser, E. Thomas, Jr., and J. Cooney, Phys. Plasmas, **4**(1), 162 (1997).

9 D. M. Thomas, A. S. Bozek, J. I. Robinson, K. H. Burrell, T. N. Carlstrom, T. H. Osborne, R. T. Snider, D. K. Finkenthal, R. Jayakumar, M. A. Makowski, D. G. Nilson, and B. W. Rice, Rev. of Sci. Instrum. **72**(1), 1023(2001).

10 R. J. Fonck, P. A. Duperrex, and S. F. Paul, Rev. of Sci. Instr. **61**(11), 3487(1990).

11 G. McKee, R. Ashley, R. Durst, R. Fonck, M. Jakubowski, K. Tritz, K. Burrell, C. Greenfield, and J. Robinson, Rev. of Sci. Instr. **70**(1), 913(1999).

12 D. M. Thomas, Rev. of Sci. Instr. **66**(1), 806(1995).

13 A. Theodore Forrester, *Large Ion Beams—Fundamentals of Generation and Propagation* (Wiley,1988).

14 Heat Wave Labs, Inc. alkali ion source doc. http://www.cathode.com/pdf/tb-118.pdf

15 H. B. Haskell, O. Heinz, D. C. Lorents, Rev. Sci. Instrum., **37**(5), 607 (1966).

[16] W. Gekelman, S. Vincena and D. Leneman, Plasma Phys. Control. Fusion **39**, A101 (1997).

[17] Walter Gekelman, Stephen Vincena, David Leneman, James Maggs, J. Geophys. Res. **102**, 7225

(1997).

18 W. W. Heidbrink, J. D. Strachan, Rev. Sci. Instrum. **56**, 501 (1985)

[19] D. Leneman, W. Gekelman, and J. Maggs, Phys. Plasmas **7** (10), 3934 (2000).

Chapter 3

FAST-ION DOPPLER SHIFTED CYCLOTRON RESONANCE WITH SHEAR ALFVÉN WAVES

This chapter presents the direct experimental measurement of fast-ion cross-field transport induced by SAWs in the linear regime.

- Sec. 3.1: Analytical resonance theory
- Sec. 3.2: SAW dispersion relation
- Sec. 3.3: Simulation codes
- Sec. 3.4: Experimental setup
- Sec. 3.5: Resonance results

3.1 Resonance Theory

A charged particle is in cyclotron resonance with a transverse wave if the oscillation of wave electric field $\tilde{\mathbf{E}}$ matches the Doppler-shifted cyclotron motion of the particle[1], when the particle and the wave exchange energy effectively. The condition for such a resonance between fast ions and SAWs propagating parallel to the ambient magnetic field $\mathbf{B_0}$ (along the *z* direction) is

$$\omega - k_z \mathrm{v}_z \cong \pm\Omega_f , \tag{3.1}$$

where ω and k_z are the wave frequency and parallel wave number; v_z is the parallel velocity of the fast ions in the lab frame; and $\Omega_f = q_f B_0 / m_f$ is the cyclotron frequency of the fast ions. For MHD shear Alfvén waves, the dispersion relation is $\omega = k_z \mathrm{v}_A$ with $\mathrm{v}_A = B_0 / \sqrt{\mu_0 n_i m_i}$ as the wave phase velocity (the Alfvén speed), $n_i m_i$ is the mass density of the plasma. The upper/lower sign in Eq. (3.1) corresponds to the normal/anomalous Doppler resonance where fast ions travel slower/faster than the wave phase velocity along $\mathbf{B_0}$. In the following experiments, normal Doppler resonance is investigated. The goodness of the resonance is first evaluated by this normalized difference

$$\Delta\bar{\omega} = \left(\omega - k_z \mathrm{v}_z - \Omega_f\right) / \Omega_f \ll 1. \tag{3.2}$$

The position $\mathbf{x}$ and velocity $\mathbf{v}$ of the fast ion is given by the Lorentz force law,

$$\begin{cases} \dfrac{d\mathbf{v}}{dt} = \dfrac{q_f}{m_f}\left(\tilde{\mathbf{E}} + \mathbf{v}\times\mathbf{B}_0 + \mathbf{v}\times\tilde{\mathbf{B}}\right) \\ \dfrac{d\mathbf{x}}{dt} = \mathbf{v} \end{cases}, \tag{3.3}$$

where $\tilde{\mathbf{E}}$ and $\tilde{\mathbf{B}}$ are the wave fields of SAW. Adopting Cartesian coordinates, the wave

electric field can be modeled as linearly polarized in the *y*-z plane,

$$\tilde{\mathbf{E}}(y,z,t)=\left(\tilde{\mathrm{E}}_y\hat{y}+\tilde{\mathrm{E}}_z\hat{z}\right)\cos(\omega t-k_z\mathrm{v}_z+\varphi_0), \tag{3.4}$$

where φ_0 is the launched phase of the fast ion relative to the wave and assuming $\tilde{\mathrm{E}}_x=0$. From Ampere's law, $\tilde{\mathrm{E}}_y$ is related to $\tilde{\mathrm{B}}_x$ through:

$$\tilde{\mathrm{E}}_y=-\frac{k_z\tilde{\mathrm{B}}_x}{\omega\mu\varepsilon}, \tag{3.5}$$

where $\mu\varepsilon$ is determined by the plasma dispersion relation (Sec. 3.2). In the experiment, $\tilde{\mathrm{E}}_y$ has a perpendicular pattern determined by the characteristics of the SAW antenna (see Sec. 3.4.4). Replace $\tilde{\mathbf{B}}$ in Eq. (3.3), then the changes of fast-ion velocity components become

$$\begin{cases}\dfrac{d\mathrm{v}_x}{dt}=\dfrac{q_f}{m_f}\left(\mathrm{v}_y\times\mathrm{B}_0\right)\\ \dfrac{d\mathrm{v}_y}{dt}=\dfrac{q_f}{m_f}\left[-\mathrm{v}_x\times\mathrm{B}_0+\left(1-\dfrac{\omega\mu\varepsilon}{k_z}\mathrm{v}_z\right)\cdot\tilde{\mathrm{E}}_y\right],\\ \dfrac{d\mathrm{v}_z}{dt}=\dfrac{q_f}{m_f}\left(\tilde{\mathrm{E}}_z+\dfrac{\omega\mu\varepsilon}{k_z}\mathrm{v}_y\cdot\tilde{\mathrm{E}}_y\right)\end{cases} \tag{3.6}$$

which shows that perpendicular acceleration is only along the *y* direction, and that the parallel acceleration is associated with the rate of change of perpendicular kinetic energy[1], as well as acceleration from $\tilde{\mathrm{E}}_z$. At the *exact* Doppler resonance condition, v_y grows linearly with *t*. The phase of $\tilde{\mathrm{E}}_y$ seen by the fast ion changes and eventually turns opposite, when the fast ion accelerates in the opposite direction. The amplitudes of the parallel and perpendicular velocities undergo slow oscillations over time and space much longer compared to the period and wavelength of the wave. This oscillation is actually the fast ion's trapping in the SAW. From Ref. [1], the trapping period (τ_{trap}) can be calculated

as

$$\tau_{\text{trap}} = \sqrt{\frac{8\pi m_f \omega}{k_z^2 q_f \mathrm{E}_y \mathrm{v}_{0z}}}\,, \tag{3.7}$$

where v_{0z} is the initial parallel velocity. The distance traveled along the z direction in t_{Trap} is defined as λ_{trap}, the trapping length.

The Landau resonance is another resonance mechanism for the fast-ion beam to exchange energy with the SAW. The resonance condition for this case seems conceptually simpler than the Doppler resonance:

$$\omega - k_z \mathrm{v}_z \cong 0\,. \tag{3.8}$$

However, it requires a fast Li^+ ion (> 2 keV) at a relatively small initial pitch angle, which is currently not an operational regime for this thermionic emission source (see Sec. 2.3.1). One example of the Landau resonance condition is listed in Table 2, where the plasma conditions are modified from usual LAPD operations in order to slow down the wave.

3.2 SAW Dispersion Relation

There are two regimes of plasma parameters for SAW propagation: the Kinetic Alfvén Wave (KAW) for plasma electrons having a Boltzmann distribution in the presence of the Alfvén wave fields and the Inertial Alfvén Wave (IAW) for electrons responding inertially to the wave. The KAW is more relevant to the physics of the interior regions of tokamak plasmas and the IAW to the edge and limiter regions. In this experiment, KAWs launched during the discharge of the LAPD are investigated.

A dimensionless parameter— $\overline{\beta}_e \equiv \overline{\mathrm{v}}_{te}^2 / \mathrm{v}_A^2$ is a quantitative measure of how inertial

or kinetic a plasma region is, where $\bar{v}_{te} = \sqrt{2T_e / m_e}$ is the thermal electron speed with T_e the electron temperature. If $\bar{\beta}_e >> 1$, as in the discharge plasma of the LAPD, it is kinetic; if $\bar{\beta}_e << 1$, as in most of the afterglow, inertial. For the KAW, the dispersion relation is

$$\omega^2 / k_{//}^2 = v_A^2 (1 - \bar{\omega}^2 + k_\perp^2 \rho_s^2), \tag{3.9}$$

where $k_{//}$ is the component of the wave vector parallel to the background magnetic field, $k_\perp$ is the perpendicular wave number and ρ_s is the ion sound gyro-radius $\rho_s = c_s / \omega_{ci}$ with $c_s = (T_e / m_i)^{1/2}$. The intensity of the parallel wave electric field is[13]

$$\tilde{\mathbf{E}}_{//} = \frac{i\omega k_\perp \rho_s^2}{v_A (1 - \bar{\omega}^2)(1 - \bar{\omega}^2 + k_\perp^2 \rho_s^2)^{1/2}} \tilde{\mathbf{E}}_\perp . \tag{3.10}$$

A typical ratio of $\left| \frac{\tilde{\mathbf{E}}_{//}}{\tilde{\mathbf{E}}_\perp} \right|$ is 0.01, which means that the non-vanishing parallel electric field will modify v_z in the resonance experiment. The perpendicular electric field can be calculated from Ampère's law and the dispersion relation:

$$\left| \frac{\tilde{\mathbf{E}}_\perp}{\tilde{\mathbf{B}}_\perp} \right| = \frac{v_A (1 - \bar{\omega}^2)}{(1 - \bar{\omega}^2 + k_\perp^2 \rho_s^2)^{1/2}} . \tag{3.11}$$

3.3 Resonance Orbit Simulation Code

3.3.1 Single particle simulation

If the cross field transport of the test-particle beam is much smaller than the scale

length of the wave fields, then a single particle Lorentz code is capable of predicting the expected resonance beam profile by launching particles at an ensemble of initial phases (φ_0).

In the plasma physics literature, cross-field diffusion usually refers to radial transport of guiding centers. In this experiment, the fast ions only execute a few Larmor orbits prior to measurement, so it is conceptually simpler to examine the full helical Lorentz orbit rather than the guiding-center orbit. A typical Doppler resonance fast-ion trajectory is shown in FIG. 3.1 a). Fast ion and wave parameters (Table 2) are chosen to satisfy the Doppler resonance condition of $\Delta\bar{\omega} < 0.1$, using feasible experiment conditions. To indicate the relative strength of different SAWs, B_{max} is defined as the maximum amplitude of $\tilde{B}_x$ in a specific *z* plane. If $\tilde{B}_x = B_{max}\hat{x}$ at t = 0, the ions, initiated in phase with the wave, would lose energy (FIG. 3.1 b) continuously from the wave and the magnetic moment ($\mu = mv_\perp^2 / 2B$) decreases. At several gyro-cycles away in the z direction, the fast-ion energy (*W*) and μ changes linearly with the traveling time/distance; as *W* changes, the initial phase φ_0 will eventually change to $\varphi_0 \pm \pi$, when *W* starts to change in the opposite direction. The trapping length (λ_{trap}) is ~ 46 m from the original *z* position (FIG. 3.1 b). The fast ion oscillates in phase space over long periods—the trapping of fast ions in the wave frame.

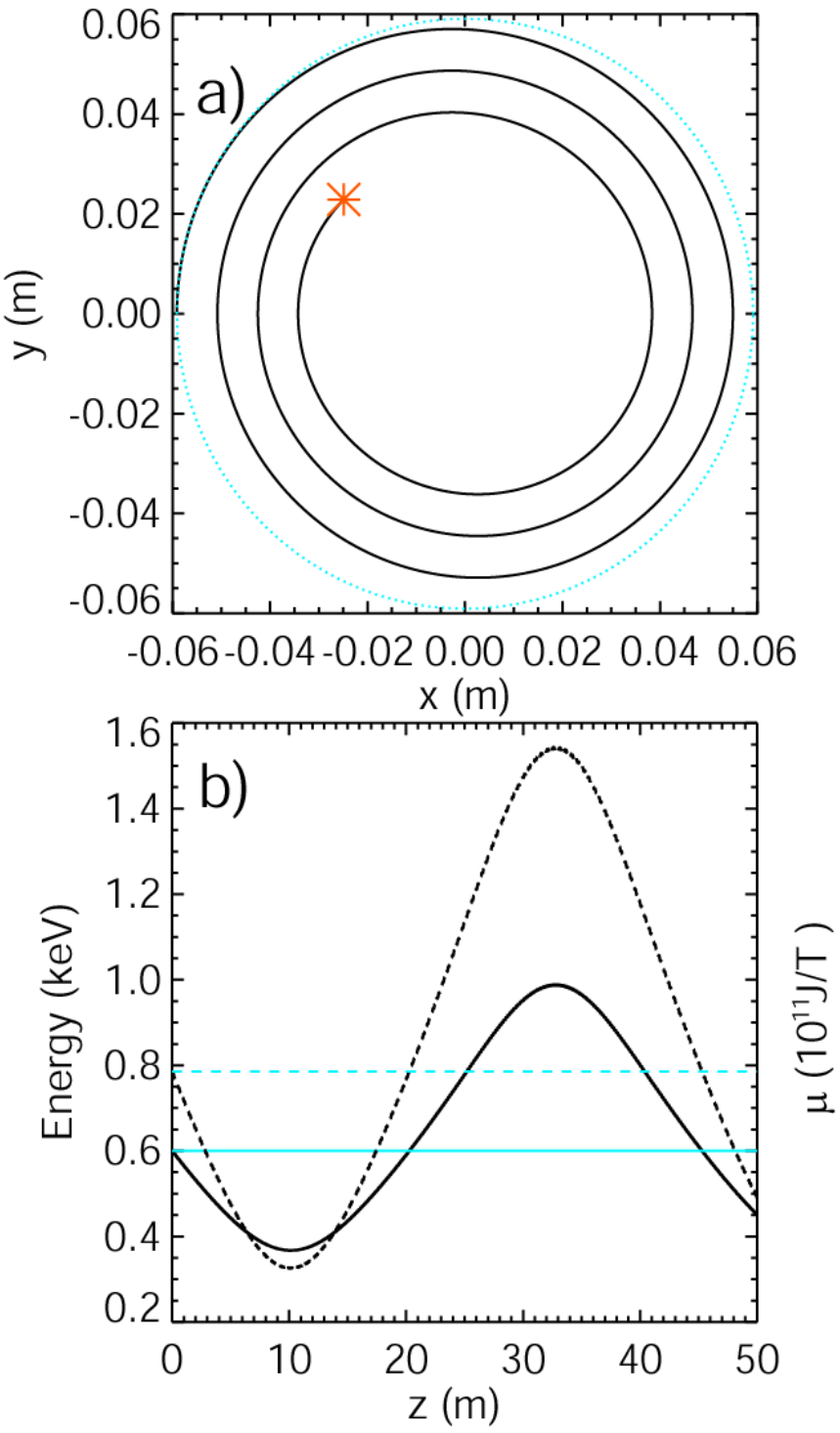

FIG. 3.1 Single-particle simulation results.
a) An *x-y* projection of SAW influenced gyro-orbit (solid black) is compared with the unperturbed one (dotted cyan). B_{max} = 10 G; b) Fast-ion energy and magnetic moment trapping in the SAW. B_{max} = 1 G. (φ_0 = 0, fast-ion parameters refer to Doppler resonance case III in Table 2)

If an ensemble of ions are launched with random phases relative to the wave, $\varphi_0 \in [0, 2\pi]$, other initial conditions being identical, their positions on the collection plane mark the spatial spreading caused by the perturbation from the wave field (FIG.3.2 a). The maximum displacements from the undisturbed position along the $\hat{r}$ and $\hat{\phi}$ directions are defined as Δr and $r_0 \Delta \Phi$. It is obvious that Δr is a direct indicator of the change in perpendicular ion energy ($W\perp$). The gyro phase Φ at the collection plane is $\frac{\Omega_f \Delta z}{v_z}$, where Δz is the distance traveled by fast ions in the z direction. Thus $r_0 \Delta \Phi$ indicates the change in parallel energy ($W_{//}$).

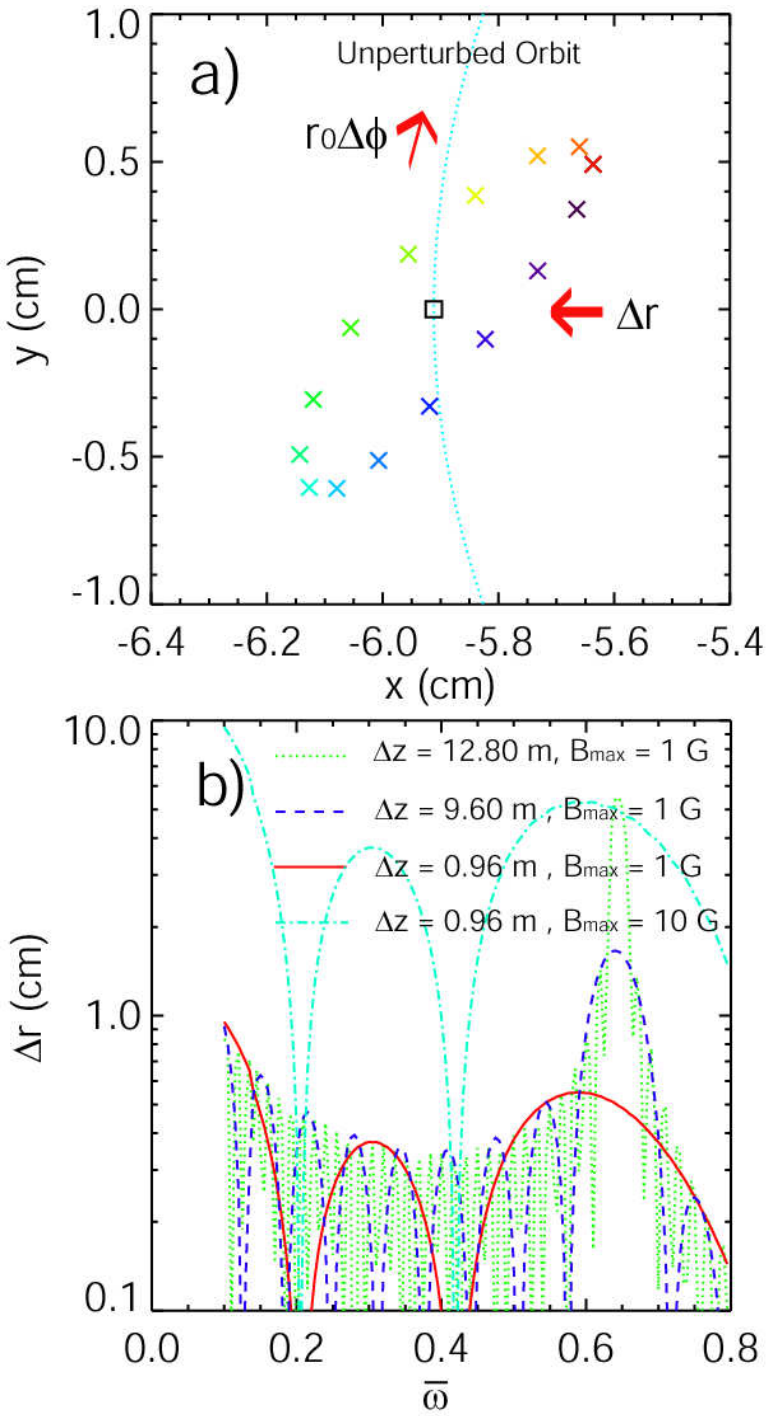

FIG.3.2. Single-particle simulation results, cont.
a) Fast ion collection positions at Δz = 0.96 m with 16 uniformly distributed values of initial wave phase φ_0 (color crosses). Black box is the unperturbed collection position. B_{max} = 1 G; b) Doppler resonance spectra of Δr at variable z and B_{max}. (Fast-ion parameters refer to Doppler resonance case III in Table 2)

In the simulation, varying the wave frequency from 0.1 to 1.0 ω_{ci} (singly-ionized helium ion cyclotron frequency), one can obtain the spectrum of spatial displacements caused by the SAW perturbation. In FIG.3.2 b) Δr and $r_0\Delta\Phi$ are plotted against $\bar{\omega} = \omega / \omega_{ci}$, where the frequency satisfying the resonance condition ($\Delta\bar{\omega} = 0$) is 0.65 ω_{ci}. Resonance spectra show that the maximum displacement occurs at the expected frequency. At larger Δz (less than $\lambda_{trap}/4$), the resonance frequency is closer to 0.65 ω_{ci} and the resonance peak is sharper. At shorter lengths, e.g. several gyro-cycles away, the quality factor of the resonance is degraded but a clear maximum is still observed. The spatial displacements are proportional to the SAW wave field amplitude, as expected for moderate field perturbations ($\delta B / B < 1\%$) in the linear regime.

The simulation code was first used to find the optimal conditions for conducting the resonance experiments with fast-ion sources in the LAPD. Realistic ranges for parameters listed in Table 2 are evaluated in the code for $\Delta\bar{\omega}$, Δr and $r_0\Delta\Phi$. Those sets of parameters satisfying $\Delta\bar{\omega} \ll 1$ while producing observable Δr and $r_0\Delta\Phi$ are selected for experiments at the LAPD. Three lithium fast-ion Doppler resonance conditions in Table 2 are realized and measured experimentally. In this article, if not otherwise specified, the resonance parameters are for Li_7^+ Doppler resonance case (III).

Resonance / Parameter	Li^{+}_{7} Doppler (I)	Li^{+}_{7} **Doppler (II)**	Li^{+}_{7} **Doppler (III)**	$Li^{+}{}_{7}$ Landau
B (kG)	1.6	**1.74**	**1.2**	0.5
W (eV)	600	**600**	**600**	2000
θ (deg)	29.5	**44.8**	**49.3**	15
ρ (cm)	2.9	**3.8**	**5.9**	8.2
Gyro-cycle/port	1/1	**4/3**	**1/1**	1/6
n_e (10^{12} cm^{-3})	2.0	**2.5**	**2.5**	4
T_e (eV)	6	**6**	**6**	4
f_{ci} (kHz)	610	**663**	**457**	191
Δr (cm) (Δz = 0.96 m)	0.43	**0.5**	**0.5**	n/a
Resonance $\bar{\omega}$	0.63	**0.63**	**0.65**	128

Table 2 List of parameters for typical cases of fast ion and SAW resonance.

3.3.2 Monte-Carlo simulation

Since the single-particle model cannot simulate a finite beam with spatial and energy distributions, an existing Monte-Carlo fast-ion orbit code[2] is upgraded to include the SAW induced fast-ion transport, as well as the classical transport caused by thermal ions and electrons. In the LAPD discharge plasma, the electrons dominate Coulomb slowing-down, while thermal ions dominate the pitch-angle scattering rate. A number of fast ions are launched numerically according to the initial beam divergence in phase space (±5 deg. in pitch angle and ~ 5 eV in energy). Due to the difference in time scales of the transport mechanisms shown in Table 3, the classical transport effects can be

readily de-coupled from the SAW influence.

Transport Time Scales	Time (ms)
Pitch angle scattering: τ_{PAS}	5
Coulomb energy-loss: τ_{W}	1
SAW period: τ_{SAW}	0.002 – 0.02
Cyclotron Motion: $\tau_{Cyclotron}$	~ 0.003

Table 3 Comparison of time rates for different transport mechanisms. B_0 = 1.2 kG

During the simulation of each fast-ion orbit, the pitch angle scattering event is considered at a randomly selected time ($t = t_1$), by which each gyro-period is divided into two partitions ($\tau_{Cyclotron} = t_1 + t_2$). FIG.3.3 shows the flow chart of the simulation process. The single-particle Lorentz code is carried on throughout t_1 and t_2 for SAW perturbation. At the end of each time partition, the fast-ion energy is updated by the Coulomb slowing-down effect:

$$W' = W \exp\left(-\frac{t}{\tau_W}\right). \tag{3.12}$$

At $t = t_1$, a Monte-Carlo collision operator[2] developed from the Coulomb scattering theory[3] is loaded to scatter the direction of the fast-ion velocity without changing its magnitude. After the desired number of gyro-periods is finished, the fast-ion velocity and coordinates are recorded in the computer memory and next fast-ion orbit is launched.

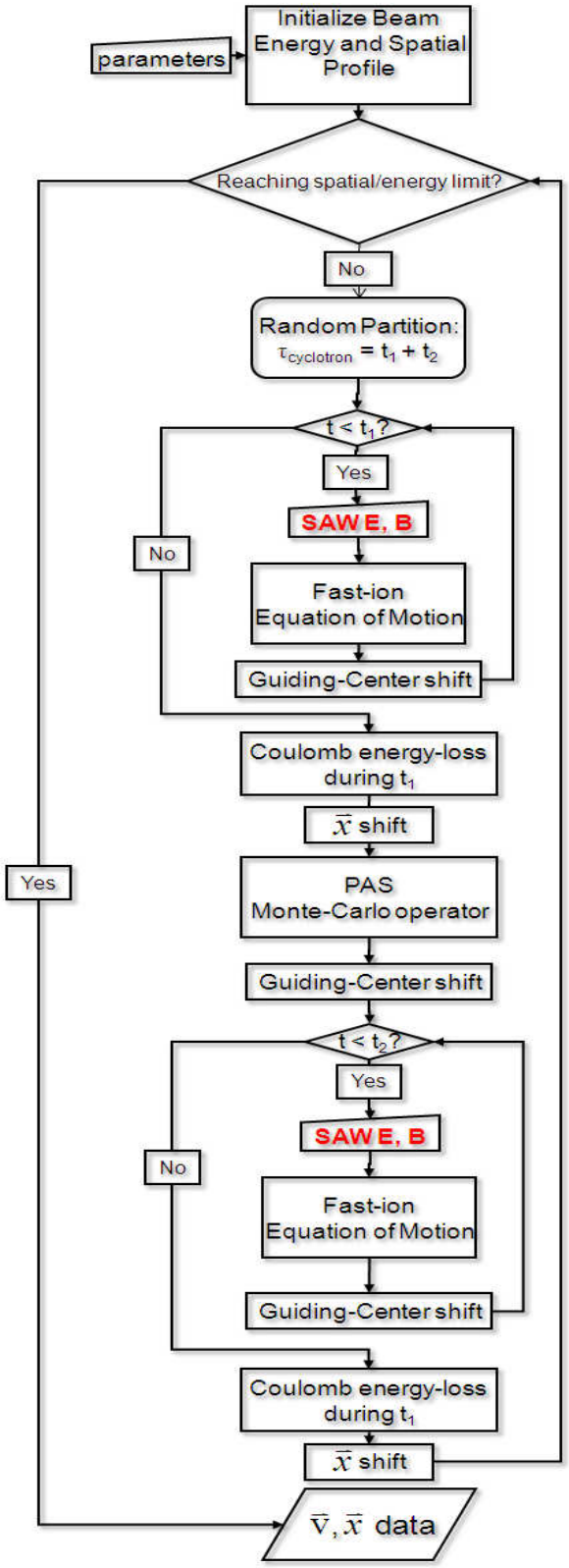

FIG.3.3 Monte-Carlo simulation flow chart

Using the same linearly polarized shear Alfvén wave fields as for the single-particle simulation, thousands of fast-ion orbits are launched with random phases (φ_0) to contribute to the beam profile several gyro-cycles away. The SAW-perturbed beam profiles are compared in FIG.3.4 with the classical profiles at different distances traveled by fast ions. Notice in FIG.3.4, all the fast ions collected in the x-y plane are included regardless of their final velocities. The classical beam profile produced by a 0.5 cm diameter source aperture is shown in FIG.3.4 a). For the SAW-perturbed beam profiles, B_{max} is set at 10 G. At the resonance peak frequency (FIG.3.4 b, $\bar{\omega} = 0.65$), substantial profile widening happens along both the $\hat{r}$ (gyro-radius) and $\hat{\phi}$ (gyro-angle) directions. The widening effect increases with the distance traveled by the fast ion. At the resonance null frequency (FIG.3.4 c, $\bar{\omega} = 0.20$), on the contrary, fast ions only perform drifting motions along with the guiding center, whereas the gyro-radius as well as the perpendicular energy doesn't change much. At $\Delta z = 0.32$ m and 0.64 m, beam profiles at different phase (φ_0) form a ellipse. At $\Delta z = 0.96$ m, where fast ions finish 3 gyro-cycles, beam profile (FIG.3.4 c) has minimal drifting and is close to the unperturbed one in FIG.3.4 a). These results from the Monte-Carlo model agree with the experimental findings in Sec. 3.5.

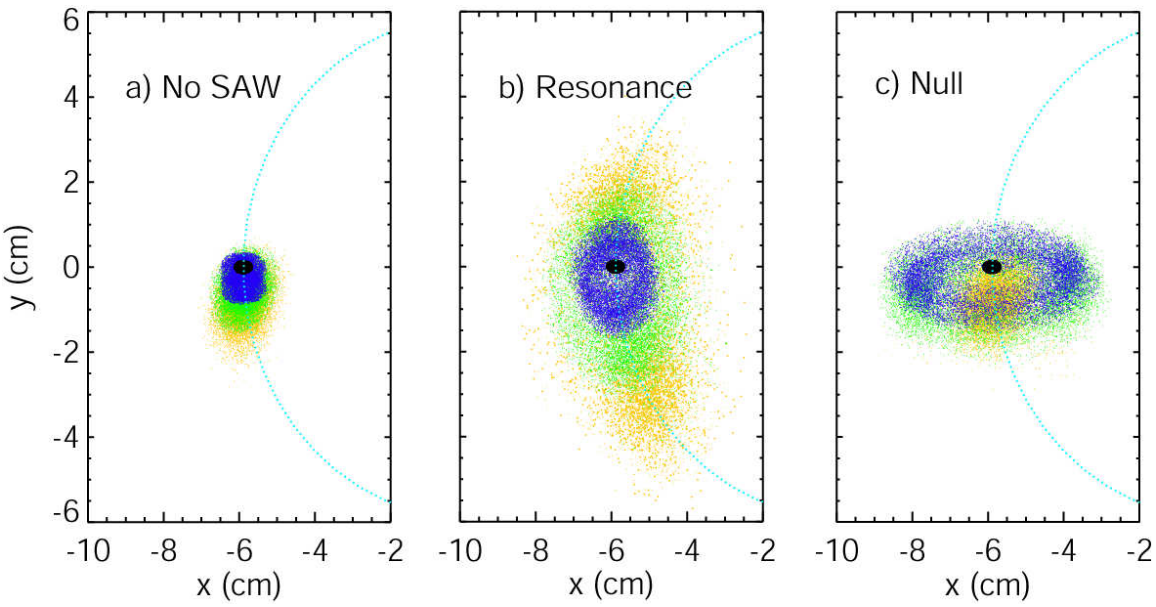

FIG.3.4. Monte-Carlo model simulated fast-ion beam profiles with different SAW perturbations.
The color of the dots indicates fast ion collection at different *z* planes: black (Δz = 0 m), blue (Δz = 0.32 m), green (Δz = 0.64 m) and orange (Δz = 0.96 m). (a) no SAW present; (b) SAW at $\bar{\omega}$ = 0.65 (resonance peak), $\tilde{B}_x$ = 10 G; (c) SAW at $\bar{\omega}$ = 0.20 (resonance null), $\tilde{B}_x$ = 10 G.

3.4 Resonance Experimental Setup

3.4.1 Overview

This experiment is performed in the upgraded LAPD, which has a 17.56-m-long, 1-m-diameter cylindrical main vacuum chamber. Pulsed plasmas (~ 10 ms in duration, 1 Hz repetition rate and ±10% spatial uniformity) are created by a discharge between a barium oxide coated cathode and a gridded molybdenum anode[4]. The cathode and anode are separated by 50 cm and are both located at the south end of the machine. The working gas is helium at a partial pressure ~ 3 x 10^{-5} Torr with less than 3% of impurities. Typical

average plasma parameters for this experiment are: $n_i \sim 2.5 \times 10^{12}$ cm^{-3}, $T_e \sim 6$ eV, $T_i \sim 1.0 \pm 0.5$ eV.

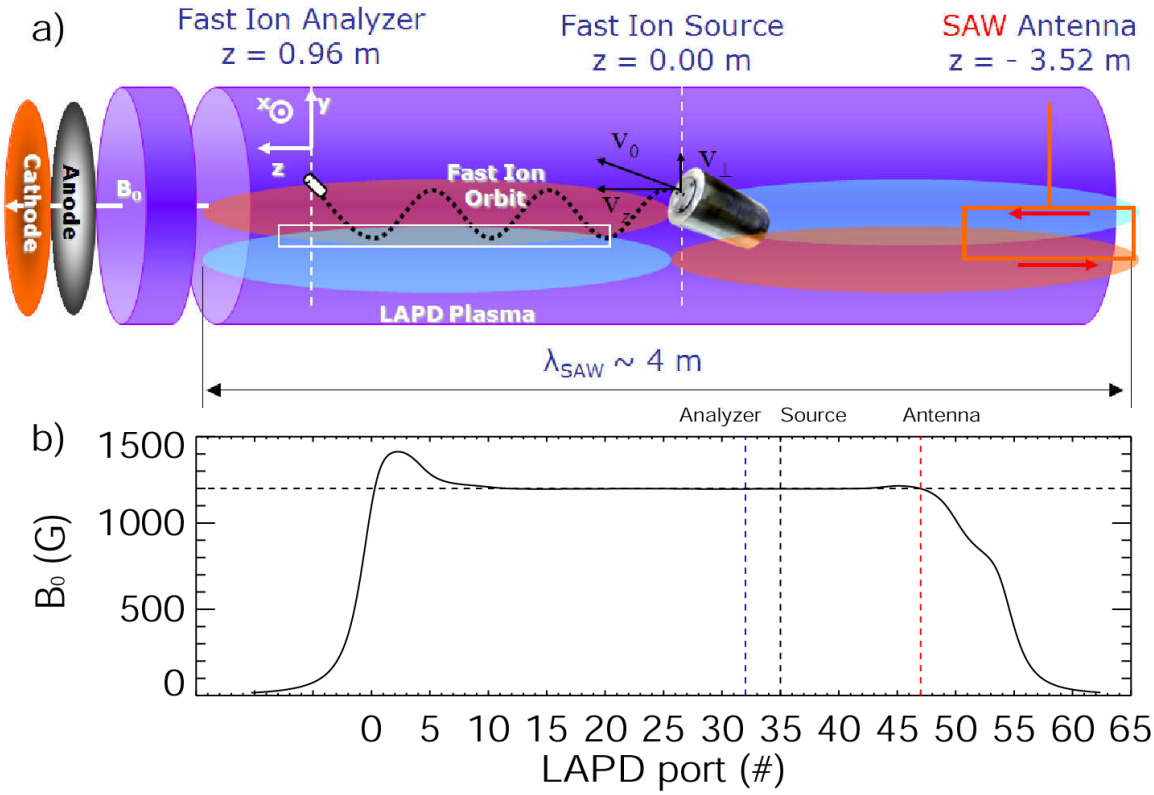

FIG.3.5. Experimental setup at the LAPD.
a) Overview of instruments; b) ambient magnetic field profile versus LAPD port number. The distance between two adjacent ports is 0.32 m. Instruments' typical locations are marked by dashed perpendicular lines.

FIG.3.5 a) illustrates the hardware configurations for this experiment. The origin of the z axis is defined as the location of the lithium fast-ion source (Sec. 2.3.1). The beam-wave interaction region is ~ 10 meters downstream of the cathode to ensure radially uniform background plasma properties. The SAW antenna (Sec. 2.4) is located at z = - 3.52 m to avoid the near field effect (typical SAW wavelength parallel to $\mathbf{B}_0$ is ~ 4 m). The fast-ion analyzer (Sec. 2.5.1) scans fast-ion signals in the x-y plane 0.32 to 0.96 m away from the source to vary the interaction time between wave and particle. FIG.3.5 b) shows the actual LAPD port locations of all the instruments relative to the ambient

magnetic field profile. The distance between two adjacent ports is 0.32 m. One set of magnets next to the anode-cathode carries a higher current corresponding to a 1.4 kG field to avoid strong Alfvén maser formation[5] which is a major source of wave field noise. A dissipating magnetic beach on the north end of the machine is used to suppress reflection of the waves at the end of the machine. The axial magnetic field profiles are calculated from the actual current distribution for all the magnets in the machine[6]. The estimated axial field ripple amplitude at the radius of the machine is less than 2% for a constant field configuration.

3.4.2 Fast-ion Signal Detection

The stainless steel source outer-shield (3" x 5") changes local plasma parameters (especially when the outer shield is grounded to the LAPD chamber as is preferred). A measurement of plasma floating potential (V_f) near the source region shows up to 10 V of decrease, which causes a small adjustment of the beam energy. SAWs launched from inserted antennas can also be influenced if the source is aligned axially with the oscillating current channels that create the wave (Sec. 3.4.4).

A special synchronization between the lithium source and the LAPD plasma is employed, so that the ~ 20 ms fast-ion pulse is turned on and off every two plasma discharges, with an adjustable delay and duration. The background signal is taken when the source is disabled for one shot right after the previous beam-on shot. Even number of shots is repeated at one spatial location before the probe drive moves on. The signals with the source on are subtracted by the signals with the source off. The fast-ion signals shown in this work are net signals with background subtractions.

An electrical diagram for the experiment is shown in FIG.3.6. Apart from the Alfvén Maser signal, which is usually avoided as stated earlier, there exist two major noise sources: the ~ 6 kA plasma discharge pulse causes ringing signals at 1 – 1000 Hz due to capacitive and inductive couplings; the SAW rf driving-circuit generates EM noise outside of the chamber as well as SAW propagation inside the plasma. It is thus very important for the lithium source to have a solid ground reference to the LAPD chamber ground with a complete shield around the heating and biasing circuit. Two Mu-metal shielded high-voltage power supplies[7] bias the emitter and the accel-decel grid at desired voltages with < 0.05% ripple rate (< 0.3 Vpp ripple at 600 V), monitored by a Tektronix P6015A high voltage probe.

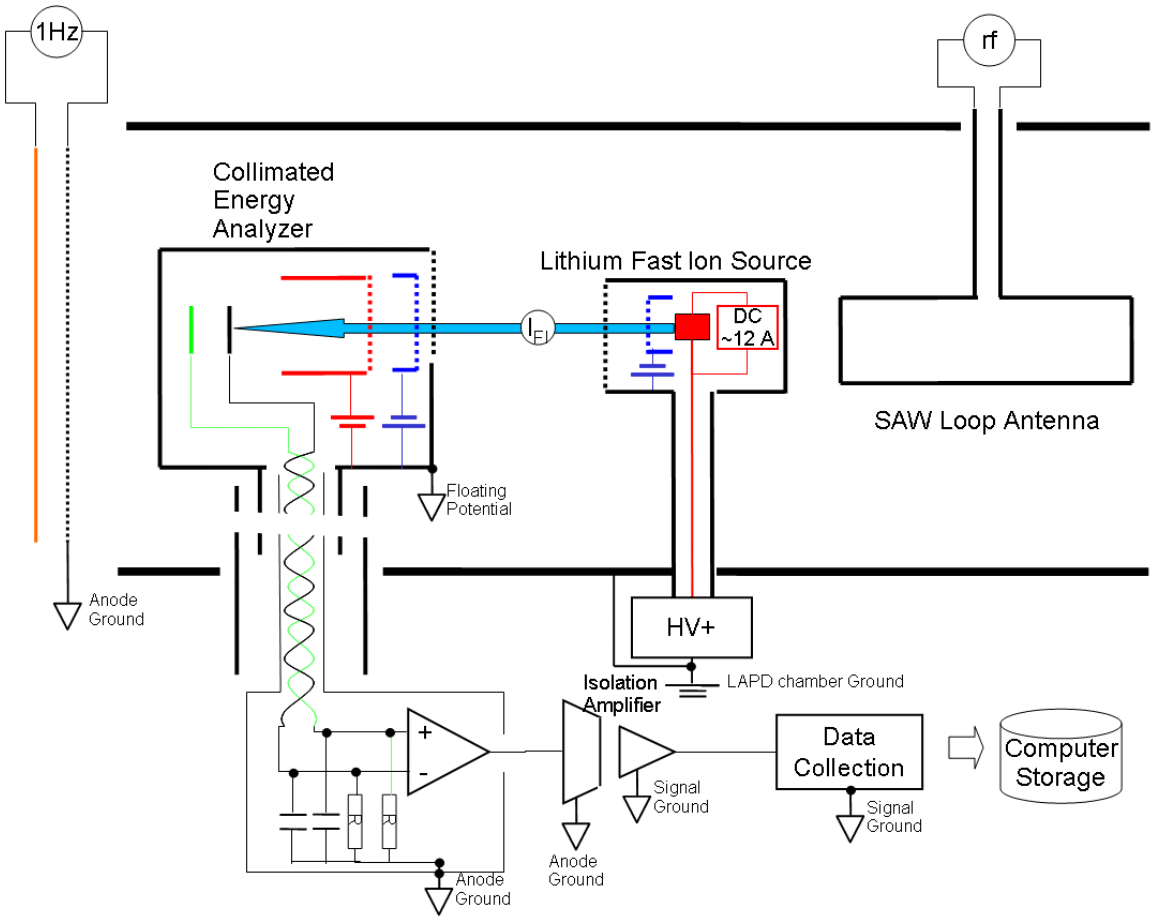

FIG.3.6 Electrical configurations and shielding solutions for fast-ion generation and diagnostics.

(Drawings are topologically correct but not to scale.)

After the beam travels in the plasma/wave fields, a collimated fast-ion analyzer is employed to produce a good fast-ion signal-to-noise under strong rf noise environment during the LAPD discharge. It packages a 3.2 mm dia. collector, an identical dummy for differential amplification and three molybdenum grids for variable electrical barriers. Typical probe current signals are in the 0.1 - 1 μA range at large distances from the ion gun. At operational pitch angles for the source (> 28˚), the tubular housing is directed parallel to the local ion beam trajectory (FIG.3.5 a), in which the collector is recessed by

more than the plasma ion Larmor radii to block thermal particles' entrance geometrically. The second grid is biased positive (~ + 50 V) and the first grid is biased negative (~ - 10 V) to further reject plasma ions and electrons electrically. Another application of the analyzer is to sweep the bias of the second grid up to 800 V to obtain the energy distribution of the ion beam. For a 600 eV beam with a pitch angle of 28°, measured 1" away from the beam exit in the LAPD afterglow plasma, the energy spread (3%) is similar to that measured in a vacuum magnetic field. A continuous low-energy tail in the energy distribution function is observed in the distribution in the presence of the plasma.

The fast-ion current and the dummy pickup signal are fed through a RG 178B/U coaxial cable twisted pair, shielded by the stainless 0.95 cm O.D. shaft. Due to the shaft length that's required by the LAPD standard probe drive as well as a minimum of ~ 1 m for external connection, the total capacitance of each coaxial signal line is ~ 270 pf. For this work, a 1 MΩ input resistance is needed for sufficient fast-ion signal as well as for filtering out strong rf pickups. Signals are pre-amplified by a Lecroy DA1822A differential amplifier. A SONY/Techtronix A6907 optical isolator separates the fast-ion current reference and the data collection ground, reduces the offset caused by the plasma discharge, and amplifies the beam signal for the 100 MHz, 8 bit digitizer.

Measurements of the beam profile and wave field utilize a 2D probe drive system (± 0.5 mm precision) and highly reproducible plasma shots of the LAPD. At each spatial location, multiple time traces are collected with a number of plasma shots repeated. The probe tip is then moved to the next spatial position according to the pre-selected grid and the process is repeated.

The fast-ion signal data and other channels such as the SAW antenna current are

collected simultaneously by a computer controlled digitizer board. A Labview program controls the data collection sequence including timing and triggering, probe driving, and antenna frequency sweeping. HDF5 formatted files are compiled after each data run to document all the fundamental information including the plasma discharge current and density, chamber partial pressures, cathode temperature, interferometer trace and magnetic field configuration. A typical fast-ion profile during the discharge of the LAPD plasma is reconstructed from the data array and shown in FIG.3.7. The collimated fast-ion analyzer has good fast-ion signal-to-noise and spatial resolution.

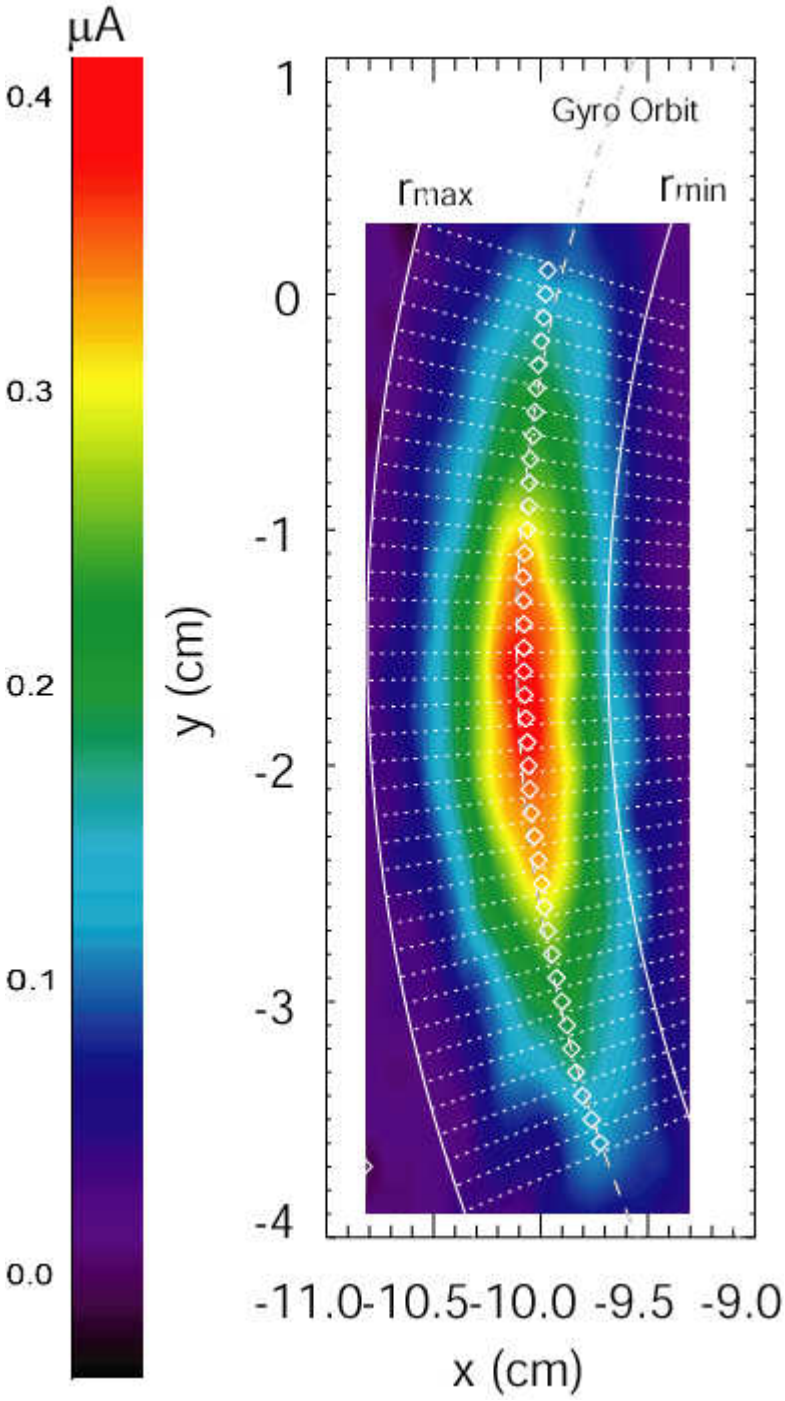

FIG.3.7. A typical lithium fast-ion beam profile during the discharge of the LAPD plasma, with superimposed curves to aid further analysis.
Fast-ion analyzer located at z = 0.96 m. Gaussian center of x profiles: white diamond; Fitted gyro-orbit from Gaussian centers: white-dashed; Radial cuts every 1 degree: white-dotted; Minimum and maximum radial range: white-solid.

3.4.3 SAWs Launched by Loop Antenna

The LAPD's large physical size and sufficiently high plasma density and magnetic field accommodates multiple Alfvén wavelengths. Research on SAW properties in the LAPD dates back to 1994 when pairs of theoretical[8,9] and experimental[10, 11] papers were published on SAWs radiated from small perpendicular scale sources in the LAPD. Subsequently, other mechanisms were discovered to generate Alfvén waves including a variety of inserted antennas, resonance between the LAPD cathode and the semi-transparent anode—the Alfvén Maser[5], and a dense laser-produced plasma expansion[12]. In 2005, Palmer[13] measured thermal ion polarization and $\tilde{\mathbf{E}} \times \mathbf{B}_0$ drifts caused by SAW fields.

To date, there are two different SAW perpendicular modes that are actively launched from inserted antennae in the LAPD. An azimuthally symmetric SAW pattern (m = 0) with $\tilde{\mathbf{E}}_\perp$ along the radial direction can be excited by direct application of an oscillating charge density to a flat, circular mesh (r ~ 0.5 cm) or external feeding of an oscillating current through a thin copper rod parallel to $\mathbf{B}_0$. By adding another identical current channel along $\mathbf{B}_0$ at the opposite phase, a few centimeters away in the *x*-*y* plane, an m = 1 mode can be excited with a linearly polarized $\tilde{\mathbf{E}}_\perp$ region near the center of two current channels.

This work uses an insulated rectangular copper loop[14] as an antenna. It is 30 cm along $\mathbf{B}_0$ and 15 cm along the *y* axis. Currents flowing through the two parallel wires along $\mathbf{B}_0$ generate an m = 1 perpendicular field pattern. The linearly polarized region of

the m = 1 pattern is aligned with part of the gyro-orbit to produce the Doppler resonance effect. FIG.3.8) shows the typical alignment of the Li^+ orbit and the SAW fields in the *x-y* plane, where the resonant fast ion gets a "kick/drag" every time it "swings" by the maximum field region. The geometry and position of the source head is also drawn to show that, for larger gyro-orbit condition, the source head is farther away from the SAW current channels and has less effect on the fields.

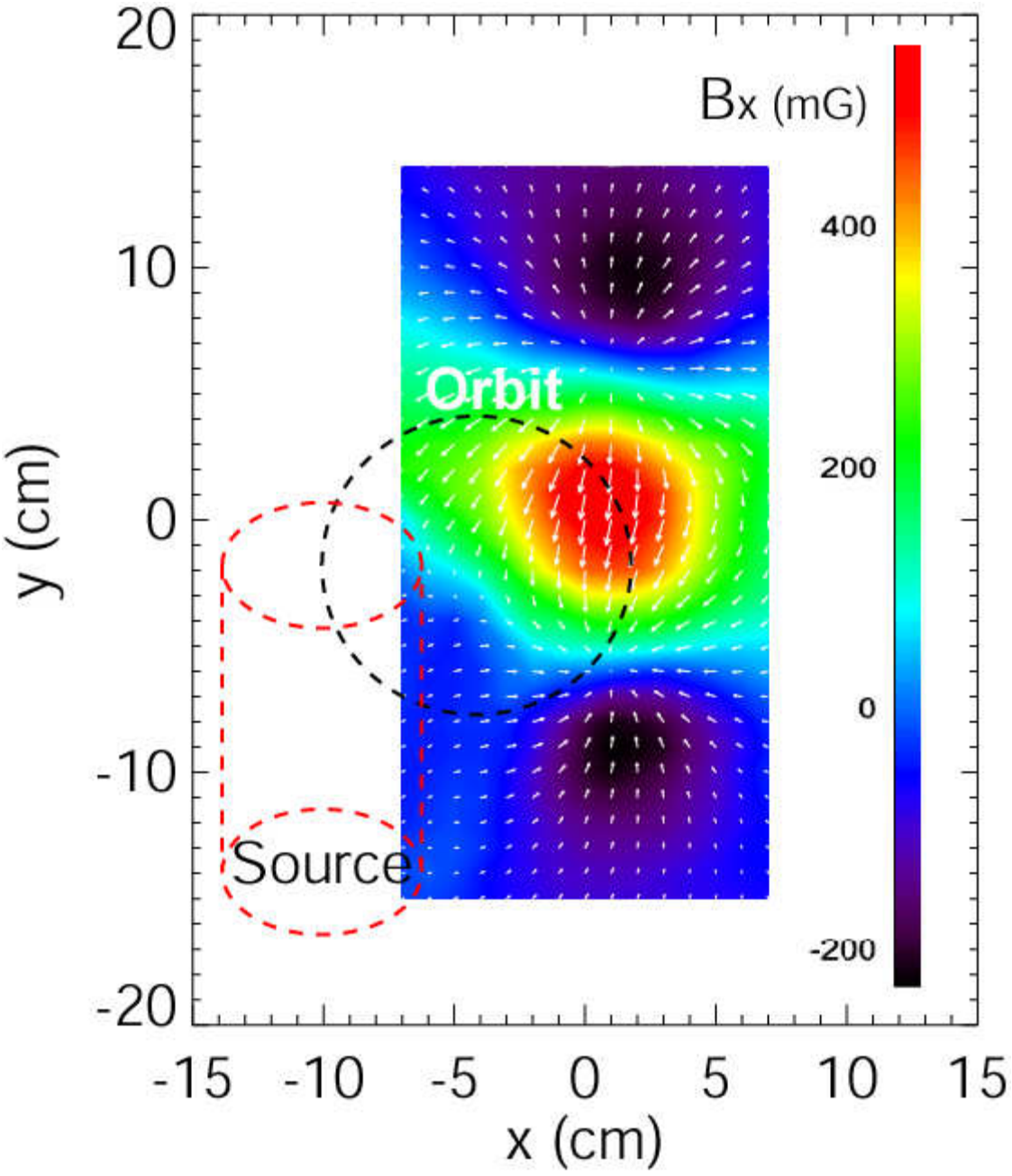

FIG.3.8. Arrangement of fast-ion source (red dashed) and the SAW fields on a perpendicular plane.
Electric field data (white arrows, length proportional to field intensity, maximum at 34.3 V/m) are calculated from measured magnetic field data ($\tilde{B}_x$ shown by color contour) taken at z = 0.64 m. f = 297 kHz. The unperturbed fast-ion orbit is the black dashed circle.

Two different circuits drive the loop antenna. The primary rf supply drives up to 2 kA through the loop and generates Alfvén wave amplitudes up to 10 G at variable frequencies up to 0.8 ω_{ci} (FIG.3.8). An Ethernet controlled Agilent waveform-generator manages the frequency of the output SAWs. The current wave form is triangular and contains harmonics of the fundamental. Since the SAWs are expected to be strongly damped near and above $\omega_{ci,}$[15] the harmonics are usually inconsequential but do affect waves launched at fundamental frequencies lower than 0.3 ω_{ci}. The secondary driving circuit produces a nearly sinusoidal wave form but requires matching capacitors for each SAW frequency. It produces amplitudes up to 1 G. In the following, the default antenna current drive is the triangular one unless otherwise noted.

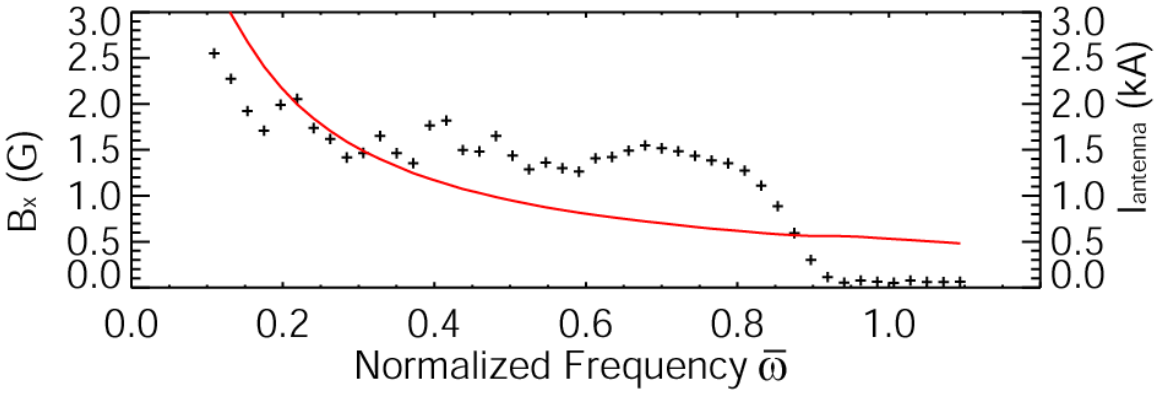

FIG.3.9. Spectra of $\tilde{B}_x$ and loop antenna current by triangular drive.
B-dot probe signal taken at the radial center of z = - 0.32 m during Sep. 2007 LAPD run. (Data acquired with 100 MHz sampling rate, averaging 8 samples and 8 consecutive plasma shots).

The fluctuations of the $\tilde{B}_x$ spectrum (FIG.3.9) as $\bar{\omega}$ varies are due to the field-line-resonance effect studied by C. Mitchell et al.[16, 17]. Although a flaring field at the north end of the machine is configured to reduce this effect (FIG.3.5 b), there are still reflected waves to interfere with the primary waves. The *b-dot* probes measures the linear

addition of all wave fields. Since only the forward wave can satisfy the normal Doppler resonance condition, using the *b-dot* probe measured fields for Doppler resonance calculation would incur systematic error which can be estimated from FIG.3.9.

3.4.4 SAW Perpendicular Pattern

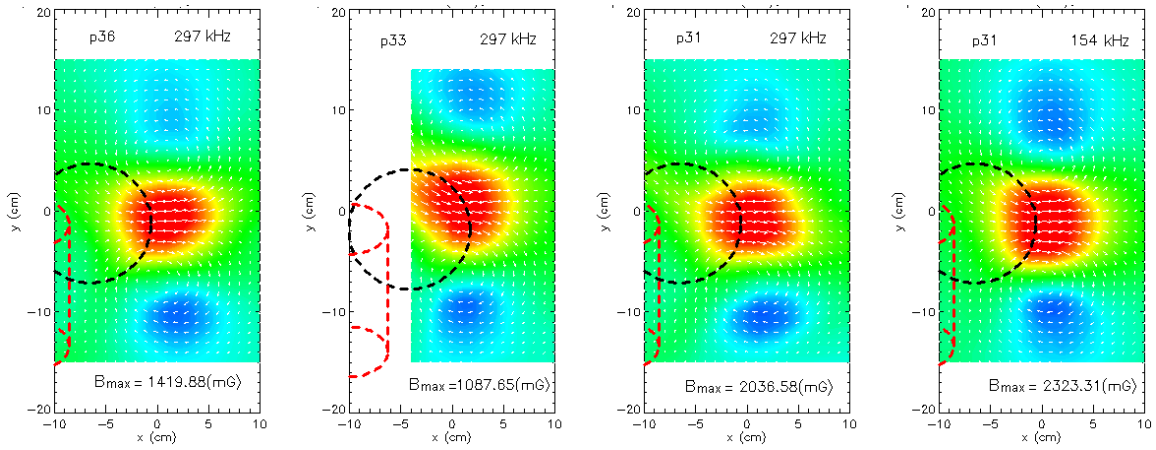

FIG.3.10. Perpendicular SAW magnetic field patterns.
a) port 36 (z = -0.32 m), f = 297 kHz; b) port 33 (z = 0.64 m), f = 297 kHz; c) port 31 (z = 1.28 m), f = 297 kHz; d) port 31 (z = 1.28 m), f = 154 kHz.

B-dot probes plane scans at multiple ports show that the axial variations of the wave field perpendicular pattern are small for the same launching frequency. The influence of the grounded fast-ion source on the wave pattern is noticeable and frequency scans at various frequencies reveal different levels of this effect on the wave pattern near the source. Higher frequency SAWs, corresponding to shorter parallel wavelengths, have more distortion in the wave pattern (FIG.3.10 which section). While a generic wave perpendicular pattern can be employed first to estimate the theoretical resonance effect, simulations using experimental wave field data for different frequencies are still necessary to make careful comparison between theory and experiment (Sec. 3.5.2).

3.5 Resonance Experiment Results

3.5.1 Fast-ion Signal Shows SAW-Induced Transport

As discussed earlier, the ~ 20 ms fast-ion beam pulse is turned on and off every two LAPD plasma discharges. Close to the end of each discharge, the plasma parameters reach the best uniformity in time and space, when the loop antenna drives an adjustable rf current for 0.5 – 0.8 ms, launching SAWs at the specified frequency. When the beam pulse is on, it overlaps in time with the 10 ms LAPD discharge. The data collection time-window opens for 2 ms with ~ 0.5 ms before and after SAW duration. A typical time history of a Doppler resonance experiment is shown in FIG.3.11, with SAWs launched at the resonance frequency (297 kHz for Doppler resonance case III). The triangular wave form of the SAW current is magnified in the inset of FIG.3.11 c). Fast-ion net signals are shown in FIG.3.11 a) and b) where the source is pulsed on for the whole ~ 2 ms window.

The fast-ion signals in FIG.3.11 a) and b) change significantly in intensity, towards different directions, when SAWs propagate to the location of the fast-ion orbit several microseconds after current drives through the antenna. The spatial locations of the two time traces are different: a) is taken at the center of the beam spot whereas b) is near the edge, which are accurately indicated in FIG.3.12. Since the RC time is much longer than the SAW period, fast-ion signal variation at SAW frequency is filtered out. However the averaged beam profile would still widen in the $\hat{r}$ and $\hat{\phi}$ directions, as shown in the Monte-Carlo simulation results (FIG.3.4). With particle conservation in mind, the fast

ions are transported from the center of the beam to the edge, during Doppler resonance. This effect in experiment is shown in FIG.3.11 where the beam center/edge signal decreases/increases when the SAW is turned on. When the SAW is turned off, the signal restores back to the unperturbed values. The green curves in FIG.3.11 a) and b) are the fitted RC decay/rise curves yielding an RC time of 0.3 ± 0.05 ms, which is in agreement with the estimated value.

In the following analysis, the SAW-influenced beam signal uses the averaged signal from 0.6 ms after the onset of the antenna current, shown in FIG.3.11 a) and b) with the red-dashed time window. This average has underestimation of the signal change if the SAW-influence time was infinite, which means the actual fast-ion transport effect in the experiment is up to ~ 8% more significant than shown by the current data. The unperturbed beam signal, as a reference, is the average over the blue-dotted time window before SAW-influence.

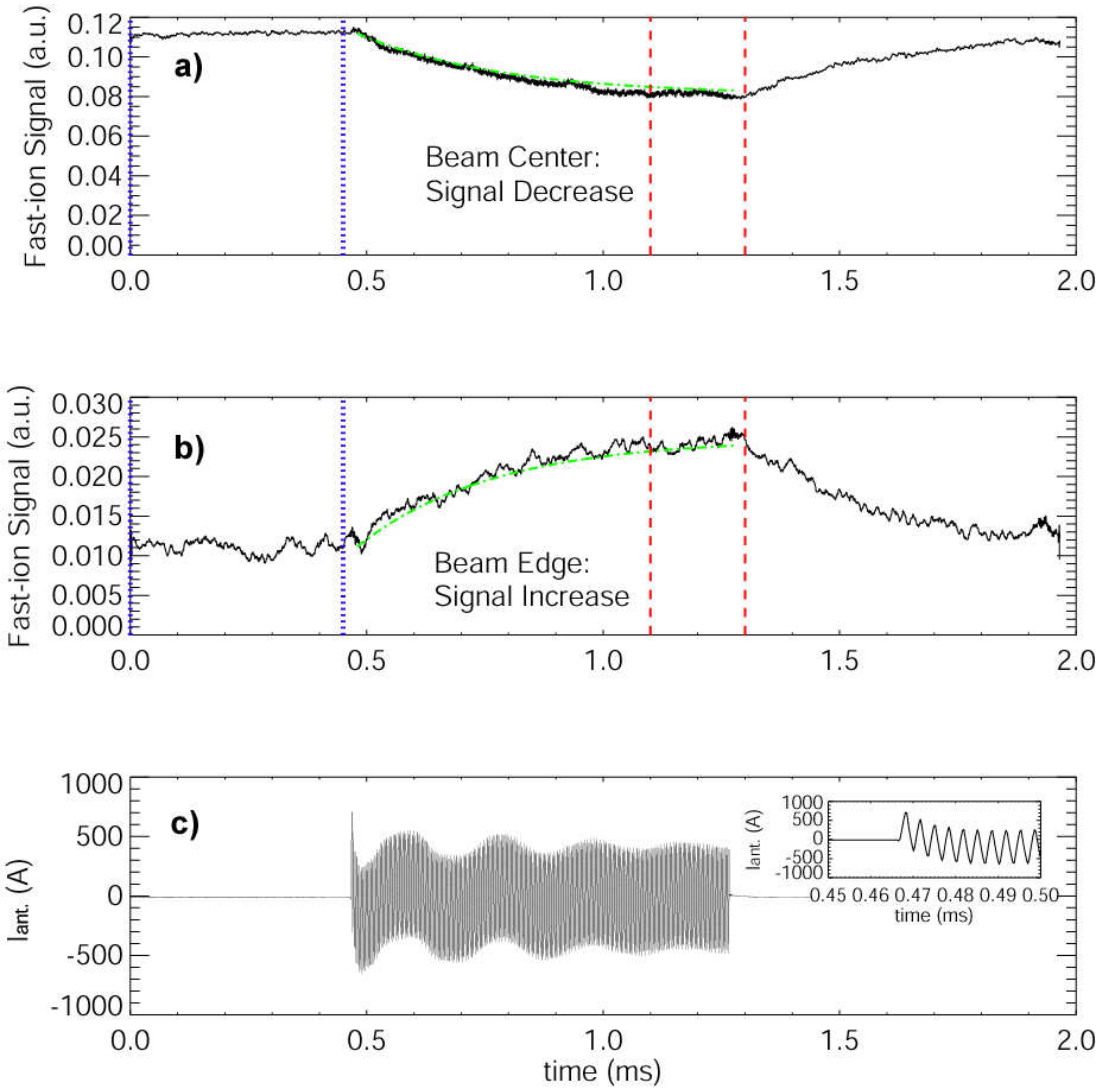

FIG.3.11. Typical fast-ion signal time traces influenced by SAWs at the Doppler resonance frequency.
a) beam center signal RC decay; b) beam edge signal RC rise; c) Loop antenna current. Inset: magnified triangular current signal for the initial 0.5 ms. (SAW frequency 297 kHz; Data acquired with 25 MHz sampling rate, averaging 8 samples and 8 consecutive plasma shots, Dec. 07 LAPD run).

Time traces taken at a selected spatial grid are processed to show the fast-ion beam profile at the *x*-*y* plane. Fast-ion signals with and without SAW influence show significant difference in FIG.3.12, in agreement to the transport effect at resonance frequency. From the 3D visualization in FIG.3.12 a), fast-ion intensity migrates from the center of the beam to the edge, causing widening along the $\hat{r}$ and $\hat{\phi}$ directions. The beam profile

along each direction is acquired using the statistical technique mentioned in Sec. 2.5.1. Both profiles are widened as the SAW is turned on.

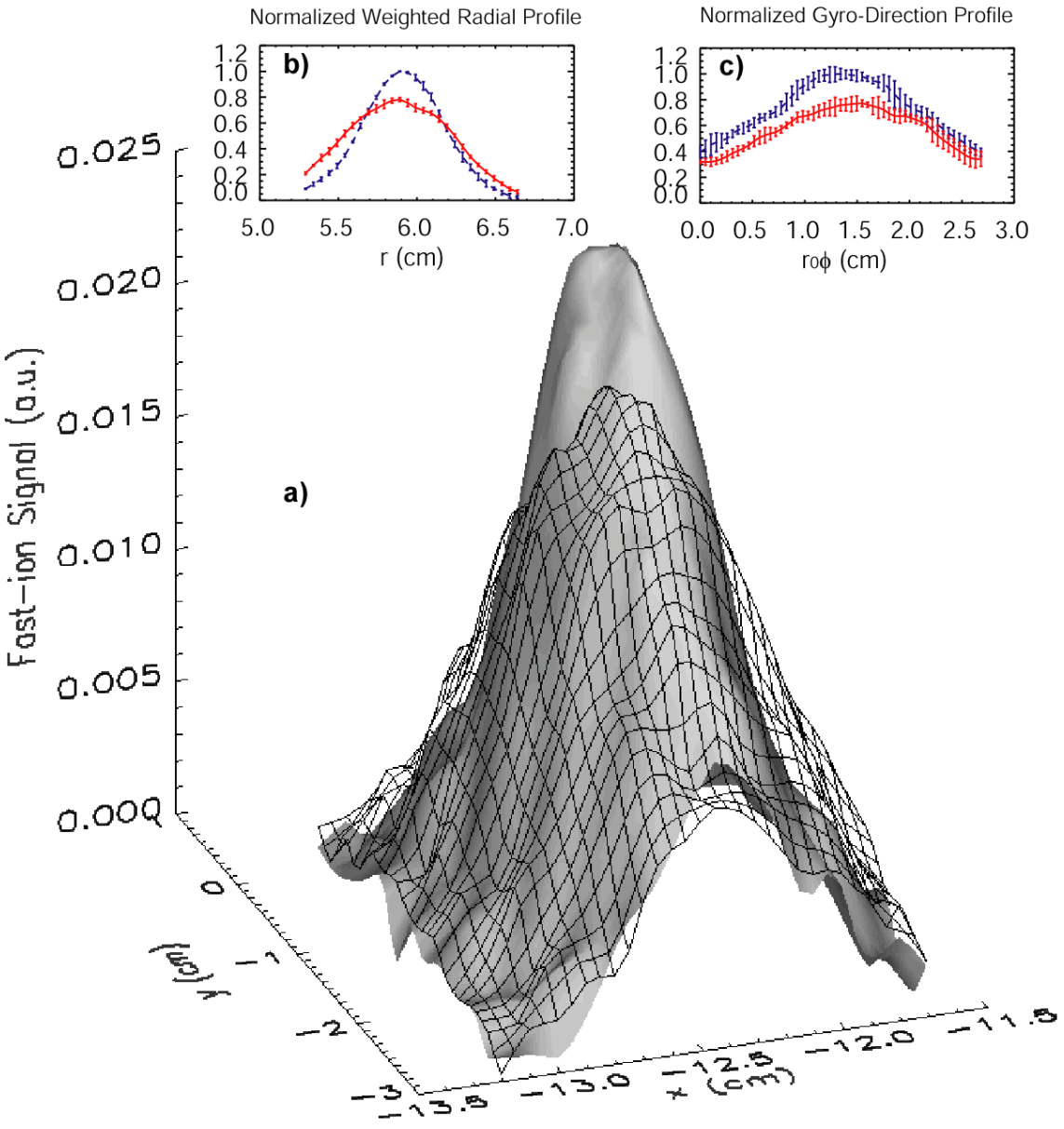

FIG.3.12. Comparison of fast-ion beam profile with and without SAW influence. a) 3D visualization of beam profiles with (gridded surface) and without SAW influence (shaded surface); b) Normalized weighted radial profiles with (red-solid) and without SAW influence (blue-dashed); c) Normalized gyro-direction profiles with (red-solid) and without SAW influence (blue-dotted) (SAW frequency 297 kHz; Data acquired with 100 MHz sampling rate, averaging 8 samples and 10 consecutive plasma shots, Sep. 07 LAPD run).

3.5.2 Measured Doppler Resonance Spectra

In this section, quantitative agreement between the measured and predicted resonant spatial broadening is demonstrated. The resonance spectra of SAW-induced displacements are measured and compared with the theoretical spectra.

Based on the theoretical spectra in FIG.3.2 b), a set of SAW frequencies is selected to cover the important features of the spectra, e.g. peaks and nulls of the resonance. For each of these frequencies, the antenna is driven for multiple plasma shots (8 – 10) and fast-ion signals are taken at the same spatial location. After completing all the frequencies and shots, the fast-ion analyzer is moved to the next point on the *x*-*y* grid. The total time of the spectra measurement is usually kept within 2 hours (~ 1/10 of source lifetime) to avoid significant change in the lithium source performance.

The spatial profile at each frequency is acquired from the data array and analyzed as shown in FIG.3.7. As mentioned in Sec. 3.3, both Δr and $r_0\Delta\Phi$ are measurable indicators of the resonance effect and Δr is more favorable, which corresponds to the change in the perpendicular fast-ion energy. In FIG.3.13 a), a typical set of radial profiles for the selected frequencies (colored) are shown, to which the classical profile (black-dashed) is compared. The fast-ion migrating effect varies as the frequency, which peaks at 0.65 ω_{ci} and diminishes at 0.20 and 0.41 ω_{ci}, as expected from the theory. In FIG.3.13 b) and c), plotted are the frequency dependences of full-width-half-maximum (FWHM) and the beam intensity coefficient (P_0) calculated from the Gaussian fit of the profile:

$$P(r) = P_0 \exp\left(-\frac{(r-r_0)^2}{b^2}\right) + P_c, \tag{3.13}$$

where P is the radial profile, b is proportional to the FWHM and P_c is the background level. It is obvious that the variations of both quantities have similar dependence on $\bar{\omega}$ as expected.

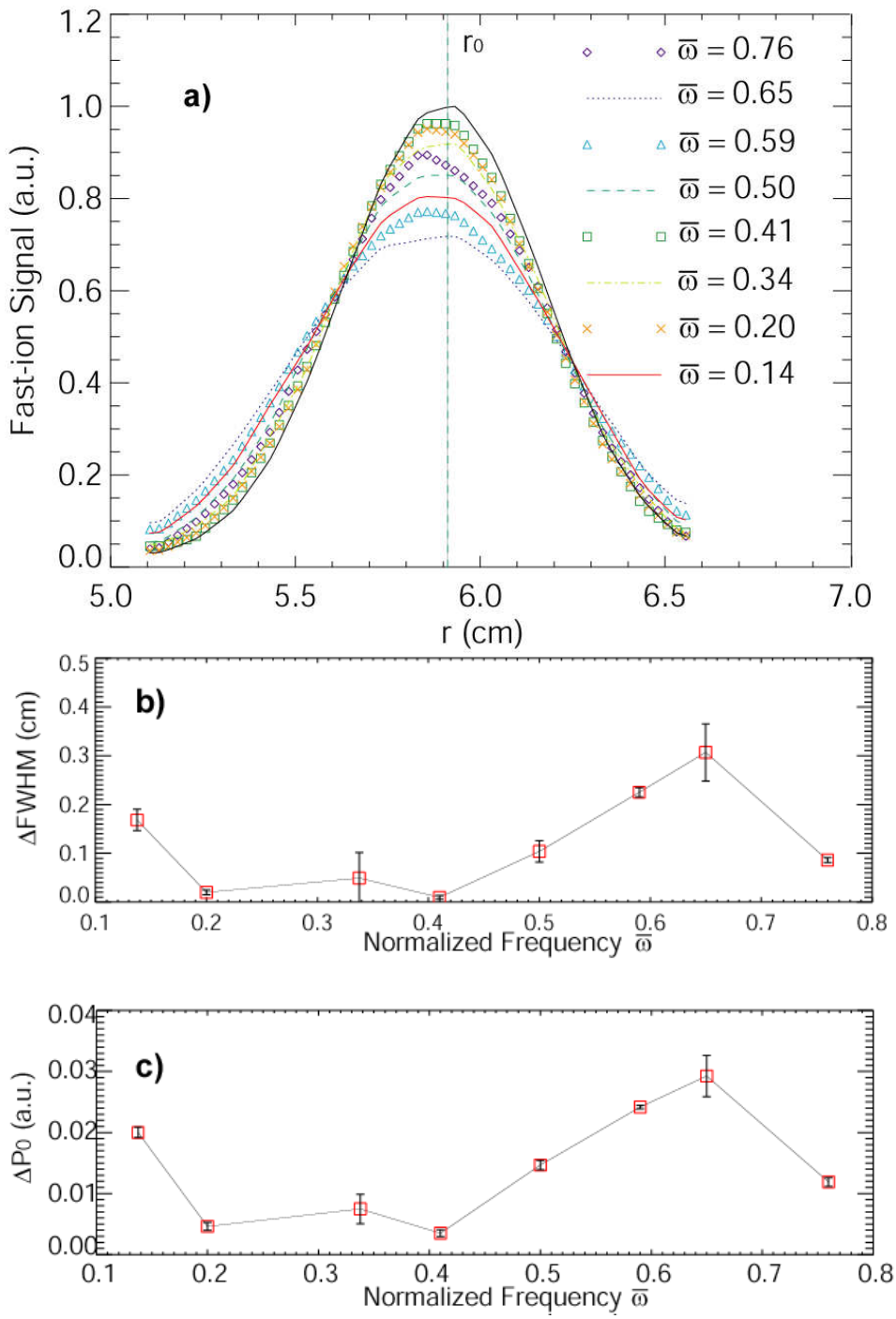

FIG.3.13. a) Fast-ion beam radial profiles with various SAW frequencies (colored lines/symbols) compared to the unperturbed profile (black-solid); b) Changes in FWHM of beam radial profiles versus SAW frequency; c) Changes in Gaussian peak intensity (P_0) versus SAW frequency. (Data acquired with 25 MHz sampling rate, averaging 8 samples and 8 consecutive plasma shots, Dec. 07 LAPD run).

In order to determine Δr quantitatively from the experimental beam profile, the profile WITHOUT SAW is displaced digitally to find an empirical Δr that produces the best fit of a specific profile WITH SAW. The single-particle result in FIG.3.2 a) shows that the fast-ion collection position undergoes elliptical displacements with SAW perturbations at different phases (φ_0). The projection of the SAW displaced beam center (r_{SAW}) along the $\hat{r}$ direction can be thus modeled by:

$$r_{SAW} = r_0 + \Delta r \sin(\varphi_0), \tag{3.14}$$

where r_0 is the classical radial position and Δr is as defined in Sec. 3.1. Then the integration of all the displaced profiles across the region of $\varphi_0 \in [0, 2\pi]$ yields an empirical profile that is dependent on Δr. If such a profile has the best χ^2 fit to a SAW perturbed profile, then the corresponding Δr is regarded as the displacement inferred from experimental data (FIG.3.14). For well-behaved Gaussian distributions like the beam classical profiles in Eq. 3.13, that integration can be written as

$$P(r, \Delta r) = \frac{1}{2\pi} \int_0^{2\pi} \left[P_0 \exp\left(-\frac{(r - r_0 - \Delta r \sin(\omega t))^2}{b^2} \right) + P_c \right] d\varphi_0 . \tag{3.15}$$

This algorithm converges rapidly as φ_0 integration step goes below 2π/100.

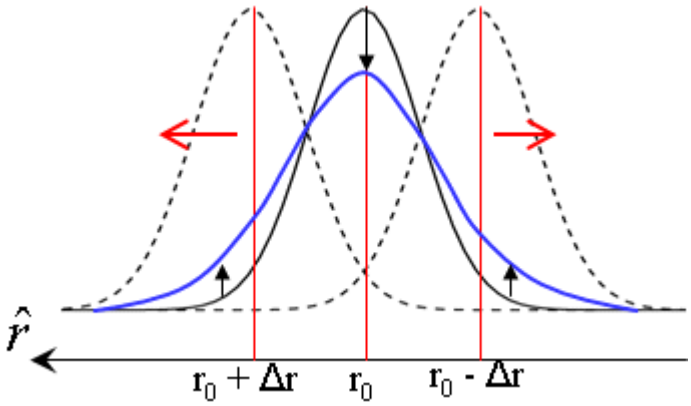

FIG.3.14. Illustration of widened beam spot caused by beam displacement along the $\hat{r}$ direction.

FIG.3.15 shows the Doppler resonance spectra of calculated Δr from measured fast-ion beam profiles. For Doppler resonance case III, two different sets of data acquired during two LAPD runs (Sep. and Dec. 2007) are plotted in FIG.3.15 a), both using the triangular wave drive at similar intensities. The single-particle model using a generic wave field pattern produces the continuous theory curve. The measured wave field amplitude spectrum (FIG.3.9) is used in the simulation. Although slightly different in the wave field strength and the source-antenna arrangement between the Sep. and the Dec. run, the resonance spectrum is similarly characterized by both data sets. The absolute magnitude of Δr shows good agreement between experiment and theory. In FIG.3.15 b), Doppler resonance case II is plotted with its own theoretical resonance curve. Agreement is still good even though this case has smaller fast-ion gyro-radius (3.8 cm) and the source has more perturbation on the SAW field pattern (FIG.3.10).

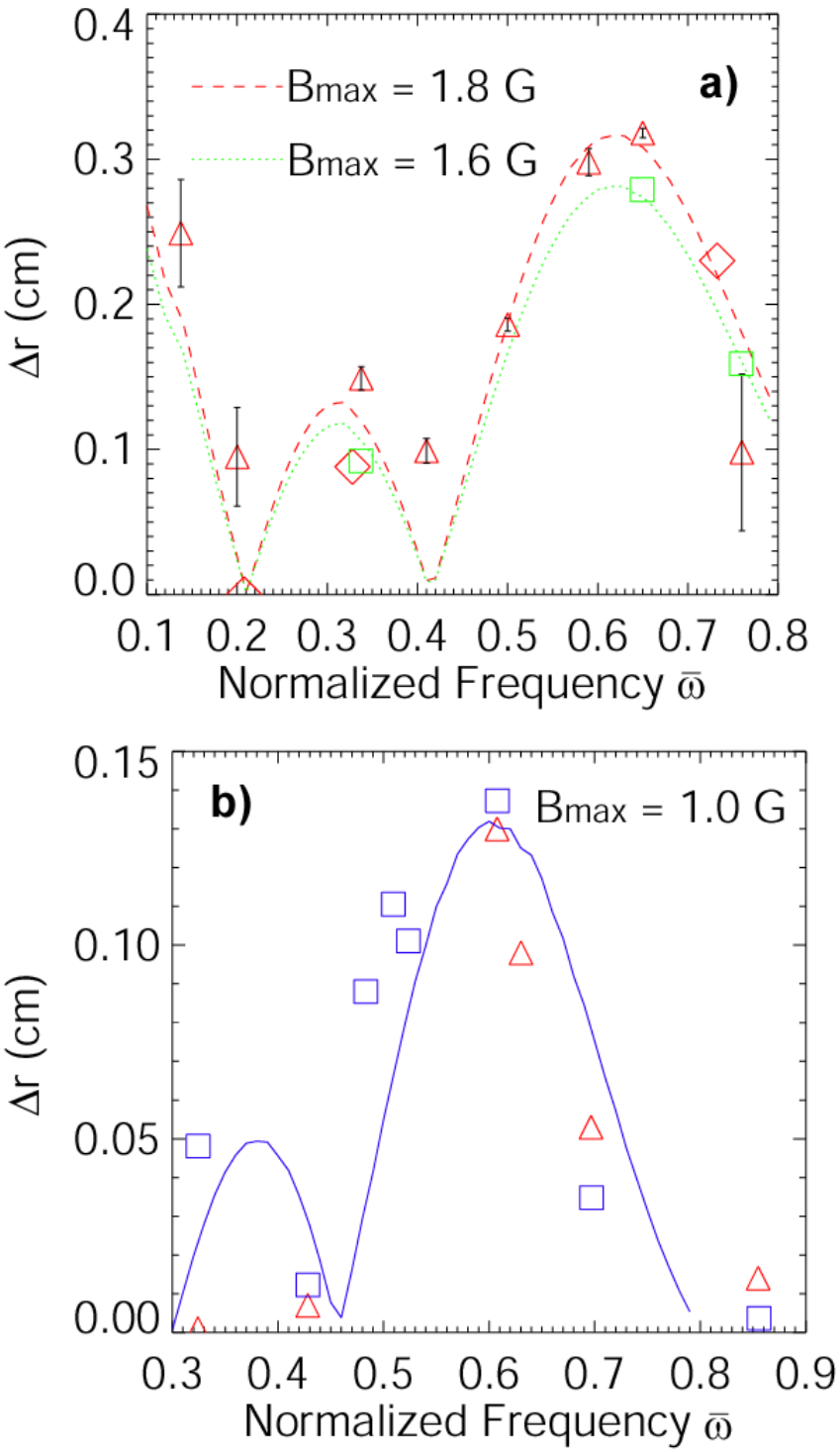

FIG.3.15. Doppler resonance spectra: experimental and theoretical.
a) Doppler resonace case III (ρ = 5.9 cm). B_{max} = 1.8 G (Dec. 2007 LAPD run): red-triangles are data taken with the triangular wave drive; Red-diamonds are sine wave drive. B_{max} = 1.8 G (Sep. 2007 LAPD run): green-boxes are data with the triangle wave drive. b) Doppler resonance case II (ρ = 3.8 cm). (Sep. 2007 LAPD run). Red-triangles: data taken with the triangular wave drive; Blue-boxes: calculated displacements using experimental wave magnetic field data.

The error bars in FIG.3.15 are random errors calculated among data taken at 8 consecutive LAPD shots. During each shot, 5000 samples are averaged to get beam signal at one spatial location, with and without SAW. The highly repeatable plasma-fast-ion-SAW system contributes to the miniscule random errors. Potential systematic errors do exist in this complicated measurement: Source-antenna alignment is routinely done with a telescope through a quartz viewport at the north end of the LAPD with $\pm$ 1 mm error; The *b-dot* probe measurements at multiple ports along fast-ion trajectory ensures the wave perpendicular pattern is centered at the antenna center with $\pm$ 1 cm error; The collection of fast-ion beam integer gyro-cycles away by design shows a strong boundary for the errors in the fast-ion initial mean energy (600 $\pm$ 1 eV)and pitch angle (49.3 $\pm$ 0.2º); The ~ 10 % of fluctuation in wave magnetic field spectrum caused by the field-line-resonance modes. However, none of these above error sources can contribute to the non-linear resonance spectrum in FIG.3.15, especially with the nulls and peaks observed experimentally.

It is obvious in FIG.3.15 a) that, using the triangular-wave antenna drive, Δr does not become a complete null at 0.20 ω_{ci} as predicted by the theory curve assuming single mode SAW fields. As a matter of fact, the triangular waveform of the antenna current and magnetic field contains 2nd (if not perfectly triangular) and 3rd harmonics (FIG.3.16). For $\bar{\omega}$ below 0.5, 2nd harmonic can still be effective, and so does 3rd harmonic for $\bar{\omega}$ below 0.3. The sine-wave drive, although needs different matching capacitance at each frequency, provides clean single mode wave for comparison. The displacements measured with the sine-wave driver at 0.20, 0.33 and 0.73 ω_{ci} are reported in FIG.3.15 a) as red-diamonds. There is a complete null effect for 0.20 ω_{ci}. At 0.73 ω_{ci}, the results from

triangle and sine wave drive are very similar since the higher harmonics are expected to be strongly cyclotron-damped.

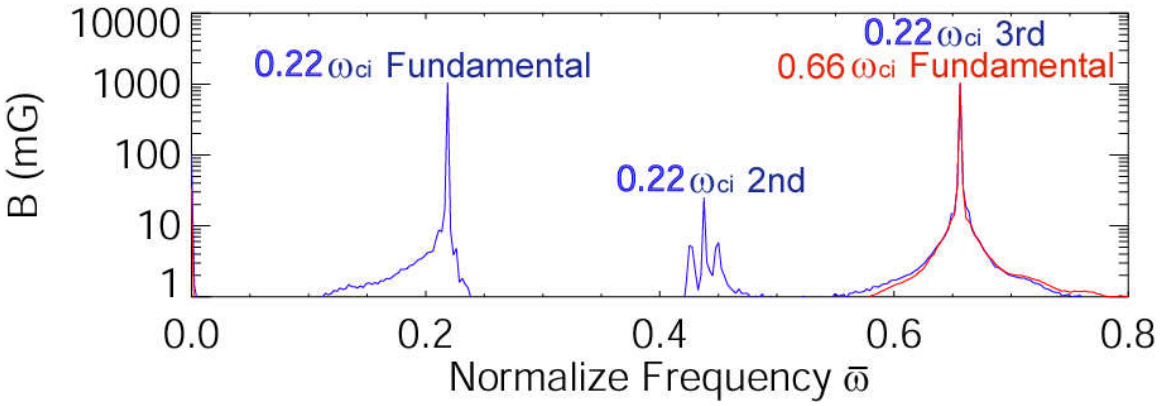

FIG.3.16. Typical FFTs of $\tilde{B}_x$ signal launched by the triangular wave antenna drive.
Blue: $\omega = 0.22\ \omega_{ci}$; Red: $\omega = 0.66\ \omega_{ci}$.

3.5.3 Energy Test of Fast Ion Doppler Resonance

Simulation results also predict that fast-ion beam energy is changed up to ~ 23 eV at the Doppler resonance condition (FIG. 3.17) with 1.6 G wave magnetic field amplitude. The observed beam profile broadenings along the $\hat{r}$ and $\hat{\phi}$ directions are good indicators of perpendicular and parallel energy change. To verify that the wave actually affects the fast-ion energy, the 2nd grid of the fast-ion analyzer is biased at ~ + 480 V relative to the beam energy reference (the LAPD anode) to effectively reject around half of the fast-ion population in the beam energy distribution. The fast-ion signal at the beam center drops to less than half of the one with + 50 V collector bias. The fast ions with insufficient energy to pass the potential barrier in the analyzer will be cut off and the SAW-induced energy change can thus become twice as obvious.

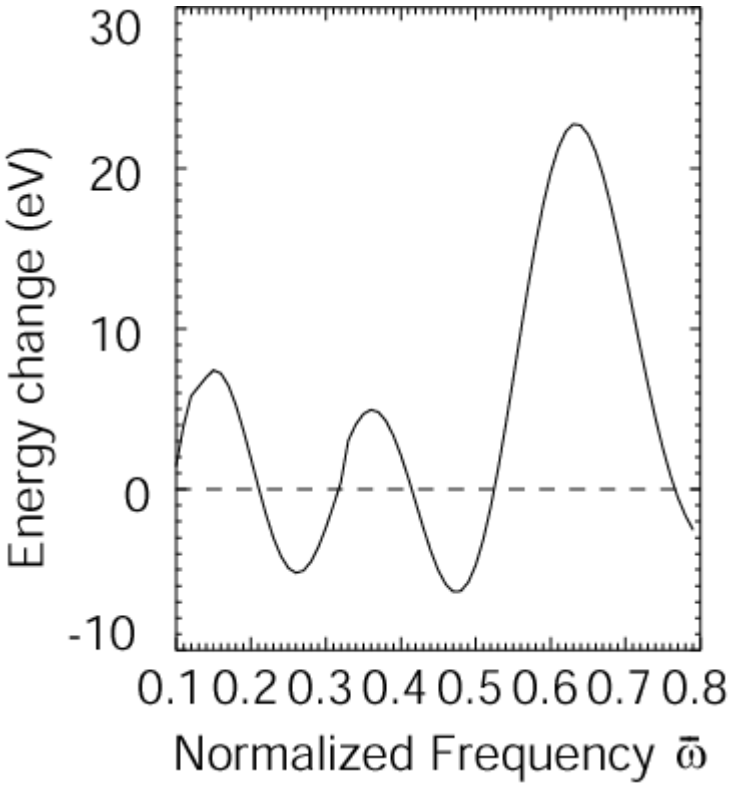

FIG. 3.17. Fast-ion energy change versus $\bar{\omega}$ at resonant frequency (Simulation).

Several experiments with high collector bias were conducted and the results show partial agreements with the theory. It has been established that the collection position is correlated with the energies of the fast ions and their initial distribution in phase space. When SAW is in resonance with the beam, fast ions gaining energy would move to a position with a larger radius (left in the *x*-*y* plane) and lower in gyro-phase. A typical scan is shown in FIG. 3.18 where the SAW perturbed beam profile is shown in a) and its difference with the unperturbed profile is in b). While the fast-ion signal decreased along the gyro direction, there are several spots where signal increased substantially (~ 50 %), where the gyro-radius is higher. One would also expect, at much lower gyro phase (higher energy), stronger fast-ion signals corresponding to the gaining of the fast-ion energy. A complete energy scan at selected beam spot with and without SAW is feasible.

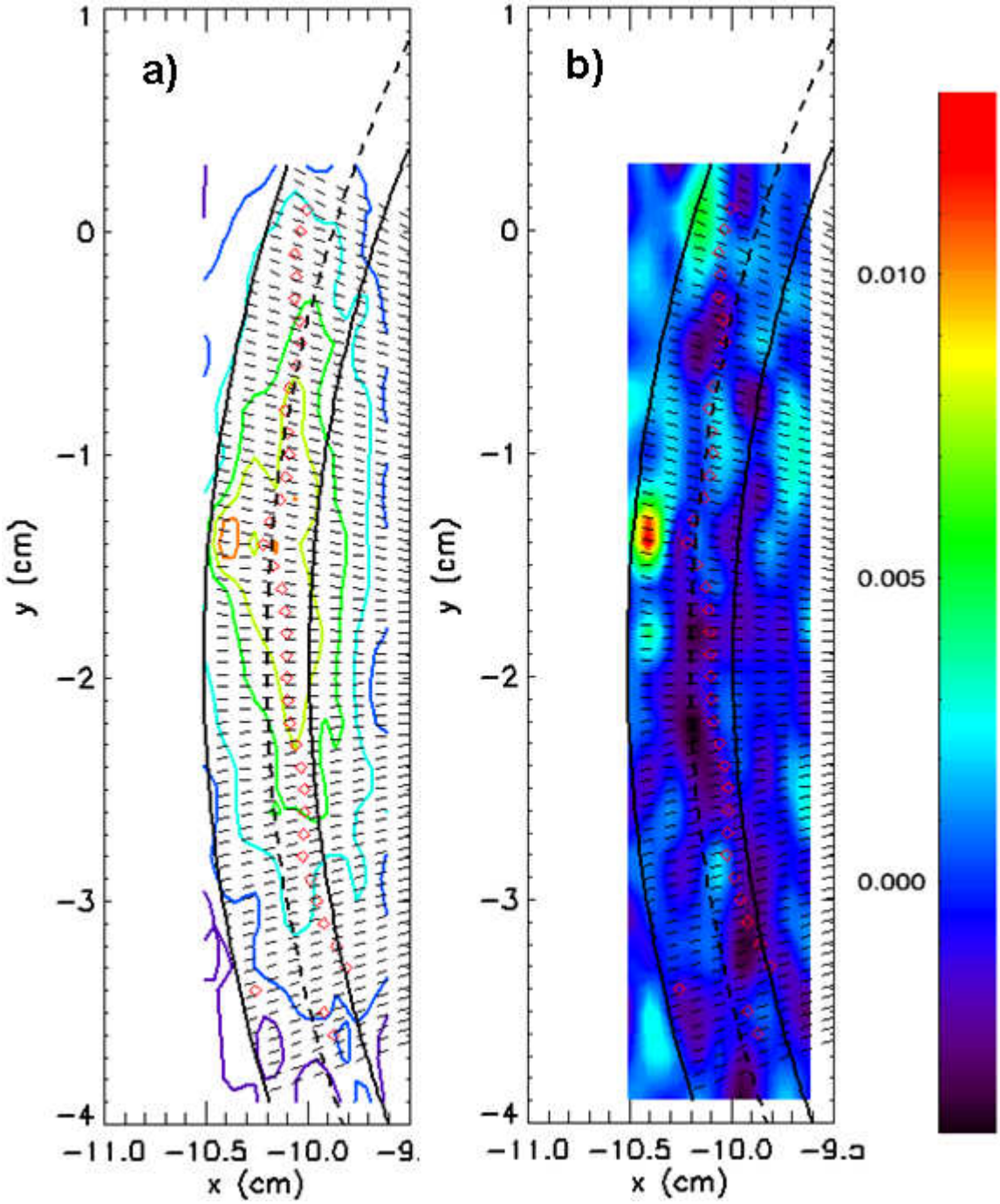

FIG. 3.18 Fast-ion signal detected with collector at high bias (+ 480 V).
a) SAW perturbed fast-ion beam profile; b) Contour plot of the difference of fast-ion signal with and without SAW.

[1] T. H. Stix, *Waves in Plasmas*, (American Institute of Physics, New York, 1992), p238-246.

[2] L. Zhao, Ph. D. thesis, Univ. Cal. Irvine, (2005)

[3] A. H. Boozer, Phys. Plasmas, 9, 4389 (2002).

[4] D. Leneman, W. Gekelman, and J. Maggs, Rev. Sci. Instrum., **77**, 015108 (2006).

[5] J. E. Maggs, G. J. Morales, and T. A. Carter, Phys. Plasmas **12**, 013103 (2005).

[6] S. Vincena, Ph. D. thesis, Univ. Cal. Los. Angeles, (1999).

7 UltraVolt, Inc. High Power "C"/"F" Series High Voltage Power Supply, http://www.ultravolt.com/hicser.htm

[8] G. J. Morales, R. S. Loritsch, and J. E. Maggs, Phys. Plasmas **1**, 3765 (1994).

[9] G. J. Morales and J. E. Maggs, Phys. Plasmas **4**, 4118 (1997).

[10] W. Gekelman, D. Leneman, J. Maggs, and S. Vincena, Phys. Plasmas **1,** 3775 (1994).

[11] W. Gekelman, S. Vincena, D. Leneman, and J. Maggs, J. Geophys. Res. **102**, 7225 (1997).

[12] M. VanZeeland, W. Gekelman, S. Vincena and G. Dimonte, Phys. Rev. Lett. **87** (10), 2673 (1999).

[13] N. Palmer, W. Gekelman and S. Vincena, Phys. Plasmas **12**, 072102 (2005)

[14] T.A. Carter, B.T. Brugman and D.W. Auerbach, CP932, Turbulence and Nonlinear Processes in Astrophysical Plasmas—6th Annual International Astrophysical Conference, edited by D. Shaikh and G. P. Zank© 2007 American Institute of Physics 978-0-7354-0443-4/07

[15] S. Vincena,a) W. Gekelman, and J. Maggs, Phys. Plasmas **8** (9), 3884 (2001).

[16] C. Mitchell, S. Vincena, J. Maggs and W. Gekelman, Geophys. Res. Lett., **28** (5), 923 (2001).

[17] C. C. Mitchell, J. E. Maggs, and W. Gekelman, Phys. Plasmas **9** (7), 2909 (2002).

Chapter 4

SPECTRAL GAP OF SHEAR ALFVÉN WAVES IN A PERIODIC ARRAY OF MAGNETIC MIRRORS

This chapter presents the first experimental observation of an Alfvén spectral gap in a periodic magnetic mirror array.

- Sec. 4.1: motivation and previous studies of Alfvén waves in the LAPD
- Sec. 4.2: analytical results from Mathieu's equation in an infinite magnetic mirror array;
- Sec. 4.3: experimental setup including the mirror array configuration, and plasma and wave diagnostics;
- Sec. 4.4: spectral gap results
- Sec. 4.5: Numerical simulation of the mirror-induced spectral features.

4.1 Motivation

Waves propagating in periodic media have spectra with allowed bands separated by forbidden gaps. This phenomenon was first discussed in 1887[1] by Strutt (Lord Rayleigh) who recognized that it is characterized by the Hill and Mathieu differential equations. One naturally-existing periodic system is a metallic crystal lattice, where the valence electron wave function couples with the one propagating in the opposite direction when the Bragg condition[2] is satisfied as:

$$k = k_n \equiv n\pi / L\,, \tag{1}$$

where k is the wave number, L is the distance between two adjacent ions in the lattice and n is an integer. Two standing wave solutions are formed corresponding to two distinct energy states with a prohibited energy gap in between. For electromagnetic waves, similar propagation frequency gaps occur in many periodic systems, e.g., optical fiber Bragg gratings, Distributed Feedback Lasers (DFL)[3, 4] and waveguide Bragg reflectors[5,6]. When the perfect translational symmetry is disrupted by a defect, e.g., donor/acceptor atoms in a semiconductor or holes in a photonic crystal[7, 8], eigenmodes can exist with frequencies inside the gap.

The propagation of TE and TM waves are treated analytically in a plasma with a stratified density profile in 1968, [9] where the spectral gap and continuum structures are found for both waves. Similar phenomena occur for Alfvén waves in magnetically confined plasmas.[10] The Alfvén speed v_A depends on the magnetic field B_0 and

plasma mass density as $v_A = B_0 / \sqrt{\mu_0 n_i m_i}$, so periodic variations in either the magnetic field or the mass density introduce periodic variations in the index of refraction. Gaps in the shear Alfvén wave spectrum are associated with periodic variations in B_0 caused by toroidicity,[11] elongation[12] or triangularity[13] of flux surfaces, and many other geometrical effects.[14] The bands of propagation between these spectral gaps are called the Alfvén continuum. Excitations in the continuum usually damp rapidly due to phase mixing.

A number of previous studies on Alfvén modes were conducted in the LAPD plasma with different boundary conditions, the results of which this experimental work benefits from. C. Mitchell et al.[15, 16] in 2001 used an impulsive driving current to study the Field-Line-Resonance spectra for a constant magnetic field with strong reflective boundary conditions (a conductive end-plate at one end and the anode/cathode at the other end). A series of Field-Line-Resonance eigenmodes were discovered having frequencies proportional to Alfvén velocity and inversely proportional to the length of the machine with the finite ion cyclotron frequency correction. Later the same year, S. Vincena et al.[17] created a section (~3 m) of magnetic field gradient in the center of the LAPD and studied Alfvén wave propagation in both parallel and perpendicular directions. Upon reaching the cyclotron resonance location in the magnetic field gradient, the wave was almost completely absorbed with no reflection observed. A WKB model was used to find the ray of wave group velocity vectors and estimate the major damping mechanisms. Soon after in 2002, C. Mitchell et al.[18] expanded the magnetic field gradient to ~ 9 meters and perpendicular SAW refraction was characterized as the Alfvén wave traveled from the KAW ($\overline{\beta}_e \approx 10$) to the IAW ($\overline{\beta}_e \approx 0.003$) region.

4.2 Spectral Gap Analytical Theory

In this section, the expected generation of the spectral gap by a magnetic mirror array field is estimated from the electromagnetic wave equations. Consider a periodic magnetic field given by:

$$B_{0z} = \frac{B_{\max} + B_{\min}}{2}\left(1 - M\cos\left(\frac{2\pi}{L_m}z\right)\right), \tag{4.1}$$

where L_m is the mirror length and $M = (B_{\max} - B_{\min})/(B_{\max} + B_{\min})$ is the mirror depth. The refraction index for SAW is

$$N^2 = \frac{c^2}{\mathrm{v}_A^2} = \frac{n_i m_i}{B_{0z}^2 \varepsilon_0} >> 1, \tag{4.2}$$

where c is the speed of light and ε_0 is the vacuum permittivity. Substituting (4.1) into (4.2) gives

$$N^2 = \frac{4n_i m_i}{(B_{\max} + B_{\min})^2 \varepsilon_0}\frac{1}{\left(1 - M\cos\left(\frac{2\pi}{L_m}z\right)\right)^2} \sim \frac{\varepsilon_p}{\varepsilon_0}\left(1 + 2M\cos\left(\frac{2\pi}{L_m}z\right)\right), \tag{4.3}$$

for weak modulation amplitude ($M << 1$), where $\varepsilon_p \equiv 4n_i m_i / (B_{\max} + B_{\min})^2$.

The wave equation for the transverse electric wave field is

$$\nabla_{//}^2 E_y(z) + \omega^2 \mu_0 \varepsilon_0 N^2 E_y(z) = 0. \tag{4.4}$$

The magnetic field can be obtained from Maxwell's equations. Using a dimensionless variable $\xi = \frac{\pi z}{L_m}$, Eq. (4.4) is cast into the form of the canonical Mathieu's equation[19]:

$$\frac{d^2}{d\xi^2}E_y + (a - 2q\cos(2\xi))E_y = 0, \tag{4.5}$$

where the two coefficients are respectively,

$$\begin{cases} a = \left(\frac{L_m}{\pi}\right)^2 \left(\omega^2 \mu_0 \varepsilon_p\right) = \left(\frac{f}{f_{Bragg}}\right)^2 \\ q = -\left(\frac{L_m}{\pi}\right)^2 \left(\omega^2 \mu_0 \varepsilon_p\right) M = -aM \end{cases}. \tag{4.6}$$

The ideal Bragg frequency is defined as $f_{Bragg} = \frac{\bar{v}_A}{2L_m}$, at which the Bragg condition is satisfied and the wave propagation is suppressed by multiple reflections from the mirror cells. Here the average Alfvén speed $\bar{v}_A$ is used and $k_{Bragg} = \frac{\pi}{L_m}$. Using the power series for *a* and *q* from Ref. [19], with mode number *n* = 1, there are two branches of solutions as:

$$\begin{cases} a_+ = 1 - q - \frac{q^2}{8} ... \\ a_- = 1 + q - \frac{q^2}{8} ... \end{cases}. \tag{4.7}$$

Dropping the nonlinear terms and solving for the upper and lower continuum eigen-frequencies by inserting (4.6) into (4.5) gives

$$\begin{cases} \frac{f_+}{f_{Bragg}} = \sqrt{\frac{1}{1-M}} \\ \frac{f_-}{f_{Bragg}} = \sqrt{\frac{1}{1+M}} \end{cases}. \tag{4.8}$$

Thus the width of the SAW spectral gap is

$$\Delta f = f_+ - f_- \approx M f_{Bragg}, \tag{4.9}$$

which varies linearly with the field modulation amplitude *M* of an infinite magnetic mirror array. There are two major premises for this result: infinite number of mirror cells and a much-less-than-unity *M*—both are experimentally difficult to implement. Nevertheless, Eq. (4.9) provides qualitative guidance for the following experimental studies.

An alternative treatment of this problem also reveals that the coupling between the forward and backward waves causes the spectral gap just as in other physical environments. In the case of shear Alfvén waves propagating parallel to a constant magnetic field, the dispersion relations for forward and backward waves are $\omega_{\pm} = \pm k_{//} \mathrm{v}_A$. If the backward wave is purely contributed by reflections from a periodic magnetic mirror array, the dispersion relation is modified to be $\omega_{-} = -\left(k_{//} - 2k_{Bragg}\right)\mathrm{v}_A$ in order to satisfy the conservation of momentum at $\omega = 0$. They are shown as two intersecting lines in a $\omega - k_{//}$ plot as in FIG. 4.1. The coupling of these two waves can be formally described by equating the product of their dispersion relations with a coupling term CT[20]

$$(\omega - k_{//}\mathrm{v_A}) \times (\omega + (k_{//} - 2k_{Bragg})\,\mathrm{v_A}) = CT\,. \tag{4.10}$$

Solving for ω yields two similar branches of solutions:

$$\omega_{\pm} = k_{Bragg}\mathrm{v}_A \pm \sqrt{(k_{//} - k_{Bragg})^2 \mathrm{v}_A^2 + CT}\,. \tag{4.11}$$

At the Bragg condition, k = k_{Bragg}, this frequency gap is given by

$$\Delta\omega = 2\sqrt{CT}\,. \tag{4.12}$$

Choosing a specific value for $CT \sim \omega^2_{+}$, a coupled dispersion relation is plotted in FIG. 4.1, which demonstrates both the forbidden gap and the forward and reflected branches *at* $k = k_{\mathrm{Bragg}}$.

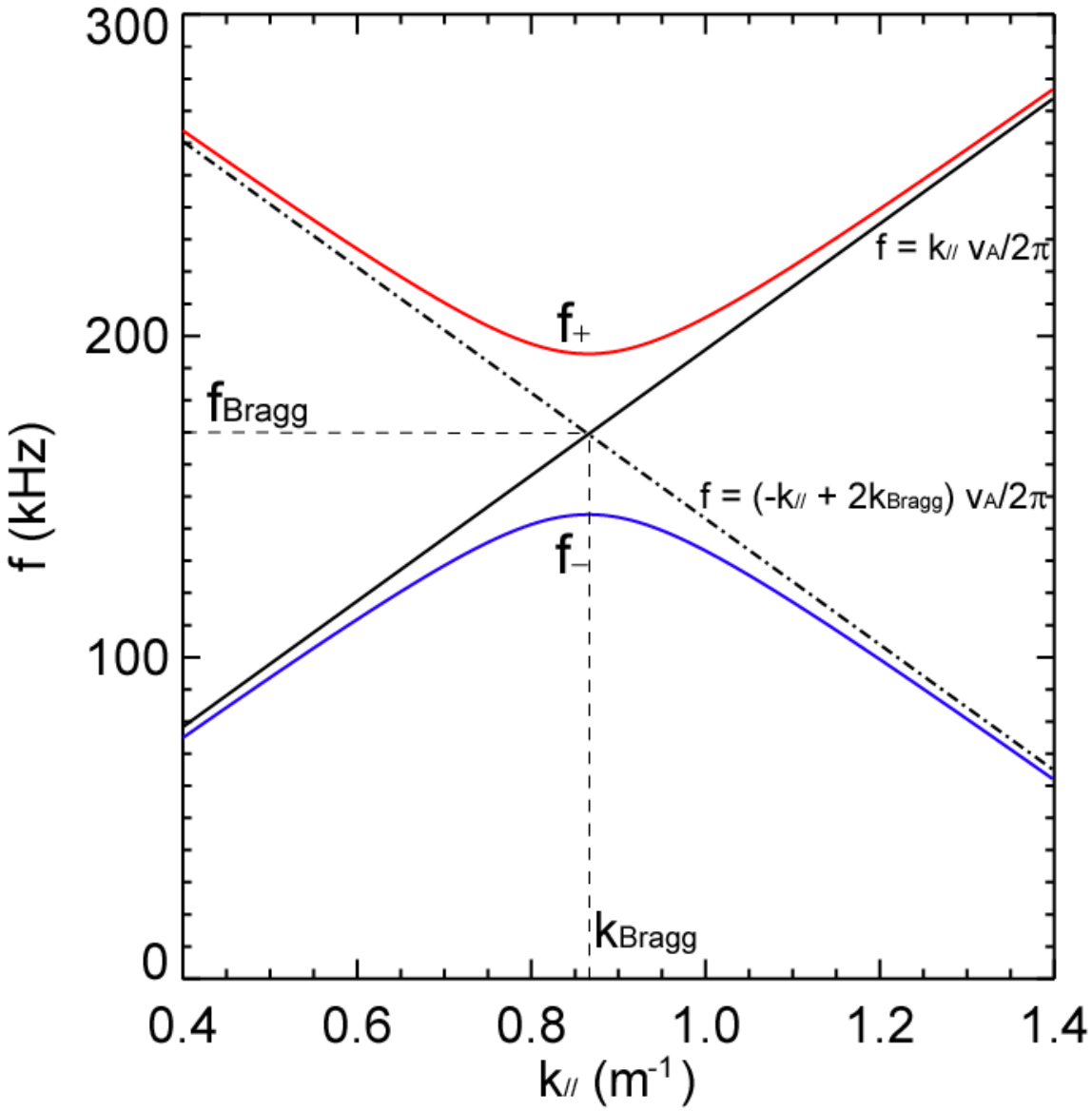

FIG. 4.1. Illustration of coupled shear Alfvén wave in an infinite magnetic mirror array configuration.
Parameters used for calculation are: $CT = (2\pi \times 25\text{x}10^3)^2$ (s^{-2}), $L_m = 3.63$ (m), $v_A = 1.23 \times 10^6$ (m/s).

4.3 SAW Spectral Gap Experimental Setup

4.3.1 Mirror Array in the LAPD

The upgraded LAPD main vacuum chamber is surrounded by ten sets of pancake

electromagnets (90 in total) fed by ten independent power supplies—this offers a maximum of five magnetic mirror cells (each cell requires two sets of magnets). Typical average plasma parameters for mirror array experiments are $n_i \sim 1 \times 10^{12}$ cm^{-3}, $T_e \sim 6$ eV, $T_i \sim 1.0 \pm 0.5$ eV. The low plasma density is chosen to avoid strong Alfvén maser formation as a major source of wave field noise. The working gas is helium at a partial pressure ~ 1.6×10^{-6} Torr with less than 3% of impurities.

FIG. 4.2 shows the baseline mirror array configuration ($M = 0.25$) for this experiment together with the axial arrangement of SAW antennas and plasma/wave diagnostics. This figure serves as a reference of relative z positions for the port numbers mentioned throughout Chapter 4. The two sets of magnets next to the anode-cathode (south) are both carrying the higher current corresponding to a 1.5 kG field to sustain a steady plasma discharge, which leaves four and a half mirror cells available to form the array. A strong dissipating magnetic beach on the north end of the machine was initially included in the mirror array field design to suppress the cavity modes that would otherwise overlap with multiple-mirror induced modes. The axial magnetic field profiles are calculated from the actual current distribution for all the magnets in the machine[21]. The estimated axial field ripple amplitude at the radius of the machine is less than 2% for a constant field configuration.

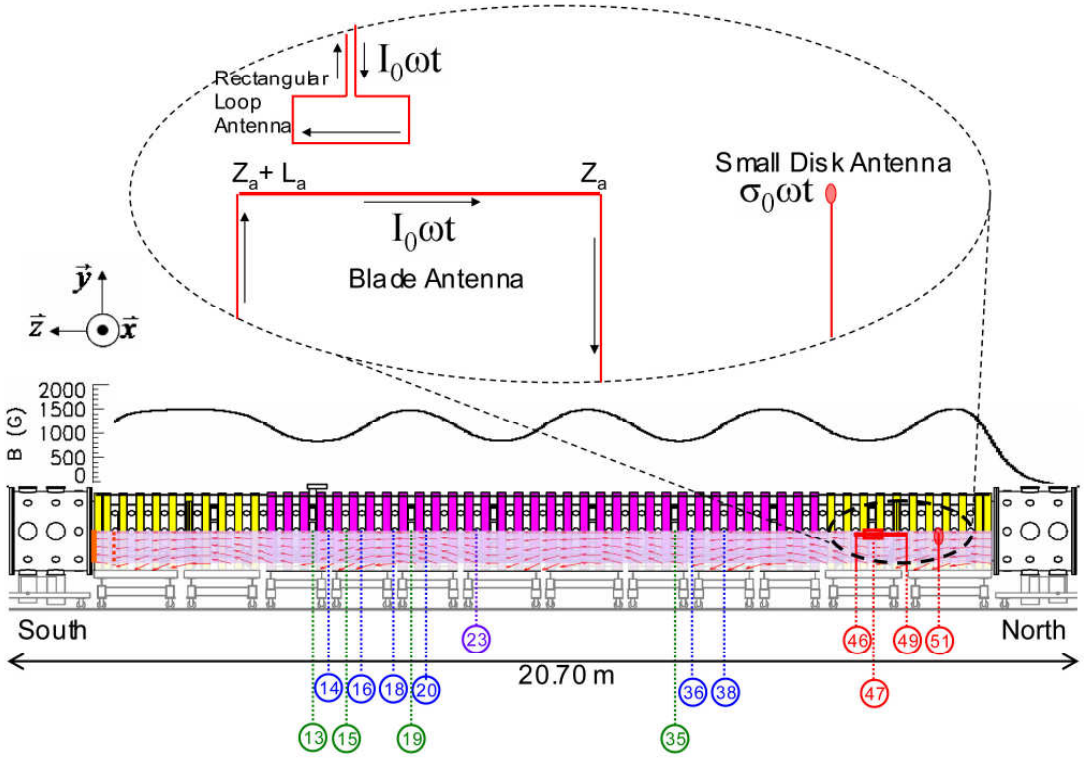

FIG. 4.2. Side view of the baseline mirror array configuration (M = 0.25) at LAPD (lower half of the chamber is semi-transparent).
Red arrows illustrate the vectors (not to scale) of mirror magnetic field. Circled numbers indicate port numbers of inserted instruments. Axial distance between two adjacent ports is 0.32 meter. Port 23: Microwave interferometers for column integrated plasma density calibration; Port 13, 15, 19, 35: Triple probes for local T_e, n_i measurements; Port 51: SAW small disk antenna; Port 46-49: SAW blade antenna; Port 47: rectangular loop antenna; Port 14, 16, 18, 20, 36, 38: B-dot probes for local SAW magnetic field measurements.

Since the LAPD was not previously diagnosed for a magnetic mirror array, plasma parameter (n_i, T_e) profiles from triple Langmuir probe scans are examined before and monitored during the SAW experiment to ensure that the plasma column is only slightly perturbed by the mirror field. Chamber-wide (1 cm step for 96 cm) line scans along the x axis (FIG. 4.2) are taken at port 13, 15, 19 and 35 with the baseline mirror array configuration (M = 0.25). A stationary 56 GHz interferometer at port 23 measures the real time line-integrated plasma density which is used to calibrate triple probe data.

Plasma density and temperature data are then used to calculate the thermal electron velocity, the local Alfvén speed and $\overline{\beta}_e$. FIG. 4.3 shows the calculated quantities along a horizontal line (y = 0) to represent the radial profiles assuming azimuthal symmetry. Comparing data of port 19 (B_{0max}) to port 13 (B_{0min}), the difference in v_A and $\overline{\beta}_e$ are due to the difference in local magnetic field. Port 35 (B_{0min}) data are also plotted next to those of port 13 (B_{0min}) to demonstrate the plasma uniformity along the z axis. $\overline{\beta}_e$ alternates to be above and below 1.0 as external B field changes between B_{0min} and B_{0max}, which implies that the shear Alfvén waves alternate between the kinetic ($\overline{\beta}_e > 1$) and the inertial ($\overline{\beta}_e < 1$) regime.

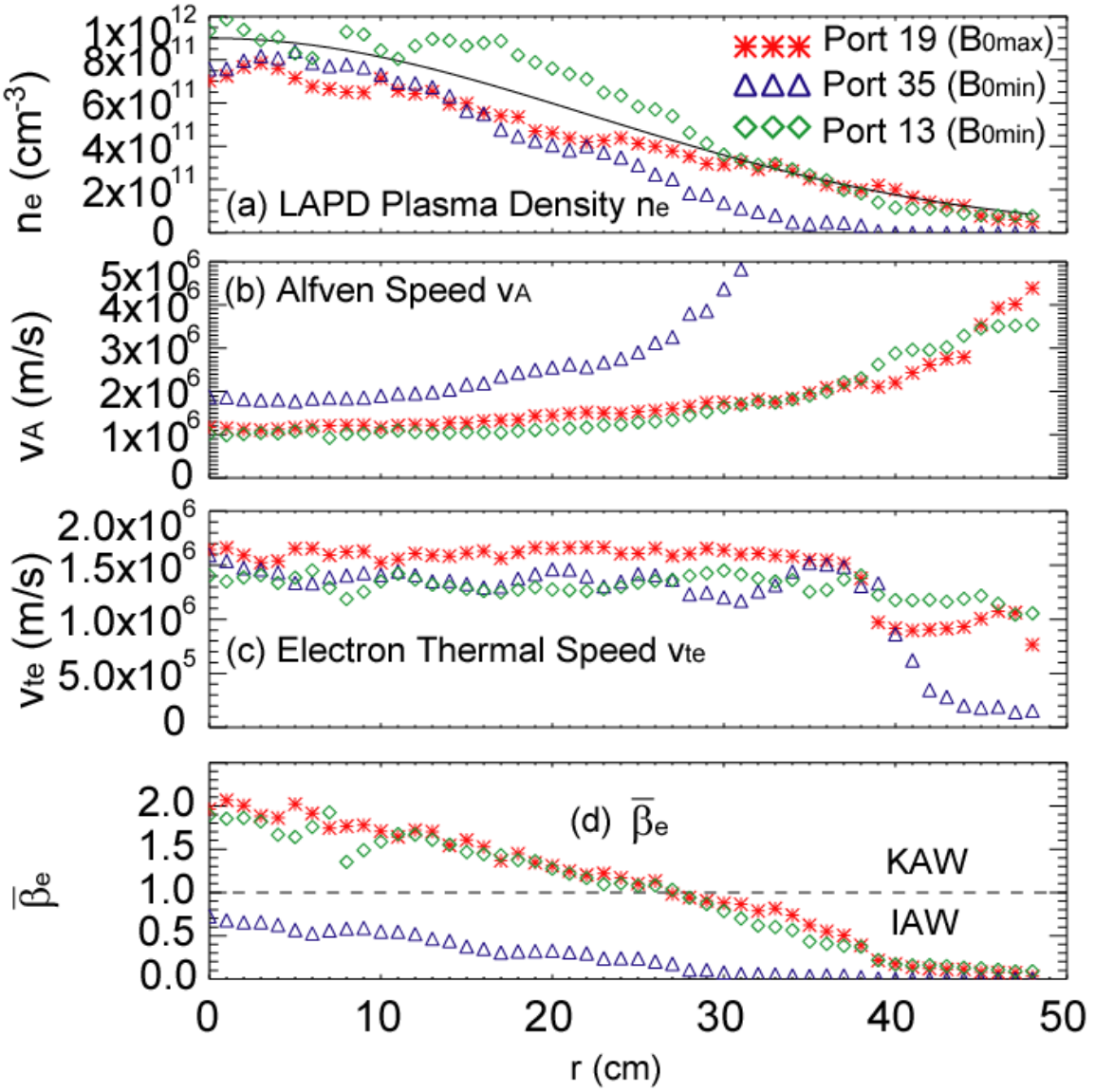

FIG. 4.3. Radial profiles of plasma properties.
a) the plasma density $n_e \sim n_i$, solid curve is a fit using $n(r) = 9\times10^{11} \exp[-1.02\times10^{-3} r^2]$ (cm^{-3}); b) the Alfvén speed v_A; c) the electron thermal speed v_{te} and d) $\bar{\beta}_e$, dashed line shows $\bar{\beta}_e = 1$. All in the LAPD baseline mirror array configuration ($M = 0.25$). Triple probe data including n_i and T_e are acquired with 50 MHz sampling rate of the digitizer, averaging 128 samples and 10 plasma shots. Random error < 10 %.

4.3.2 Launching SAWs in the Magnetic Mirror Array

As depicted in FIG. 4.2, three different antennas are individually placed at the radial center of the cylindrical plasma column where the axial location of each antenna is defined to be $z = 0$ for each probe. The advantage of studying axial (parallel) periodicity-induced SAW spectra with various antennas and launching mechanisms is to exclude any spectral features controlled by the physical characteristics of the antenna. The disk and rectangular loop antenna are used only for preliminary studies of this work and the spectral results are similar to those using the blade antenna. Unless otherwise specified, all experimental results here are from the blade antenna.

During the experiment, the SAW antenna is driven by a rf sine wave train of ~ 200 periods at one frequency for a desired number of shots before changing to the next frequency. A frequency scan from 75 kHz to 275 kHz with a step size of 5 kHz is typical. The antenna current is found to be frequency dependent, steadily decreasing from 8.5 A at 25 kHz to 2.0 A at 325 kHz (FIG. 4.6). Measurements of the forward and reflected power show that resonances in antenna coupling are absent over this frequency range.

Relative wave amplitudes ($\tilde{B}_\theta / B_0$) of up to 10^{-4} are observed 3.2 meters away from the antenna. That distance is approximately half a SAW wavelength (near field influence range) in uniform field LAPD plasma with an intermediate frequency. The wave activity is in the linear response regime, which is a precondition for the following discussions of spectral features.

FIG. 4.4 shows typical $\tilde{B}_\theta$ amplitude (averaged over 0.02 ms) radial profiles at port 14 (axial distance from the antenna south end to the probe Δz = 10.24 m) comparing two background field configurations: uniform field and baseline mirror array configuration (M = 0.25). These profiles match the prediction of Eq. (1.3) with peak wave field amplitude ~ 5 cm away from the minimum. With the magnetic mirror array, the wave field drops drastically near f_{Bragg} ~ 159 kHz (L ~ 3.63 m).

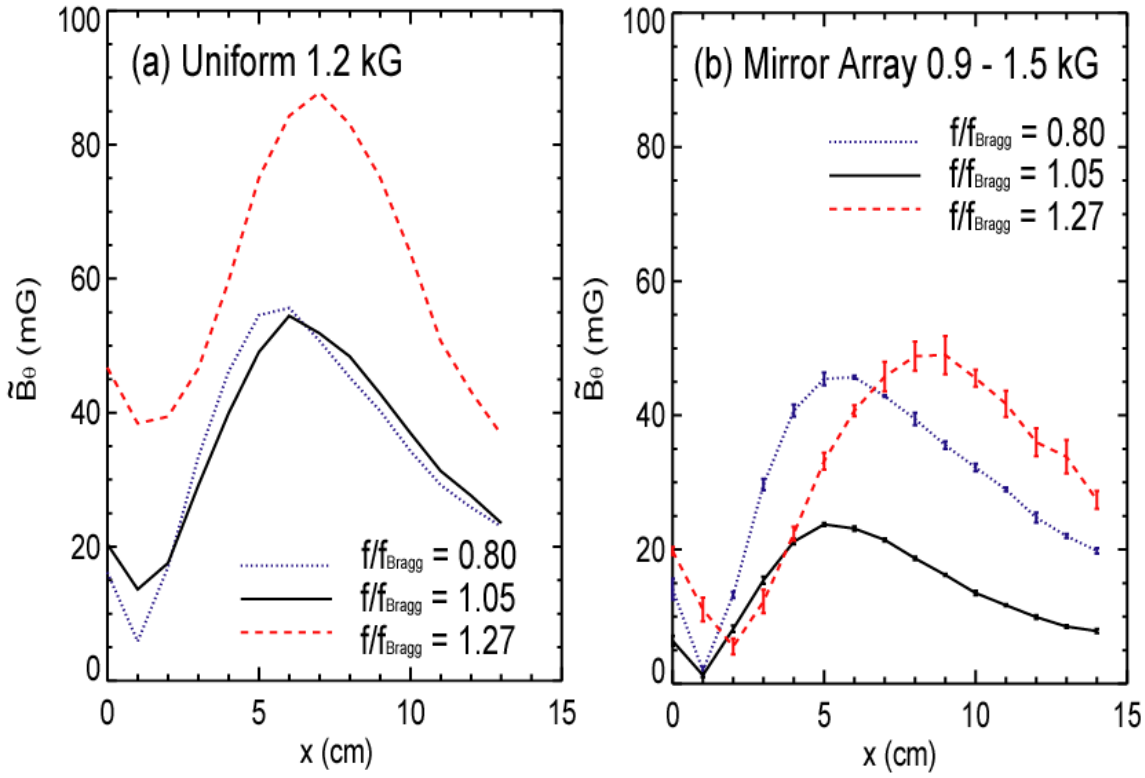

FIG. 4.4. $\tilde{B}_\theta$ radial profiles at Δz = 10.24 m (port 14).
(a) uniform magnetic field 1.2 kG, average n_e = 2.0 x 10^{12} cm^{-3}, f_{Bragg} = 124 kHz; (b) baseline mirror array configuration (M = 0.25), 0.9 – 1.5 kG, average n_e = 1.0 x 10^{12} cm^{-3}, f_{Bragg} = 160 kHz. (Field amplitude data acquired with 100 MHz sampling rate, averaging 8 samples. (b) shows random error bars calculated from 5 consecutive plasma shots.)

4.4 SAW Spectral Gap Experimental Results

4.4.1 Characteristics of Wave Spectra

In the following sections, the spectral intensity observed at various axial points and transverse to the magnetic field are plotted as a function of frequency. In a cylindrical system, U is defined as the wave magnetic energy density integrated over the azimuthal and radial coordinates,

$$U = \pi\mu_0 \left[\int_0^{r_{edge}} \tilde{B}_\theta(r)^2 r dr + b_{edge}^2 \ln(r)\Big|_{r_{edge}}^{r_{plasma}} \right], \tag{4.13}$$

where b_{edge} is the magnitude of wave magnetic field at Alfvén cone edge r_{edge} and r_{plasma} ~ 30 cm is the average radius of the plasma column. Since $U\Delta z$ yields the total wave magnetic energy of a thin disk at one axial location, U can be also referred to as the "disk energy density" [22].

In practice, a *B-dot* probe data scan at one axial position covers radially from 0 to 14 cm at a stepping of 1 cm. This range includes the peak of $\tilde{B}_\theta(r)$ and part of the *1/r* falling tail. b_{edge} can be reasonably replaced by the $\tilde{B}_\theta(r)$ value at r = 14 cm.

The ideal Bragg frequency is used to normalize the frequency. There are two error sources for estimating f_{Bragg}. First, the number of mirror cells is not infinite as the Bragg theory requires. Having as many mirror cells as possible is again important in this sense. Second, the value of the average Alfvén speed $\bar{v}_A$ has some uncertainty. Here, $\bar{v}_A$ is calculated two ways: 1) by using the average plasma density and magnetic field in the $\bar{v}_A$ formula and 2) by dividing the wave travel distance by the launch-detection delay time acquired from the cross-covariance analysis. The average of both methods is used

and they usually agree with each other to within 10%.

4.4.2 Dependence of SAW Spectra on the Number of Mirror Cells

The existence of the mirror-induced SAW spectral gap was first observed in the experimental results shown in FIG. 4.5, where the wave spectra for various mirror configurations are plotted: from zero (uniform field) to four mirror cells. The small disk antenna is placed at port 51, defining the $z = 0$ position. A *B-dot* probe is inserted in port 14 ($z = 11.80$ m) and radial scans are taken with SAW frequency swept from 50 kHz to 180 kHz at intervals of 5 kHz. The wave spectral intensity is the maximum field amplitude $\tilde{B}_\theta(r)$ of each radial wave field profile. The spectral gap becomes evident for the 4-mirror configuration where the wave field amplitude forms a trough near f_{Bragg} (~120 kHz). At higher frequencies above 150 kHz, the shaded area corresponds to large under-estimate of field amplitude since these earlier radial scans were taken up to $r = 10$ cm and the peak amplitude of high frequencies were left out. Nevertheless, this test shows that the spectral gap feature arises when there are a sufficient number of periods in the mirror array configuration.

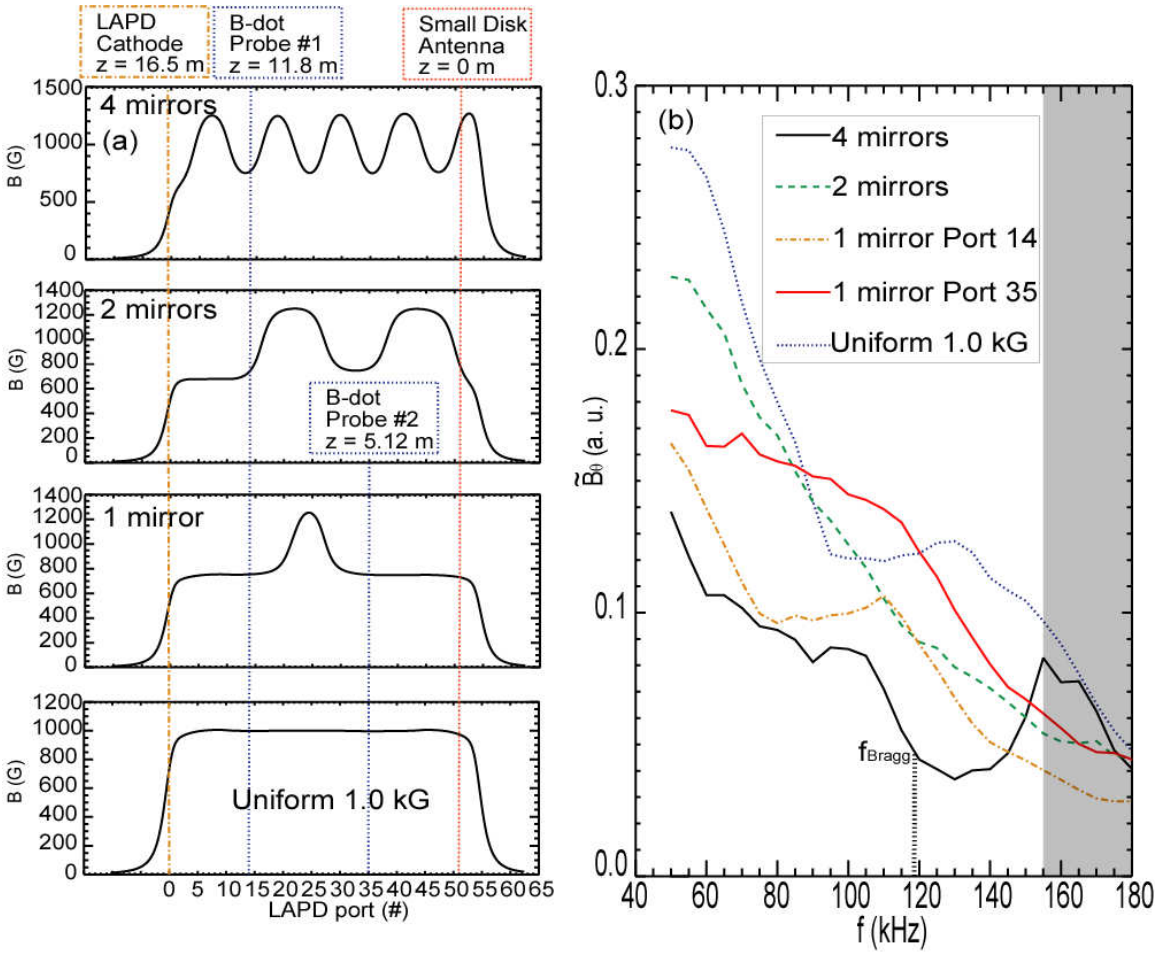

FIG. 4.5. SAW spectra with various numbers of mirror cells in LAPD.
(a) magnetic mirror configurations including the uniform case, where the axial magnetic field is plotted against LAPD port number. (Axial distance between two adjacent ports is 0.32 meter.) (b) $\tilde{B}_\theta$ versus SAW frequency, curves labeled according to the mirror array configuration. (Field amplitude data acquired with 100 MHz sampling rate, averaging 8 samples and 16 consecutive plasma shots. Maximum vertical error is less than 10% and horizontal ± 1 kHz).

4.4.3 Characteristics of Spectral Gap and Continua

With expanded radial scan range (up to r = 14 cm) and frequency scan range (75 kHz to 275 kHz), distinct spectral gap and two continua next to the gap can now be studied in detail. FIG. 4.6 shows the SAW field spectrum for the baseline mirror array configuration (M = 0.25). In FIG. 4.6 a) the radial-peak magnetic field and b) the "disk energy

density" are plotted versus the normalized frequency (f / f_{Bragg}). Both plots reveal the gap and two continua distinctly but the "disk energy density" spectrum has a better contrast between the peak and trough in addition to its better physical representation of the spectral intensity. Also in FIG. 4.6 a), the current in the antenna is frequency dependent but there are clearly no resonances. Here some spectral features are defined for future discussions: f_G and $f_{+(-)}$ are in turn the gap center frequency and the upper (lower) continuum frequency; the spectral intensity at f_G is defined as U_G and $U_{+(-)}$ at $f_{+(-)}$; the spectral Full-Width-at-Half-Maximum (FWHM) at $f_{+(-)}$ is defined as $\gamma_{+(-)}$; the spectral gap width Δf_G is the difference between f_+ and f_-.

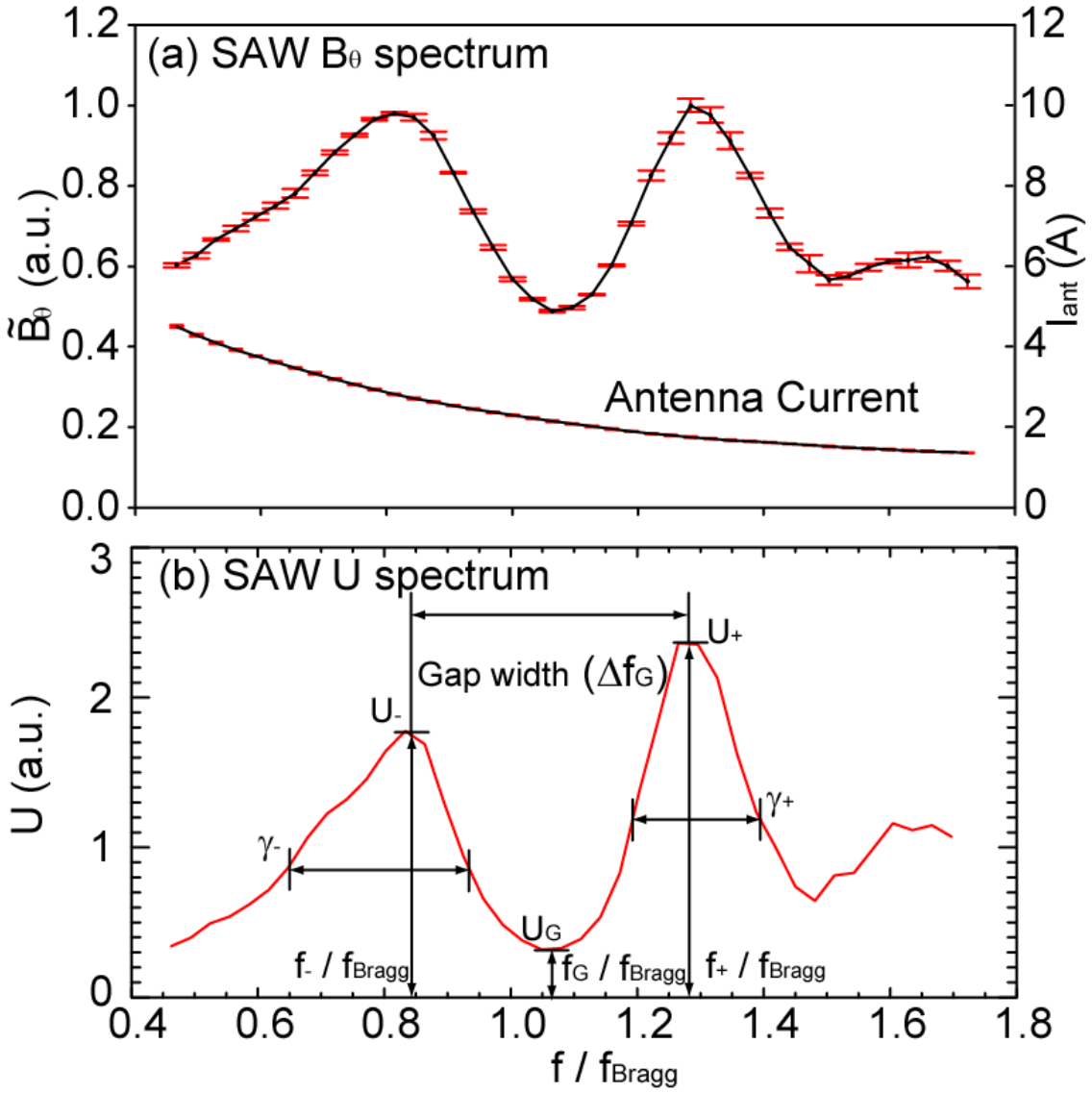

FIG. 4.6. Two different representations of the SAW spectrum at port 14 with the baseline mirror configuration (M = 0.25).

a) normalized $\tilde{B}_\theta$ versus f / f_{Bragg}; antenna current rms value is also over-plotted (error bars may be too small to be distinguished from the curve); b) "disk energy density" normalized using a constant ($1.0 \times 10^5 / \mu_0 \pi$) versus f / f_{Bragg}. f_{Bragg} = 160 kHz. (All data acquired with 100 MHz sampling rate, averaging 8 samples and 5 consecutive plasma shots. Maximum horizontal error is ± 0.01.)

4.4.4 Varying Mirror Depth (M)

In order to verify the dependence of SAW spectral gap width (Δf) on the mirror depth (M), four mirror array configurations are tested in the LAPD with different magnetic mirror depths (FIG. 4.7). The axially aligned blade SAW antenna extends from port 46 to port 49 for about 96 cm. The LAPD anode/cathode set is located 14 meters away to the south of port 46, which provides a strong reflective boundary condition[15, 16]. At the north end of the machine, a 2.6 meter long magnetic beach is presented for all configurations for a strong absorbing boundary condition. A *B-dot* probe is inserted in port 14 (z = 10.24 m) for radial scans. Notice that the background magnetic field configuration to the south of port 14 is kept constant for all mirror depths in order to preserve both a steady performance of the LAPD discharge and a steady plasma environment for the SAW diagnostics.

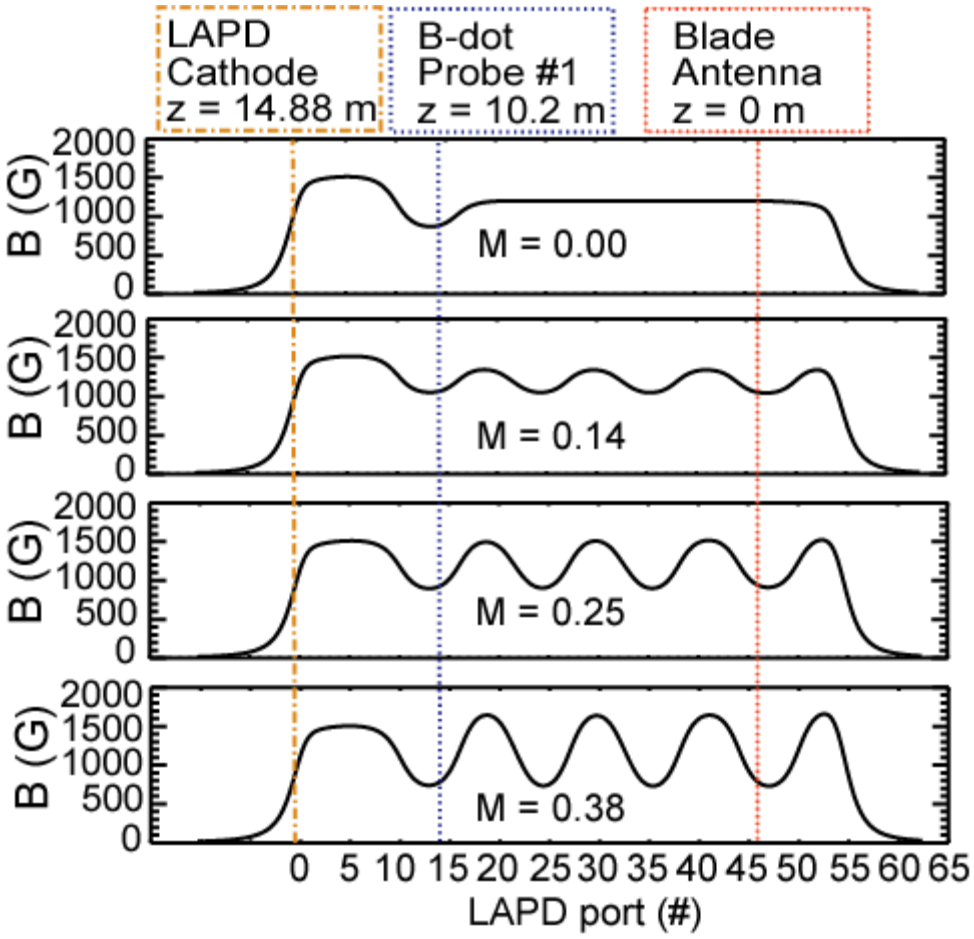

FIG. 4.7. Four magnetic mirror array configurations with gradually increased mirror depth
(*M* calculated with B field from port 20 to port 53; axial distance between two adjacent ports is 0.32 meter.)

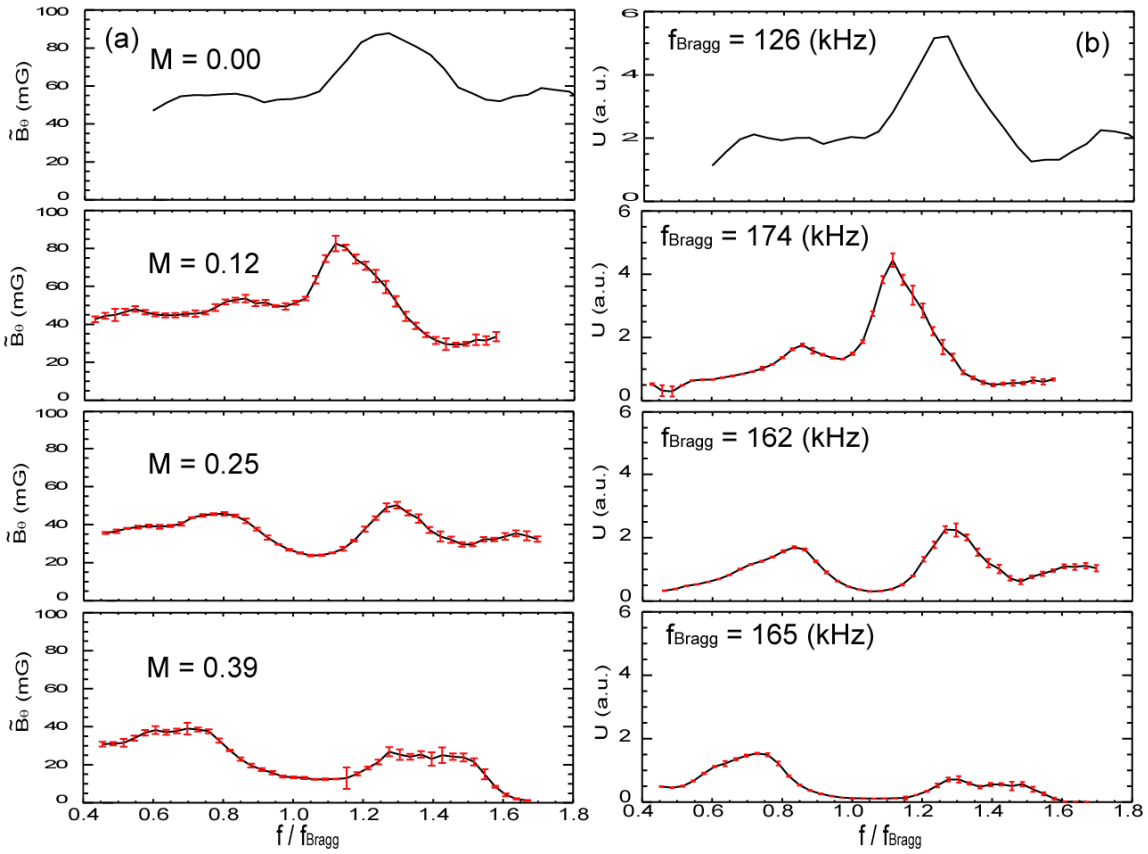

FIG. 4.8. SAW spectra for four magnetic mirror array configurations with different mirror depth (*M*) at port 14.
(a) maximum $\tilde{B}_{\theta}(r)$ versus f / f_{Bragg} and (b) "disk energy density" normalized using a constant (1.0 x $10^5/\mu_0\pi$) versus f / f_{Bragg}. Vertical error bars calculated from 5 consecutive plasma shots. Maximum horizontal error is ± 0.01.

The resulting spectra from all four mirror array settings are shown in FIG. 4.8 where the gap width gradually increases with the mirror depth. Although each mirror array configuration has different plasma density and thus different v_A, the mirror array spectra (normalized to f_{Bragg}) have a nearly identical gap center at f / f_{Bragg} ~ 1.05. With the uniform 1.2 kG magnetic field, there is only one spectral peak that splits into two branches once *M* is increased above zero.

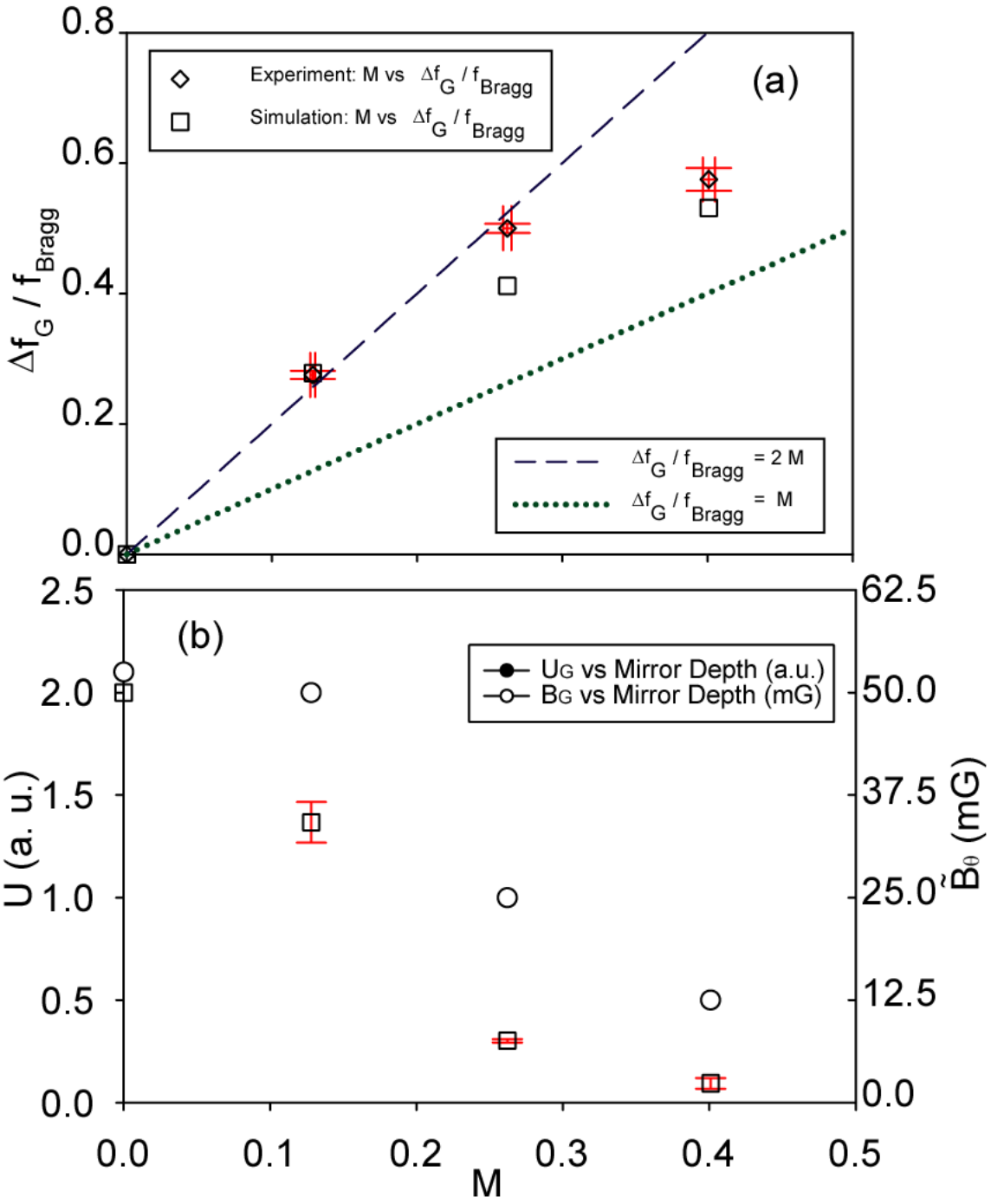

FIG. 4.9. Dependence of spectral gap width on mirror depth (*M*).
a) Experiment: diamond with error bars; Simulation: box; Green dotted line: theoretical prediction of Mathieu's equation (Eq. 4.9) for an infinite system; Blue dashed line: analytical prediction from TAE model (Ref. 23); (b) transmitted wave field amplitude B_G and disk energy density U versus mirror depth (M). (Vertical and horizontal error bars are random errors calculated from 5 consecutive plasma shots.)

The dependence of the normalized spectral gap width (Δf_G / f_G) on the magnetic mirror depth (M) is shown in FIG. 4.9 (a). In both experiment and simulation (see Sec. 4.5.3.), the spectral gap width increases with the mirror depth. The agreement between the experiment and the simulation is good for both small and large values of M. As M goes significantly above 0.1, the gap width deviates from the linear dependence predicted analytically in the small M limit (Eq. 4.9). The gap width is larger than the prediction in both experiment and simulation. Simulations with an infinite number of mirror cells (Sec. 4.5.2) agree well with Eq. 4.9, showing that this difference is caused by the finite number of mirror cells in the experiment. The transmitted wave field amplitude and disk energy density at f_G are shown in FIG. 4.9 (b). It is noticeable that the spectral intensity at the gap center decreases with higher M, which suggests that higher modulation strength in a periodic system cause higher reflectivity of the wave.

4.4.5 Verification: Interference Causes Spectral Gap

It is interesting to examine how the spectral features come into being over time. All previous data analysis is done with rf magnetic field response averaged over ~ 0.2 ms containing 15 full wave cycles for the lowest launching frequency (75 kHz). To have the best temporal resolution, the cross-covariance analysis averages over one wave period of each SAW frequency and progresses at a small time step (0.2 μs) forward from the onset of the antenna current signal. The temporal resolution is determined roughly by the order of the wave period so that the higher frequency has better resolution (up to 3.6 μs). The contour plot in FIG. 4.10 a) shows the wave field amplitude versus frequency and time in order to reveal the onset of mirror array-induced spectral features. The left curve shows

the time that it takes the wave front to propagate from the antenna to the *B-dot* probe the first time, calculated from dividing the axial distance (10.24 m) by the parallel group velocity in the cold-plasma (black solid) approximation. The curvature agrees with the contour plot in that the higher frequency SAW travels with slower group velocity in the parallel direction. It is important to notice that, before the wave is reflected back from the anode/cathode, the gap and continua features are already formed, which shows that the mirror cells alone can cause strong modification of the spectrum. The features then grow to the fullest contrast upon reaching the curve to the right, which is the time that it takes the wave to reflect from the anode/cathode and back to port 14, again calculated from the dispersion relation. From FIG. 4.10 b), where the wave field amplitudes are plotted against time for three characteristic frequencies (f_G, f_+ and f_-), it is obvious that the wave amplitude at the gap frequency f_G peaks when the first forward wave front reflects back (~ 16 μs) and then is further suppressed by the destructive interference between the forward and reflected waves. All the features turn into steady state as seen in the previous sections after the initial 40 μs.

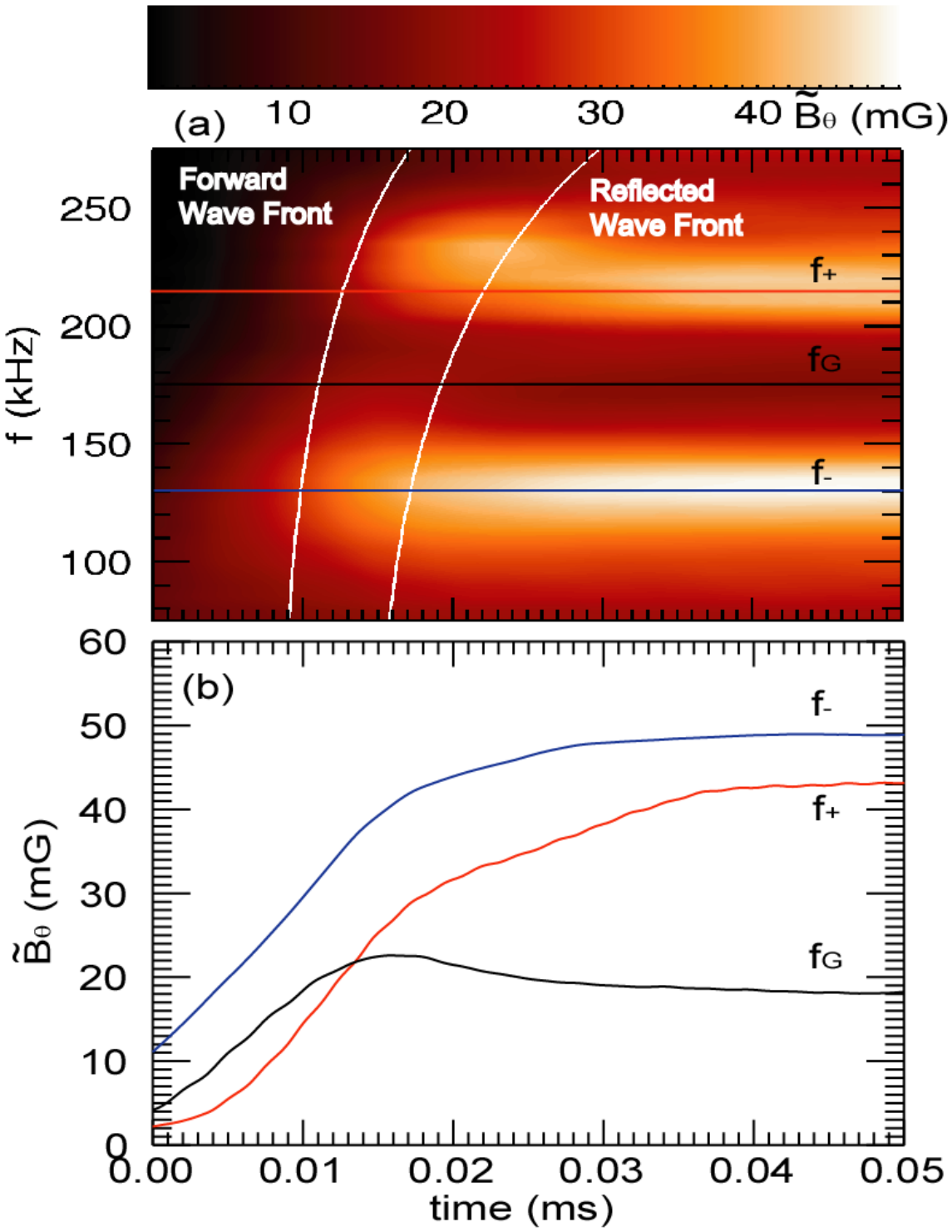

FIG. 4.10. Time history of the running cross-covariance between the wave field and the antenna current with the baseline mirror array configuration (M = 0.25) at port 14.
a) contour plot of wave field intensity versus frequency and time. The first white curve indicates the time that takes the wave to travel towards the probe one-way; the second white curve indicates the time that takes the wave to return to the

probe after being reflected at the anode/cathode the first time. b) Temporal plot of wave field intensity growth at three characteristic frequencies: f_+ (215 kHz), f_- (130 kHz) and f_G (175 kHz).

4.4.6 Continuum Quality Factor Varying with Density

The quality factors of the continuum depend on the damping mechanisms of SAW propagation, the refraction and reflection at each mirror cell as well as the machine end condition. Here theoretical damping estimation in a straight field LAPD plasma column is used as the only contribution to the theoretical quality factor. In Ref. [17], SAW damping along the ray path through the background field gradient were determined to be mainly from three mechanisms: the ion-cyclotron damping, the electron Landau damping and the electron-ion Coulomb collisions. In the baseline mirror array configuration (M = 0.25), the upper continuum f_+ is lower than 0.6 f_{ci} at $B_{0\min}$, which means that the ion-cyclotron damping is negligible. For a general resonant mode ω, the theoretical quality factor can be expressed as:

$$Q = \frac{\omega}{\gamma} = \frac{m_i \omega}{m_e(\nu_{ei} + \nu_{e-Landau})}\left(\frac{k_{//}}{k_\perp}\right)^2\left(\frac{\omega_{ci}}{\omega}\right)^2, \qquad (4.14)$$

where ν_{ei} is the electron-ion Coulomb collision rate and $\nu_{e-Landau} \propto \omega$ is the effective collision frequency for electron Landau damping rate (see Eq. 4.20). Several spectra are taken with various n_e in the LAPD as shown in FIG. 4.11, where the horizontal axis is the normalized frequency f / f_{Bragg} centered to the upper continuum of each curve. When the density drops from 2.66 x 10^{18} m^{-3} to 1.26 x 10^{18} m^{-3}, the normalized spectral width drops as predicted by Eq. 4.14 as shown in the inset. It is also noticeable that the spectral intensity at the gap center increases with the higher density, which implies that if there

are any modes within the gap region, they are not subject to the continuum damping. More quantitative discussions of mode damping mechanisms will be included in the simulation works of Sec. 4.5.

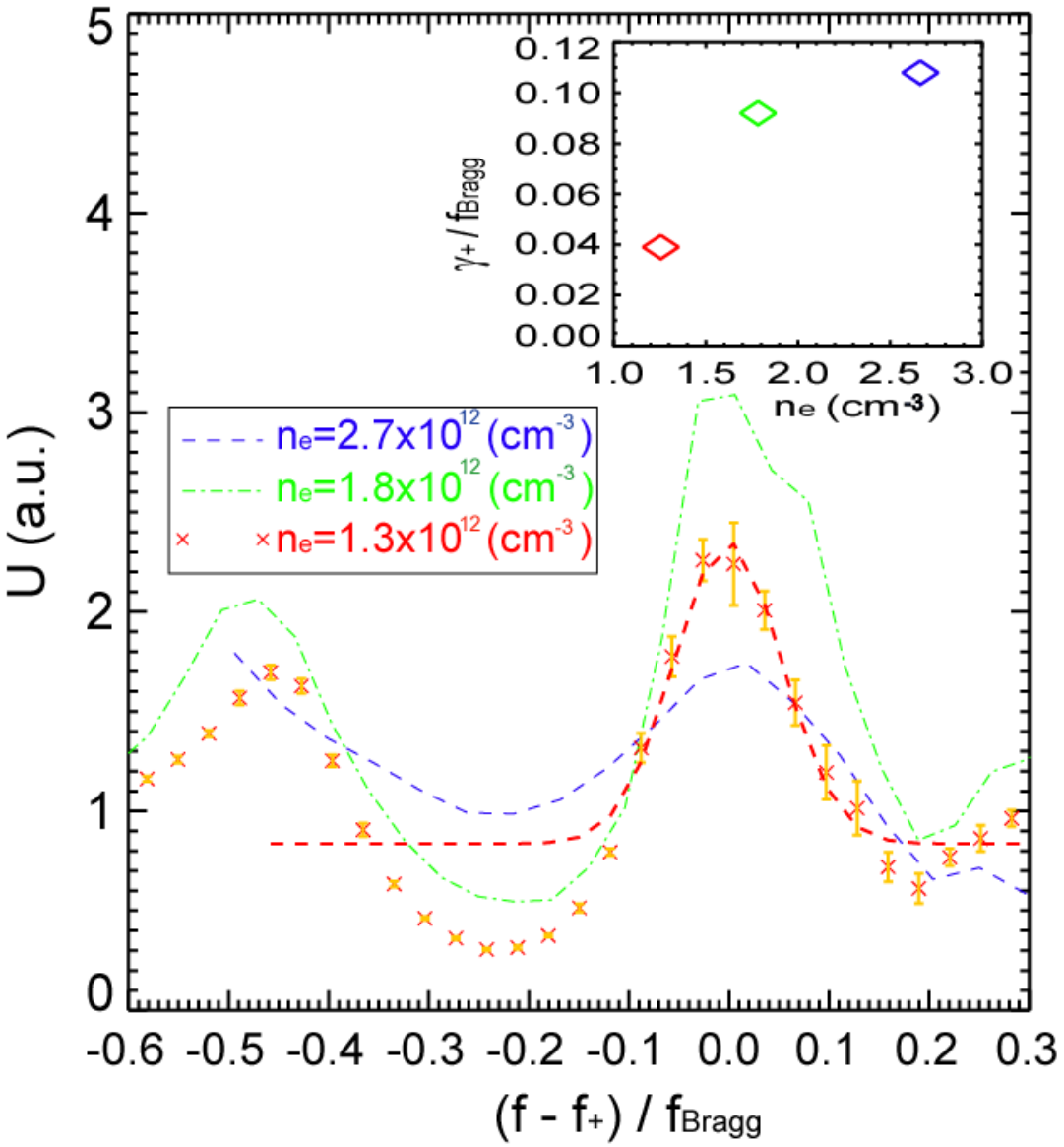

FIG. 4.11. Upper continuum spectra width (γ_+ / f_+) with three different plasma densities.
The upper continuum of each spectrum is centered at the horizontal origin. The inset shows the normalized spectra width versus plasma density. The error bars as well as the Gaussian fit of the f_+ peak are shown for n_e = 1.26 x 10^{18} m^{-3} case. (All data acquired with 100 MHz sampling rate, averaging 8 samples and 5 consecutive plasma shots. Maximum horizontal error is ± 0.01.)

4.5 SAW Spectral Gap Simulation

A linear electro-magnetic wave solver for cold magnetized plasma (Guangye Chen, Univ. Texas, Austin) is employed to treat a magnetic mirror array configuration. The details of the solver are described in Ref. [24], in which the solver was used to study helicon modes.

4.5.1 Electro-Magnetic Wave Solver

The wave field is governed by Maxwell's equations in the frequency domain

$$\begin{cases} \nabla \times \mathbf{E} = i\omega \mathbf{B}, \\ \dfrac{1}{\mu_0} \nabla \times \mathbf{B} = -i\omega \mathbf{D} + \mathbf{j}_a, \end{cases} \tag{4.15}$$

where **E** and **B** are the electric and magnetic fields, μ_0 is the permeability of free space, **D** is the electric displacement vector, ω is the antenna frequency, and $\mathbf{j}_a$ is the antenna current density. The cold plasma approximation yields the following relation between the electric displacement vector and the electric field[25, 37], $D_{\alpha\beta} = \varepsilon_{\alpha\beta} E_{\alpha\beta}$, or equivalently

$$\mathbf{D} = \varepsilon_0 (\varepsilon \mathbf{E} + ig[\mathbf{E} \times \mathbf{b}] + (\eta - \varepsilon)(\mathbf{E} \cdot \mathbf{b})\mathbf{b}) \tag{4.16}$$

where $\mathbf{b} \equiv \mathbf{B}_0 / B_0$ is the unit vector along the external magnetic field and

$$\begin{cases} \varepsilon &= 1 - \sum\limits_\alpha \dfrac{\omega + i\nu_\alpha}{\omega} \dfrac{\omega_{p\alpha}^2}{(\omega + i\nu_\alpha)^2 - \omega_{c\alpha}^2}, \\ g &= -\sum\limits_\alpha \dfrac{\omega_{c\alpha}}{\omega} \dfrac{\omega_{p\alpha}^2}{(\omega + i\nu_\alpha)^2 - \omega_{c\alpha}^2}, \\ \eta &= 1 - \sum\limits_\alpha \dfrac{\omega_{p\alpha}^2}{\omega(\omega + i\nu_\alpha)}. \end{cases} \tag{4.17}$$

Here the subscript α labels particle species (electrons and ions), $\omega_{p\alpha}$ is the plasma frequency, $\omega_{c\alpha}$ is the gyro-frequency, and ν_α is the collision frequency. Singly-ionized

helium ions are assumed. Equation (4.15) is solved for a given azimuthal mode number *m* on a 2D domain (*r, z*).

The external magnetic field $\mathbf{B}_0$ is axisymmetric, with $B_{0r} << B_{0z}$ and $B_{0\theta} = 0$. It is therefore appropriate to use a near axis expansion for the magnetic field, which means that B_{0z} is treated as a function of *z* only and

$$B_{0r}(r, z) = -\frac{1}{2} r \frac{\partial B_{0z}(z)}{\partial z}. \tag{4.18}$$

The antenna is a blade antenna shown in FIG. 4.2. The components of antenna current density for the $m = 0$ mode are given by

$$\begin{aligned} j_{ar} &= \frac{I_0}{2\pi r} H(r)[\delta(z - z_a) - \delta(z - z_a - L_a)], \\ j_{a\theta} &= 0, \\ j_{az} &= \frac{I_0}{2\pi r} H(z - z_a) H(z_a + L_a - z)\delta(r - R_a), \end{aligned} \tag{4.19}$$

where I_0 is the amplitude of the current, L_a is the antenna length, z_a is the antenna position as shown in FIG. 4.2, R_a is the radius of the horizontal rod, and *H* is the Heaviside step function.

4.5.2 Periodic Array of Mirrors

It is convenient to first consider a single mirror cell ($0 \le z \le L_m$) with periodic boundary conditions, which provides an ideal case to study the Bragg reflection induced spectral gap as well as a benchmark for the realistic simulations of finite number of mirrors. This single mirror cell has the same sinusoidal profile of the magnetic field described in Eq. (4.1). The following boundary conditions are used:

1. The chamber wall at *r* = 0.5 m is assumed to be a conducting boundary where the tangential components of the electric field vanish;

2. Since all the field components are regular at $r \to 0$, there are: $B_\theta\big|_{r=0} = 0$ and $(rE_\theta)\big|_{r=0} = 0$ for $m = 0$; $E_z\big|_{r=0} = 0$ and $(rE_\theta)\big|_{r=0} = 0$ for $m \neq 0$;

3. Periodic boundary condition: $(\mathbf{E},\mathbf{B})\big|_{z=L_m} = (\mathbf{E},\mathbf{B})\big|_{z=0} e^{i\phi_s}$, where φ_s is the given phase difference between the field components at $z = 0$ and $z = L_m$.

The experimentally measured radial profile of the plasma density is used in the code as shown in FIG. 4.3. The density is assumed to be independent of *z*. The collision frequency for electrons is calculated as the electron-ion Coulomb collision frequency[26] $\nu_{ei} = 2.91\times10^{-12} n_e T_e^{-3/2} \ln\Lambda$, where T_e and n_e are expressed in eV and m^{-3}, respectively. The electron temperature is taken to be 8 eV; the Coulomb logarithm is taken to be $\ln\Lambda = 12$. The collision frequency for ions is set to zero.

In this simulation, $L_a = 0.8$ m, $z_a = 1$ m, and $R_a = 0.15$ m. Although the antenna launches several azimuthal modes, the amplitudes of all modes with $m \neq 0$ are significantly smaller than that of the *m* = 0 mode. Therefore, only *m* = 0 mode is considered here.

The amplitude of B_θ is recorded at (*r* = 0.04 m , *z* = 3 m) and normalized by the antenna current I_0 with different values of the phase angle $\varphi_s \in (0,2\pi)$ (FIG. 4.12. a). In a uniform system, the phase angle φ_s determines the value of $k_z = \varphi_s / L_z$. In the mirror configuration, the forbidden band appears around $k_m = \pi / L_z$. There are two peaks in B_θ for each value of φ_s. For various $\varphi_s \in (0,\pi)$, the lower-frequency peak represents a right-traveling wave, and the one at the higher frequency is a left-traveling wave.

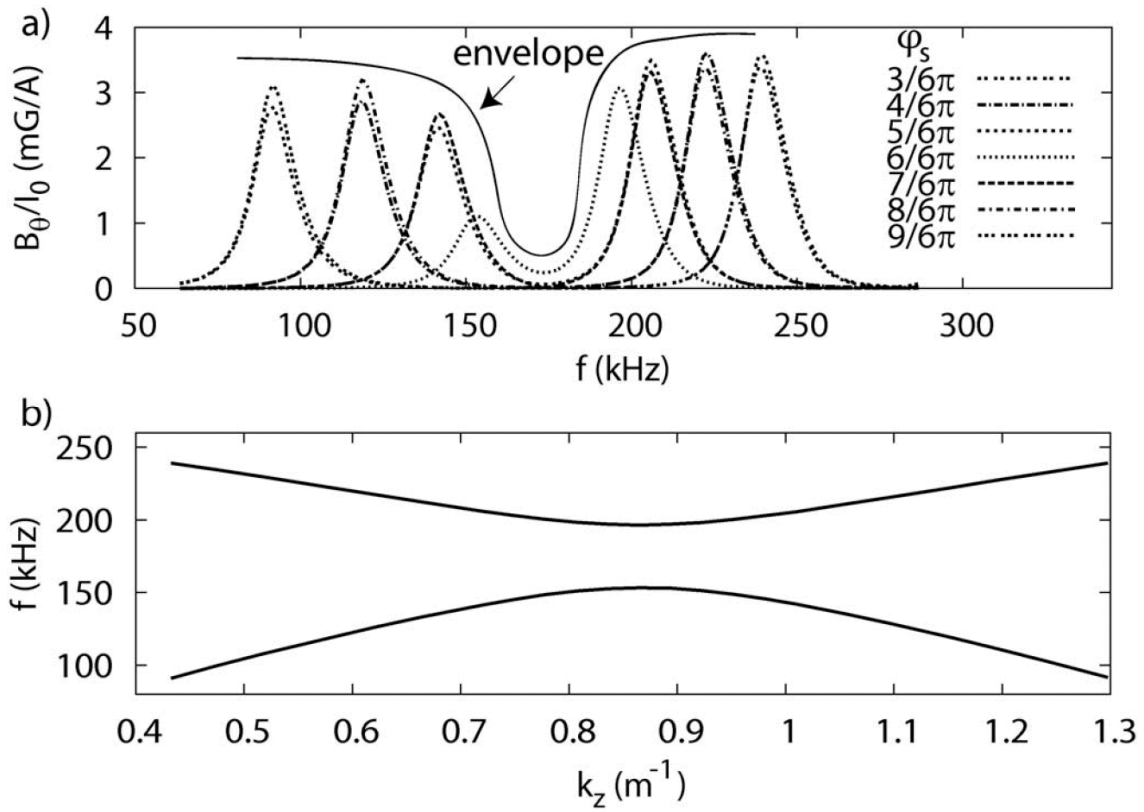

FIG. 4.12. a): simulation of wave excitation as a function of φ_s and frequency. A sharp forbidden gap of wave excitation is evident between two branches of traveling waves. Here the wave amplitude is normalized by the antenna current. b): the dispersion relation of excited waves from the simulation, in which *f* corresponds to the maximum of each peak and $k_z \equiv \varphi_s / L_z$.

At larger values of φ_s ($\varphi_s \in (\pi, 2\pi)$), the waves in both branches change the direction of propagation, switching from the right to the left in the lower branch, and from the left to the right in the upper branch. At the transition (where $\varphi_s \approx \pi$) the wave becomes a standing wave, almost fully reflected by the mirrors due to the Bragg reflection. It is clear that a gap is formed where the wave excitation is significantly suppressed as illustrated with an envelope (solid line) in FIG. 4.12 (a). The dispersion curves found in the simulation (FIG. 4.12 b) evidently reproduced FIG. 4.1. More importantly, because of the definite k_z in the simulation, the gap width can be determined accurately at $k_z = k_m$, which matches the prediction of Eq. (4.9).

4.5.3 Simulation of Mirror Array in the LAPD

Now the mirror array configuration in the LAPD is considered realistically as shown in FIG. 4.13, with a magnetic beach as an absorbing end and the anode as a reflecting end. The magnetic beach here is longer (7.74 m) than that in the experiment to ensure complete absorption of the waves. A finite ion collision frequency ν_i is introduced to resolve the ion cyclotron resonance in the beach area. The boundary conditions in the radial direction remain the same as in the case of infinite periodic system.

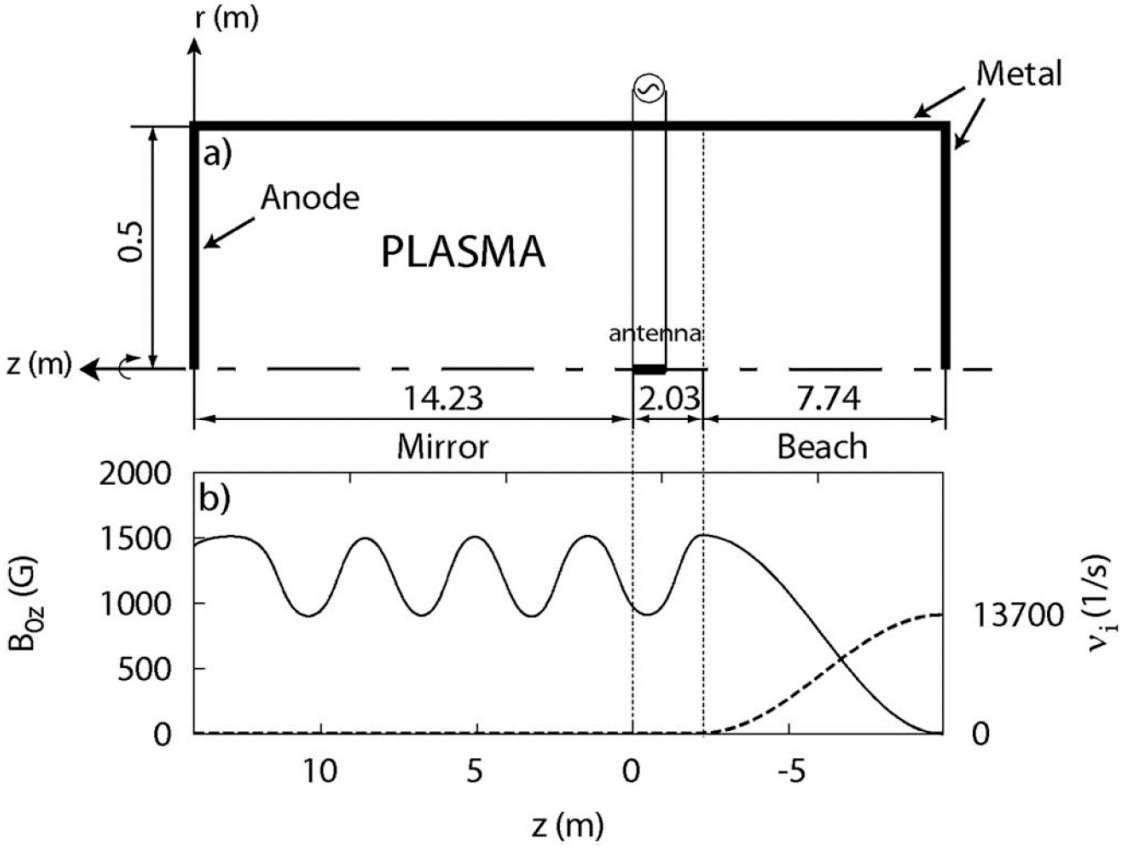

FIG. 4.13. Computational setup used to simulate the mirror array in the LAPD shown in FIG. 4.2.
a): the computational domain. b): the *z* component of the external magnetic field (left) and the finite ion collision frequency in the beach area (right).

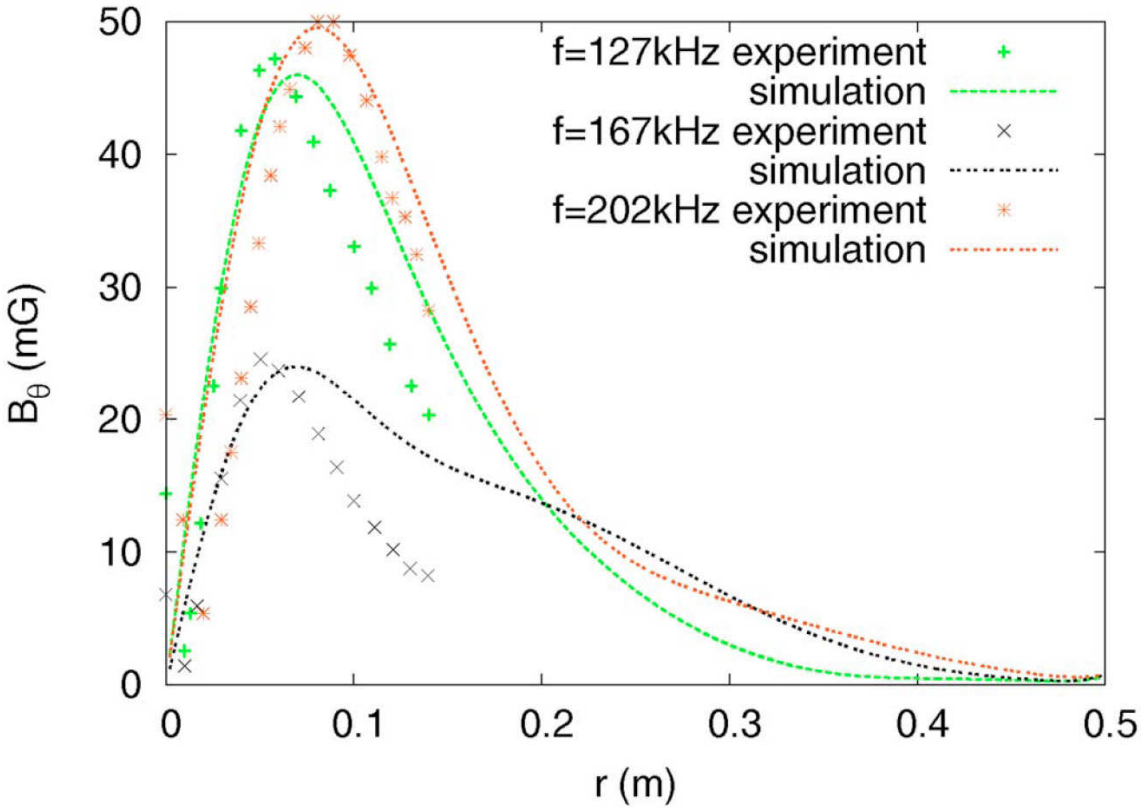

FIG. 4.14. The radial profiles of azimuthal B field (rms) at three frequencies comparing simulation and experimental results.
This simulation uses $\alpha = 4$ which is defined in Eq. (4.20).

To be consistent with the experiment, the *z* coordinates is pointing from right to left; the origin is set at the left leg of the blade antenna with $L_a = 1.0$ m, and $R_a = 0.005$ m. The variable antenna current due to rf coupling efficiency at different frequencies (FIG. 4.6) is used to calculate the wave field amplitude. The radial profile of B_θ for three frequencies f = 127 kHz, 167 kHz and 202 kHz is shown in FIG. 4.14, compared with the experimental measurement at *z* = 10.25 m (port 14). The calculated quantity B_θ in the plot is $|B_\theta(f,r,z)|/\sqrt{2}$, which is equivalent to the rms average of B_θ from the measurement. The frequency scan of the radial maximum value of B_θ at *z* = 3.21 m (port 36) and *z* = 10.25 m (port 14) are compared with the experimental data in FIG. 4.15.

Both in the simulation and the experiment, the wave signal at port 14 exhibits a gap at the same frequency as in the periodic system, while at port 36, the gap is less obvious because the detector is only one mirror away from the antenna.

Additional damping mechanism beside electron-ion Coulomb collisions is needed to match the absolute value of wave amplitude. Since the electron thermal velocity is comparable to the wave phase velocity in this study, electron Landau damping can play an important role in the wave propagation. To take into account of the effect of Landau damping, an effective electron collision frequency is introduced as

$$\nu_{e-Landau} = \alpha \frac{\mathrm{v}_{te}\omega}{\mathrm{v}_A}, \tag{4.20}$$

where α is a numerical factor. As a result of the frequency dependence of $\nu_{e-Landau}$, the wave amplitude is more suppressed in the higher frequency region, which makes the shape of the scan close to that in the experiment. A good agreement of the position, depth and width of the gap at port 14 is reached in the calculation with α = 4. The agreement at port 14 is better than that at port 36, which may be due to near-field effects at port 36.

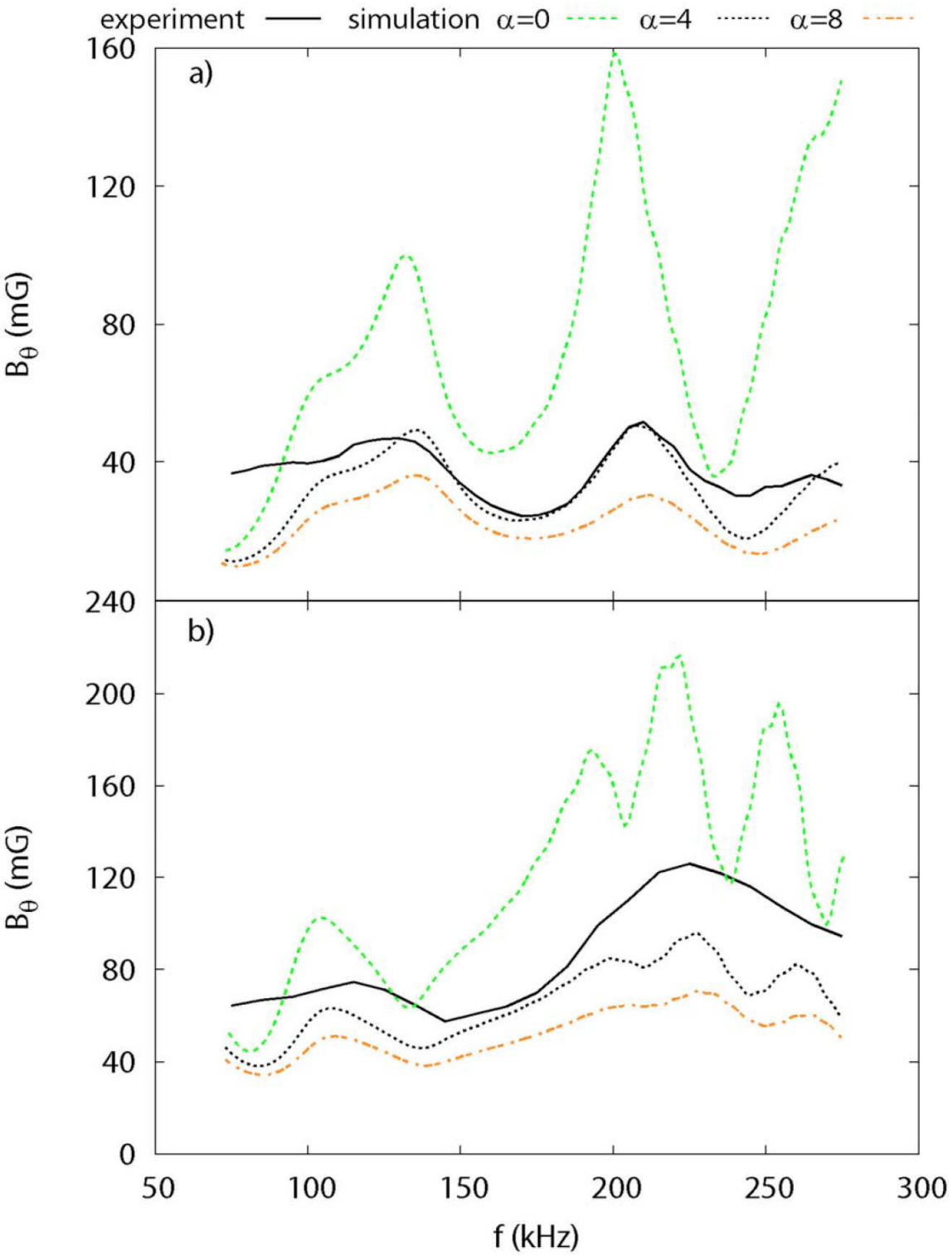

FIG. 4.15. Comparison of B_θ : experiment versus the simulation.

a): port 14 and b): port 36. The plots show the radial maximum of B_θ as a function of frequency. Three α values represent possible estimates of effective collision frequencies for Landau damping.

With the antenna placed in the last mirror, the waves are launched in both directions. It is instructive to characterize wave propagation by the wave energy density[27]

$$W = \frac{E_\alpha^* E_\beta}{4} \frac{\partial(\omega^2 \varepsilon'_{\alpha\beta})}{\omega \partial \omega}, \tag{4.21}$$

where $\varepsilon'_{\alpha\beta}$ is the Hermitian part of the dielectric tensor neglecting the collision frequency. FIG. 4.16 shows the 2-D contour plots of the wave energy density for a frequency below the forbidden gap at f = 120 kHz, a frequency inside the gap at f = 170 kHz, and a frequency above the gap at f = 220 kHz. It is seen that the wave energy is the highest at the antenna. For the frequencies away from the forbidden gap, i.e. f = 120 kHz and 220 kHz, the wave propagates leftwards and reflects as it reaches the boundary, the anode in the experiment. The magnitude of the wave energy decreases along the propagation due to damping and absorption. The patterns of wave energy density are similar at these two frequencies. In the forbidden gap region, e.g. f = 170 kHz, the wave amplitude decreases faster due to the multiple reflections from the mirror cells. As a result, the wave energy diminishes as it reaches the anode. On the other hand, for all the cases, the waves propagate rightwards without much reflection until absorbed at the magnetic beach.

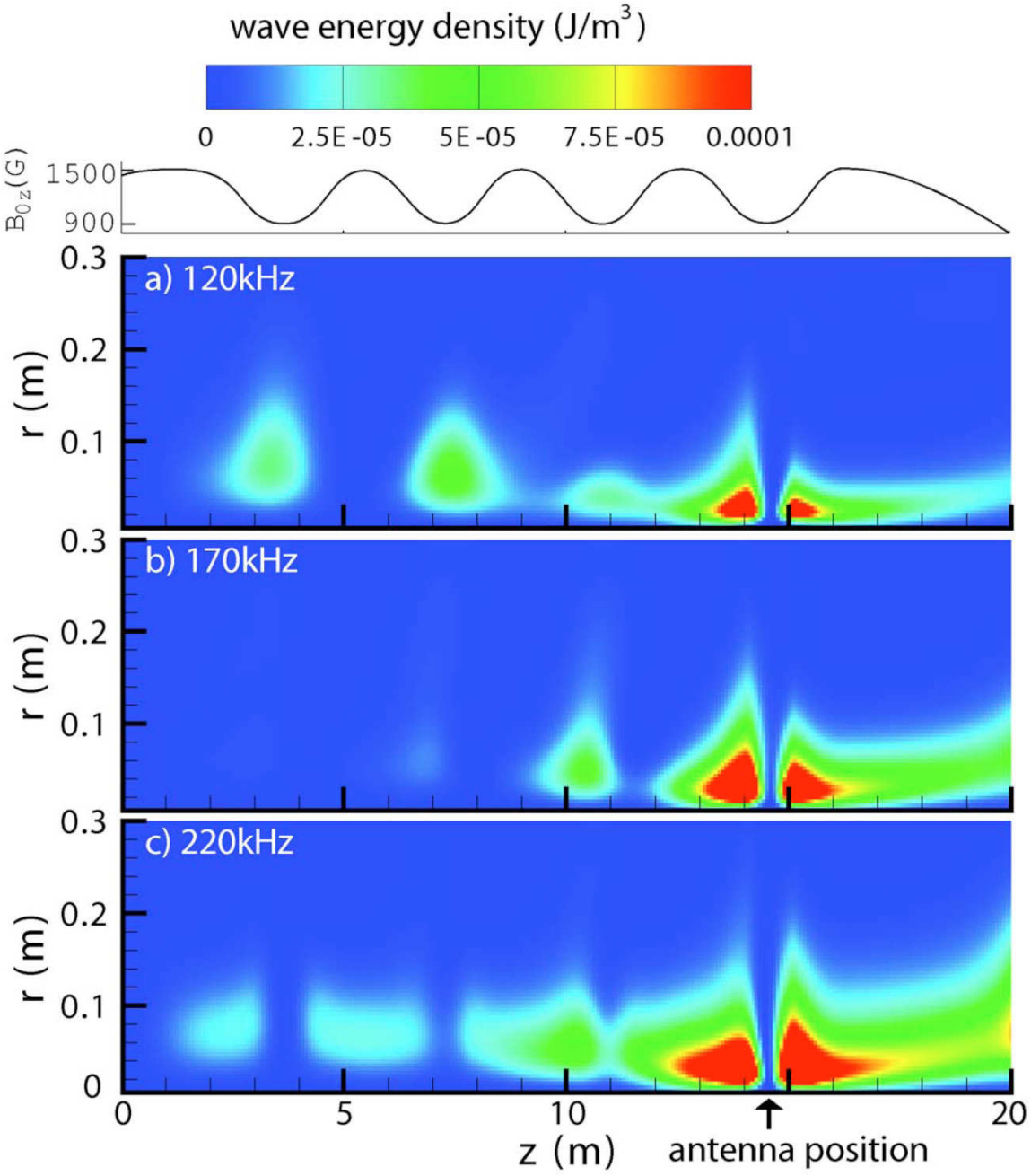

FIG. 4.16. The contour plots of wave energy density obtained from Eq. (4.21) for three frequencies.
a): f = 120 kHz below the gap; b): *f* = 170 kHz in the gap; c): *f* = 220 kHz above the gap.

[1] Lord Rayleigh, Phil. Msg., vol. 24, pp.145-159; August, (1887).

[2] Charles Kittel, *Introduction to Solid State Physics*, 7th Edition, (John Wiley & Sons Inc., 1996).

[3] H. Kogelnik and C. V. Shank, Appl. Phys. Lett. **18** (4), 152 (1971).

[4] H. Kogelnik and C. V. Shank, J. Appl. Phys. **43** (5), 2327 (1972).

[5] C. K. Chong, D. B. McDermott, M. M. Razeghi, N. C. Luhmann, Jr., J. Pretterebner, D. Wagner, M. Thumm, M. Caplan, and B. Kulke, IEEE Trans. Plasma Sci., 20 (3), 393 (1992).

[6] J. J. Barroso, J. P. L. Neto, and K. G. Kostov, IEEE Trans. Plasma Sci., **31** (4), 752 (2003).

[7] E. Yablonovitch, T. J. Gmitter, R. D. Meade, A. M. Rappe, K. D. Brommer, J. D. Joannopoulos, Phys. Rev. Lett. **67** (24), 3380 (1991).

[8] Mehmet Bayindir, B. Temelkuran, and E. Ozbay, Phys. Rev. Lett. **84** (10), 2140 - 2143 (2000).

[9] K. F. Casey and J. R. Matthes, J. Math. Phys. **10** (5), 891 (1969).

[10] C. Uberoi, Phys. Fluids **15,** 1673 (1972).

[11] D. A. D'Ippolito and J. P. Goedbloed, Plasma Phys. **22,** 1091 (1980).

[12] R. L. Dewar *et al.,* Phys. Fluids **17,** 930 (1974).

[13] R. Betti and J. P. Freidberg, Phys. Fluids B **4,** 1465 (1992).

[14] M. S. Chu *et al.,* Phys. Fluids B **4,** 3713 (1992); Y. I. Kolesnichenko, V. V. Lutsenko, H. Wobig, Y. V. Yakovenko, O. P. Fesenyuk, Phys. Plasmas **8,** 491 (2001).

[15] C. Mitchell, S. Vincena, J. Maggs and W. Gekelman, Geophys. Res. Lett., **28** (5), 923 (2001).

[16] C. C. Mitchell, J. E. Maggs, and W. Gekelman, Phys. Plasmas **9** (7), 2909 (2002).

[17] S. Vincena,a) W. Gekelman, and J. Maggs, Phys. Plasmas **8** (9), 3884 (2001).

[18] C. C. Mitchell, J. E. Maggs, S. T. Vincena, and W. N. Gekelman, J. Geophys. Res. **107** (A12), 1469 (2002).

[19] M. Abramovitz and I. A. Stegun, *Handbook of Mathematical Functions*, (Dover Publications, Inc., New York, 1972), p 722 (20).

[20] H. Boehmer, M. Zales Caponi and J. Munch, in *Free Electron Lasers*, Proceedings of the 7th Course

on Physics and Technology of Free Electron Lasers of the International School of Quantum Electronics, Erice, 1980, edited by S. Martellucci and Arthur N. Chester .

[21] S. Vincena, Ph. D. thesis, Univ. Cal. Los. Angeles, (1999).

[22] S. Vincena, W. Gekelman, and J. Maggs, Phys. Rev. Lett. **93** (10), 105003-1(2004).

[23] G. Y. Fu and J. W. Van Dam, Phys. Fluids B **1** (10), 1949 (1994).

[24] G. Chen, A.V. Arefiev, R.D. Bengtson, B.N. Breizman, C.A. Lee, L.L. Raja, Phys. Plasmas **13**, 123507 (2006).

[25] T. H. Stix, *Waves in Plasmas*, (American Institute of Physics, New York, 1992), p. 38.

[26] P. Helander and D. J. Sigmar, *Collisional Transport in Magnetized Plasmas*, (Cambridge University Press, Cambridge, UK, 2002), p. 5.

[27] V.D. Shafranov, *Reviews of Plasma Physics 3*, (Consultants Bureau, New York, 1967), p. 143.

Chapter 5

CONCLUSIONS

5.1 Summary

Two basic plasma experiments are accomplished during this thesis work.

In preparing the hardware for the first experiment, lithium ion sources using lithium – aluminosilicate as a thermionic emitter were developed and characterized. Two commercially available emitter sizes (0.6" and 0.25") with integrated heater assembly were used. A compact ion gun structure was chosen featuring grids for acceleration – deceleration sections. In principle, the ion guns can be operated at any angle with respect to the magnetic field. At high plasma density environment, e. g. the discharge plasma of the LAPD, a minimum pitch angle must be used to avoid plasma electron loading of the emitter circuit. Typical ion beam densities are in the 1 mA/cm^2 range at beam voltages between 400 V and 2000 V. The ion guns successfully operated in the discharge of the LAPD. Collimated/gridded fast-ion analyzers are developed to detect the fast-ion signals in the LAPD discharge with good signal-to-noise and spatial resolution.

In the first experiment, Doppler shifted cyclotron resonance effect is directly measured from the beam spatial non-classical spreading caused by single and multi-mode shear Alfvén waves. Both qualitative and quantitative agreements of the SAW-induced

spatial displacements with theory are achieved. Primary and subordinate resonance peaks in frequency are seen in experiment and simulation. A subordinate resonance is caused by partial overlapping of the fast ion and wave phases when the frequency is an integer fraction of the primary frequency. With a pure sine wave drive, a null effect point is discovered in the resonance spectrum as predicted by theory. This null effect is absent with a triangle wave drive because higher harmonics cause an extra resonance effect. Resonance effect is kept within linear regime where spatial displacements are proportional to SAW amplitude. Both single-particle and Monte-Carlo simulation codes proved robust for predicting fast-ion resonance experiment. Finally, SAW-induced energy change of fast ions was verified by variable potential barriers in the fast-ion analyzer.

In the second experiment, the axial magnetic periodicity induced Alfvén spectral gaps and continua are discovered and characterized experimentally for the first time. The gap spectral width is found to increase with the Magnetic mirror depth (M), which is predicted by solving Mathieu's equation as well as the coupled wave theory in TAE studies[1, 2]. The running cross-covariance analysis shows that reflected wave from the LAPD anode/cathode enhances the features of the spectral gap. The quality factor of the spectral upper continuum is found to decrease with the plasma density.

A finite-difference simulation code successfully models this experiment in a 2-D r-z plane. The results from an ideal case with periodic boundary conditions, i.e. infinite number of mirrors, show wave energy reflection near the frequency satisfying the Bragg condition. In a realistic simulation using experimental conditions at the LAPD machine, two candidate damping mechanisms, the electron-ion Coulomb collision and the electron Landau damping, are both essential in order to match the calculated spectra to the

experimental ones.

5.2 Implications

To emphasize the correlation of the second work with the TAE studies, the similarities between the two are summarized in Table 4, where in both cases a frequency gap arises due to a periodic modulation of the ambient magnetic field. Due to the toroidal coupling in a tokamak and the magnetic shear, a certain discrete frequency can exist inside the gap, i.e. TAE modes.

Properties \ Experiments	TAE	SAW in Mirror Array
Periodicity	Magnetic field: $B_0(\theta)$	Magnetic field: $B_0(z)$
Periodic length	$2\pi qR$	Mirror length: L_m
B_0 modulation strength	$\hat{\varepsilon}$ [Ref. 2]	$M = \frac{B_{\max}-B_{\min}}{B_{\max}+B_{\min}}$
Wave function	$\sim exp(im\theta)$	$\sim exp(ik_{//}z)$
Bragg Condition	$k_{//}=n/2qR$	$k_n=n\pi/L_m$
Spectral Gap/ Continuum	Yes	Yes
Eigenmodes	Yes	?

Table 4 Similarities between TAE and mirror array Alfvén experiment.

In a toroidal geometry, at rational q (safety factor) magnetic surfaces, where $q = (|m|+1/2)/|n|$, two different poloidal modes m and m+1 couple to each other since their wave vector satisfy $k_{//m} = -k_{//m+1}\frac{1}{R_0}\left(n+\frac{m}{q}\right)$. Solving the two coupled eigenmode equations for poloidal electric fields[2], the frequency difference between two

continuum frequency branches is defined as the spectral gap width: $\Delta\omega = \omega_+ - \omega_- \approx 2\hat{\varepsilon}\left|\mathrm{v}_A k_{//m}\right|$. From the analogy in Table 4, with proper substitution of relevant quantities, the expressions for the spectral gap width in the magnetic mirror array experiment is $\Delta f_G = f_+ - f_- \approx 2Mf_{Bragg}$. This is shown as the blue dash line in FIG. 4.9. This work in the LAPD can provide further understanding of the TAE mode due to the benefits of simplicity and outstanding spatial and temporal resolutions.

5.3 Future work

Several improvements are possible for future experiments. In addition to having a well-polished emitter surface, a new extraction grid design with less heat expansion can help maintain the collimation of the fast-ion beam over long operation hours. The fast-ion signal-to-noise is usually a limit for conducting resonance experiment at large numbers of gyro-cycles. Coulomb scattering, beam divergence and the intensity loss of the beam to the plasma make distant observations more difficult. The beam emission current is usually kept low (< 1 mA) since it is inversely proportional to the source lifetime (~ 20 hrs). The cost of LAPD run time to replace the source on site (~ 6 hr) and the monetary expense are both significant. A customized lithium-aluminosilicate refilling vacuum furnace has been designed and tested to be capable of produce glassy emission material using low-cost raw powder (Heatwave Labs, Inc.). Eventually a Li_7^+ source containing two times the emission material (thicker scab) at half the cost would be practical to operate at much higher emission current. Another way to improve the fast-ion signal-to-noise is to design a pre-amplifier[3, 4] right next to the fast-ion analyzer in order

to drive the ~ 10 ft long signal line. This would also enable the analyzer to observe SAW frequency signal at chosen spatial locations.

An antenna containing two current loops at the correct phase difference can produce left-circularly polarized SAW. A small gyro-radius (~ 2.5 cm) fast-ion orbit can be designed to stay in phase and direction with the wave electric field for near a complete cycle, which further enhances the resonance effect. A smaller footprint of lithium source is required for this experiment and the existing 0.25" diameter lithium source[22] is suitable.

Fast-ion trapping in the SAW frame requires up to the full length of LAPD plasma. Orbit designs with fast ions finishing multiple gyro-cycles per port can have the SAW modified fast-ion energy oscillate faster along the *z* direction. Then it is convenient to fit at least one energy oscillating cycle as in FIG. 3.1 b).

Resonance experiments with other types of waves, e.g. electrostatic waves, can also be considered. Landau resonance experiments with the strong, low pitch angle Ar^+ rf source or the LAPD intense rf fast-ion source are been designed to implement in the near future.

For UC Irvine fast-ion group, this experiment has established a foundation for fast-ion transport experiments in turbulence fields. Nonlinear heating of fast-ion beam with much stronger SAW fields (amplitude $\delta B / B$ up to 1%) is one adjacent experiment to try based on L. Chen's multi-mode heating theory. The natural multi-mode triangular wave drive can be used to launch SAWs with multiple frequencies and random phases simultaneously. A conductive, fast-ion gyro-diameter sized disk was inserted into the LAPD plasma and Alfvén-drift wave turbulence was created downstream (FIG. 5.1).

Fast-ion orbit designed to overlap with the strong turbulence fields showed non-classical transport effects. Further experiments like this will be conducted.

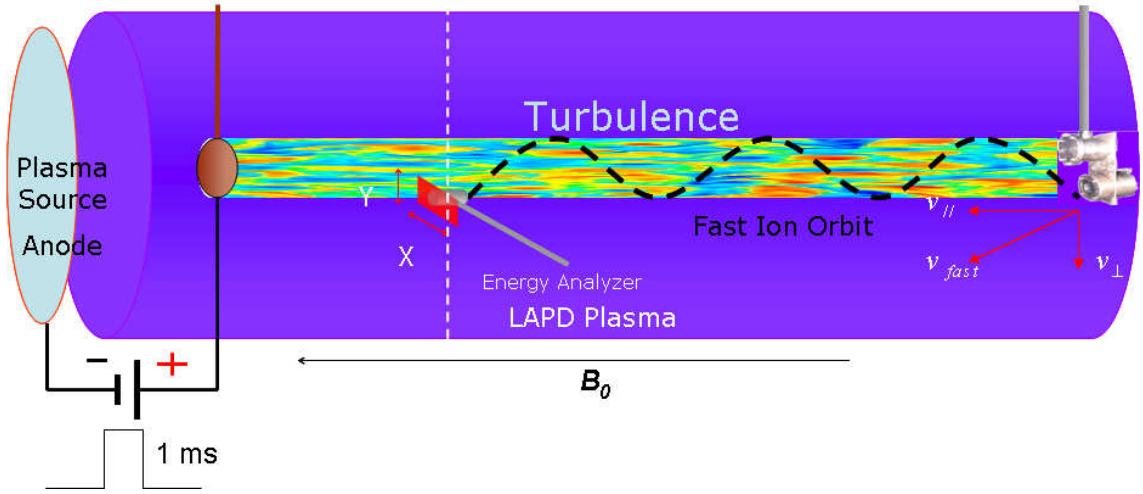

FIG. 5.1. Fast ion transport under turbulence fields experiment in the LAPD plasma.
RF source was used in the July 2004 experiment.

It will be further intriguing to study fast-ion transport in modes similar to the TAE mode in a Tokamak. In order to create eigenmodes in this system, the axial periodicity has to be broken with a strong defect, which can be made possible by introducing a sector of magnet with much stronger background field (up to 3.5 kG) compared to the regular mirror field (FIG. 5.2). The mirror field periods also need to match the reflective boundary locations at both ends in order to provide the higher Q factor for the possible modes.

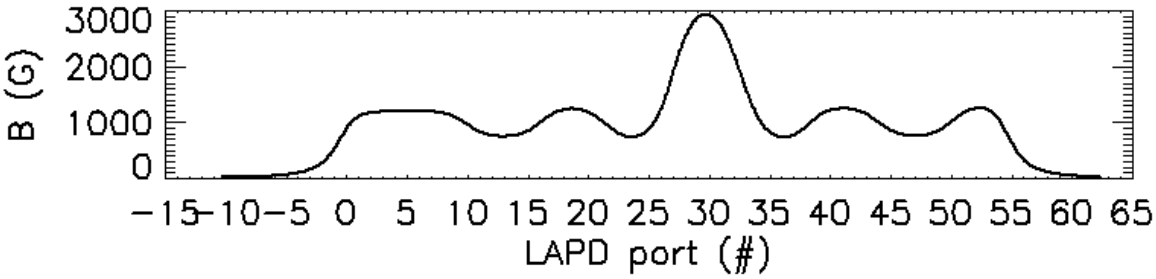

FIG. 5.2. Magnetic field with defect in the mirror array in the LAPD.
(July 2006 LAPD run)

[1] G. Y. Fu and J. W. Van Dam, Phys. Fluids B **1** (10), 1949 (1994).

[2] H. L. Berk, J. W. Van Dam, Z. Guo, and D. M. Lindberg, Phys. Fluids B **4** (7), 1806 (1992).

[3] R. A. Pitts and R. Chavan,S. J. Davies, S. K. Erents, G. Kaveney, G. F. Matthews, G. Neill, J. E. Vince and JET-EFDA workprogramme contributors, Rev. Sci. Instr. **74** (11), 4644 (2003)

[4] P. Pribyl, W. Gekelman, M. Nakamoto, E. Lawrence, F. Chiang, J. Stillman, J. Judy, N. Katz, P. Kintner, P. Niknejadi, Rev. Sci. Instr. **77,** 073504 (2006)

APPENDIX A: Typical Ion Beam and the LAPD Plasma Parameters

I. The LAPD plasma (Helium plasma)

Magnetic field, B	1.0 -2.0 kG
Pressure, P	2.3×10^{-5} *Torr*
Electron density in afterglow, n_e	10^{11} cm^{-3}
Electron density in Discharge, n_e	2×10^{12} cm^{-3}
Neutral density, n_0	6×10^{11} cm^{-3}
Electron temperature in afterglow, T_e	0.13 eV
Electron temperature in Discharge, T_e	6 - 7 eV
Ion temperature in afterglow, T_i	0.1 eV
Ion temperature in Discharge, T_i	1 eV
Plasma column length	18 m
Plasma column diameter	70 cm
Cathode-anode discharge current	5 - 6 kA
Cathode-anode discharge frequency	1 Hz
Afterglow time	50-60 ms
Discharge time	8 - 10 ms
Floating potential	45-50 V

II. Fast-ion beam (argon beam) and ion gun

Beam energy, W	~ 600 eV
Beam current density, j	1 mA/cm^2
Beam size	0.5 cm Dia.
Pitch angle, θ	28 - 50º
Gyro-radius of fast ions, ρ	3 - 6 cm
Emitter voltage	600V
Accelerator voltage	- 100 V
Energy spread, ΔE	~15 eV
Beam divergence	~5 degrees

APPENDIX B: Important Data Sets Supporting Experimental Results

In the LAPD backup folder (usually two copies on the lab computers), a data run between July 2004 and Dec 2007 can be found in "PLASMA\Fast Ion Turbulence\UCLA\". Each data run has a separate folder with the month or the first day of the experiment to be the folder name. A master experiment log is in MS Excel format and named "Exp log 5.9.2005", for example, which contains the details of the data sets taken during that run. If the data set contains hdf5 copies, then it is convenient to use an IDL program called "read_parameters.pro" to load the experimental setups for each data set. Important data set names and corresponding programs related to the results shown in this thesis is listed as follows.

I. Fast Ion Doppler Resonance Experiment

Programs can be found in PLASMA\Fast Ion Turbulence\UCLA\\LAPDdata\9.11.2007FIAR\FIAR.prj

Figure	Data Set(s)	IDL programs
FIG. 3.1	Fig1_FIAR_bdata.dat	saw_init_59mm.pro
		derivs_alfven_59mm.pro
	PLASMA\Fast Ion Turbulence\simulation\single particle alfven motion	lorentz_saw_59mm.pro
		Fig1_FIAR.pro
FIG.3.2	jan20_0.1_0.8_0.005wci_norec_40ports.dat	Fig2_FIAR_a.pro
	jan28_0.1_0.8_0.005wci_norec_3ports.dat	fig2b_FIAR.pro
	jan28_0.1_0.8_0.005wci_norec_10ports.dat	
	feb12_0.1_0.8_0.005wci_norec_3ports_10G.dat	
	PLASMA\Fast Ion Turbulence\simulation\single particle	

	alfven motion	
FIG.3.4	orbit_MC 0.650000Feb140G.dat	DSC_FIAR.pro
	orbit_MC 0.650000Jan25.2008.dat	orbits_SAW.pro
	orbit_MC 0.200000Feb1510G.dat	Fig_4_FIAR.pro
	PLASMA\Fast Ion Turbulence\simulation\Monte_Carlo_SAW	
FIG.3.7	10th_HYBIII_p32_sine_95kHz. SIS 3301 .dat	Fig_active_beam_profile_FIAR.pro
	10th_HYBIII_p32_sine_95kHz.hdf5	
	(Use only the no SAW data)	
	\LAPDdata\12.04.2007FIAR	
FIG.3.8	6th_b6_p33_50V_297kHz.SIS 3301.dat	Fig88_FIAR.pro
	\LAPDdata\12.04.2007FIAR	
FIG.3.9	16th_b9_p36_fscan_50-500_10kHz_1200Gflare_80V. SIS 3301.dat	Fig7b_rms_FIAR.pro
	\LAPDdata\9.11.2007FIAR	(7b is old label)
FIG.3.10	\LAPDdata\9.11.2007FIAR\16th_b9_p36_plane_fscan_80V. SIS 3301.dat	Fig10_FIAR.pro
	\LAPDdata\12.04.2007FIAR\10th_b6_p33_SAW_8f. SIS 3301.dat	
	\LAPDdata\9.11.2007FIAR\17th_b10_p31_plane_fscan_80V. SIS 3301.dat	
FIG.3.11	\LAPDdata\12.04.2007FIAR\9th_HYBIII_p32_SAW_8f. SIS 3301.dat	FIG_RC_SAW.pro
		FIG_RC_SAW_plot.pro
FIG.3.12	\LAPDdata\9.11.2007FIAR\16th_FIAR_HYBIII_297kHz_80V. SIS 3301.dat	rdsaw10shots_911_saveallshots.pro
		Fig12_FIAR.pro
		Fig12a_FIAR.pro
		Fig12bc_FIAR.pro
		read_saw_1s_6chn_911.pro
FIG.3.13	\LAPDdata\9.11.2007FIAR\16th_FIAR_HYBIII_297kHz_80V. SIS 3301.dat	Fig13a_FIAR.pro
		Fig13bc_FIAR.pro
		Fig13bc_FIAR_plot.pro

FIG.3.15	\LAPDdata\12.04.2007FIAR\9th_HYBIII_p32_SAW_8f. SIS 3301.dat	Fig15a_FIAR.pro
		Fig15a_FIAR_plot.pro
		Fig15b_FIAR_plot.pro
FIG.3.16	16th_b9_p36_fscan_50-500_10kHz_1200Gflare_80V. SIS 3301.dat	Fig16_FIAR.pro
	\LAPDdata\9.11.2007FIAR	Fig16_FIAR_data.pro

II. SAW Spectra Gap in the LAPD Mirror Array

Programs can be found in PLASMA\Fast Ion Turbulence\UCLA\1.25.2007 MAE\data \MAE2007Jan.prj

Figure	Data Set(s)	IDL programs
FIG. 4.3	triple_jan27_p13f_m1200base_13ne. SIS 3301.dat	Figure_2_plasma.pro
	triple_jan26_p19m_m1200base_13ne_c. SIS 3301.dat	
	triple_jan27_p35m_m1200base_13ne. SIS 3301.dat	
	PLASMA\Fast Ion Turbulence\UCLA\1.25.2007 MAE\data	
FIG. 4.4	Jan26th_p14_no6_fscan_m1200_rod_13 ne. SIS 3301.dat	Figure_b_vs_r.pro
		Figure_rb2_vs_r.pro
FIG. 4.6	Jan26th_p14_no6_fscan_m1200_rod_13 ne. SIS 3301.dat	Figure_5_U_character.pro
	PLASMA\Fast Ion Turbulence\UCLA\1.25.2007 MAE\data	Fig5_iant.pro
	Jan26th_p14_no6_fscan_m1200_rod_13 ne	
FIG. 4.8	Jan26th_p14_no6_fscan_m1200_rod_13 ne	Fig7a.pro
	p14_p36_m1200deep_10ne	Fig7a_flat.pro
	p14_p36_m1200shal25percent_13ne	Fig7b_disk.pro
	Jan25th_p14_no6_fscan_flat1200_rod	
	PLASMA\Fast Ion Turbulence\UCLA\1.25.2007 MAE\data	
FIG. 4.10	Jan26th_p14_no6_fscan_m1200_rod_13 ne. SIS 3301.dat	Fig9.pro
	PLASMA\Fast Ion Turbulence\UCLA\1.25.2007 MAE\data	running_ccov.pro

APPENDIX C: Schematics for Experimental Apparatuses

I. 0.6” dia. Emitter Lithium Fast-ion Source (LiGun)

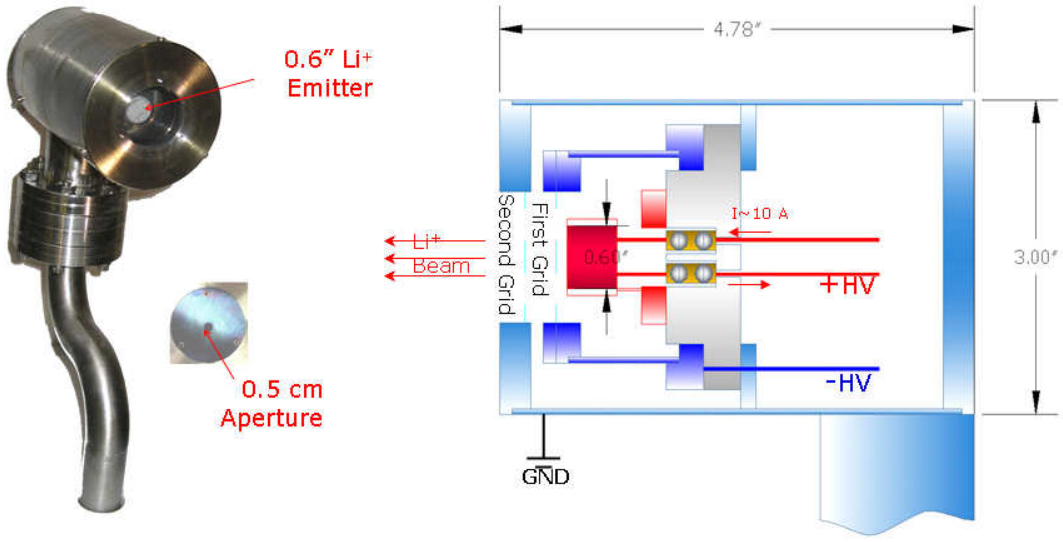

FIG. 0.1 Photograph (left) and inside structure (right) of the 0.6” emitter lithium source (LiGun).

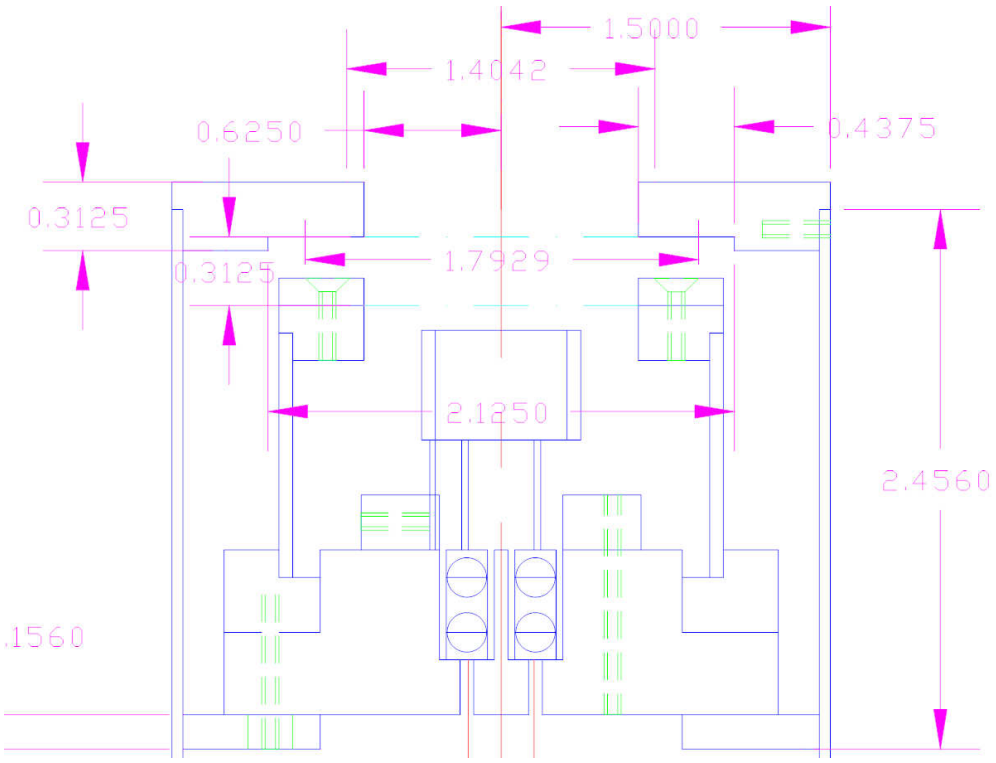

FIG. 0.2. Dimensions for original inner structures of 0.6” emitter lithium source.

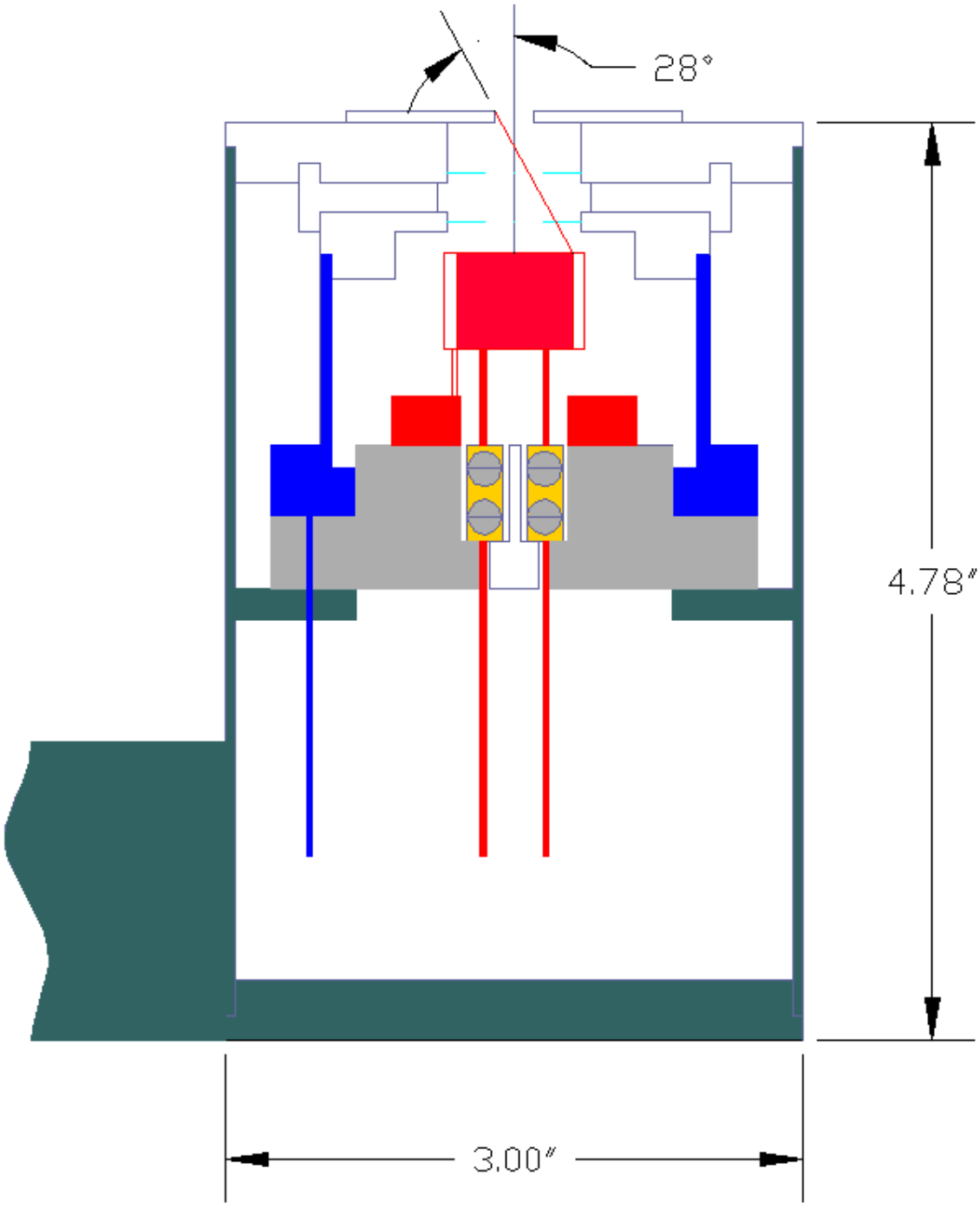

FIG. 0.3. Modified grid structure of 0.6” emitter lithium source showing 28º of incident angle to the edge of the emitter, with 0.5 cm diameter aperture.

II. 0.25” dia. Emitter Lithium Fast-ion Source (mini-LiGun)

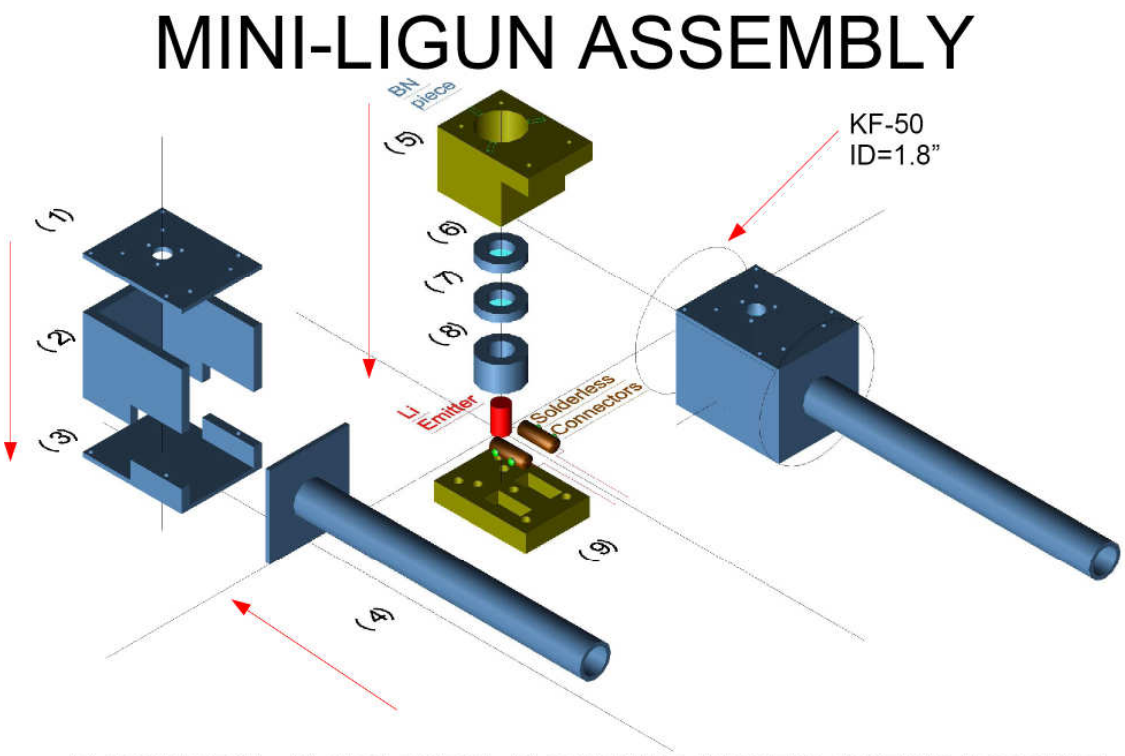

(1) FRONT PIECE (2) MIDDLE PIECE (3) BACK PIECE (4) BOTTOM PIECE W/ 0.5” OD SHAFT

(5) BN FRONT PIECE (6) 2ND GRID (7) 1ST GRID (8) EMITTER BASE (9) BN BACK PIECE

Transparent Front View

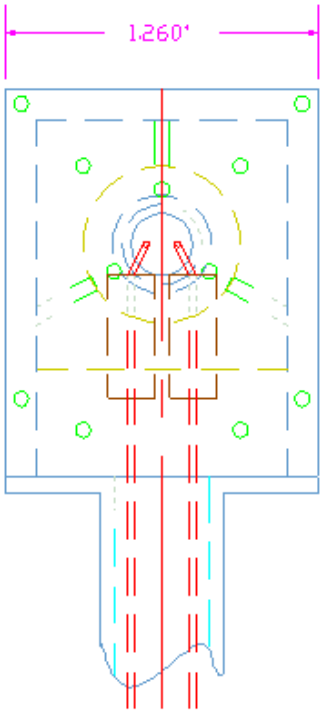

Cutaway Side View

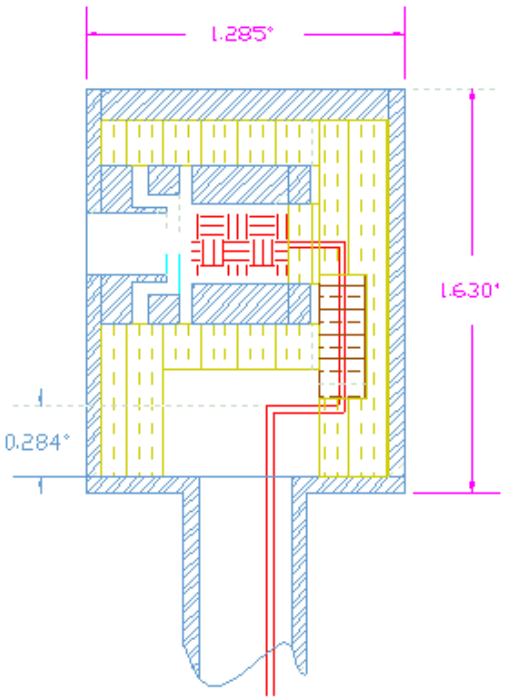

III. Lithium Source High Voltage Power Supply Schematics

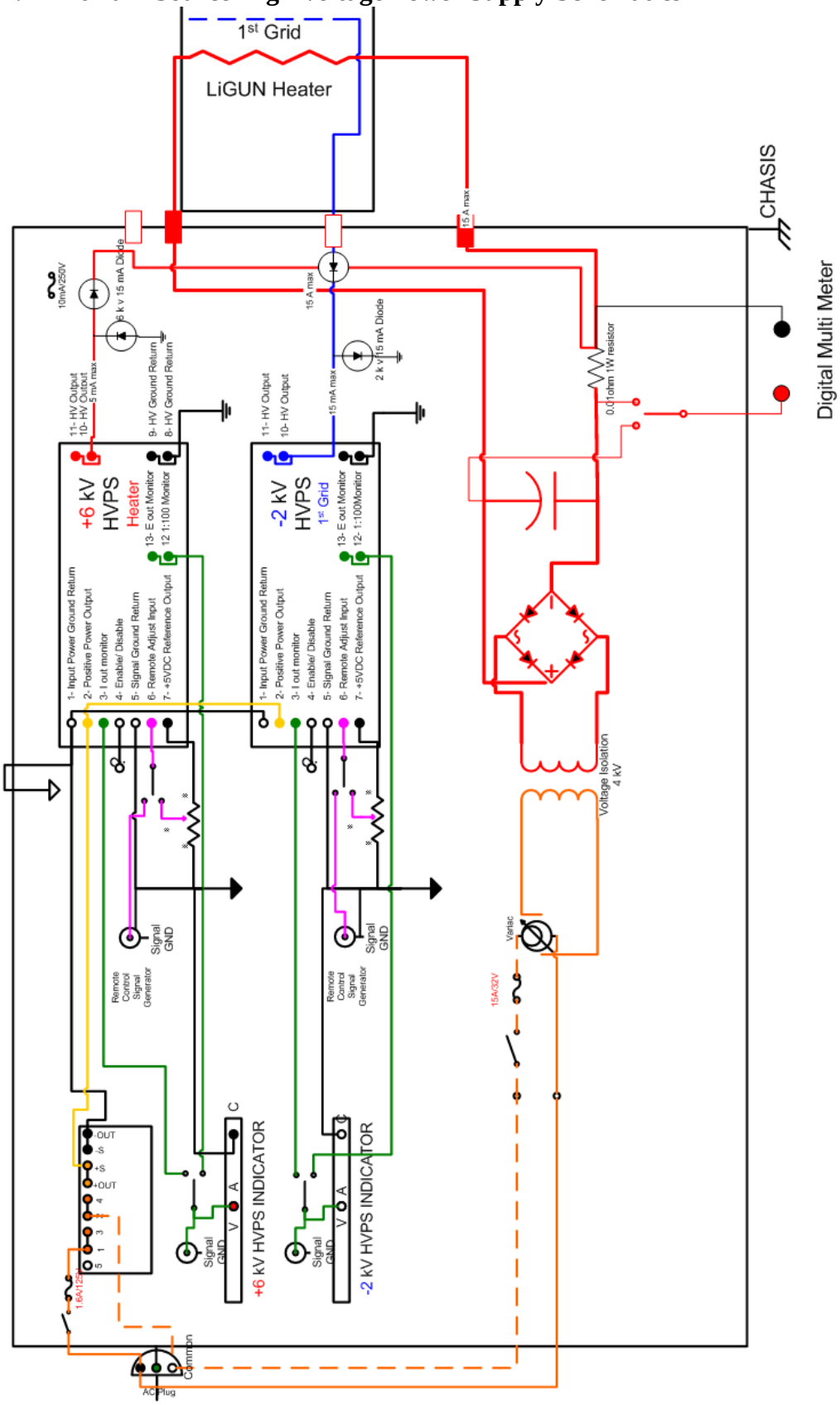

IV. Lithium Source Re-coating Device Schematics

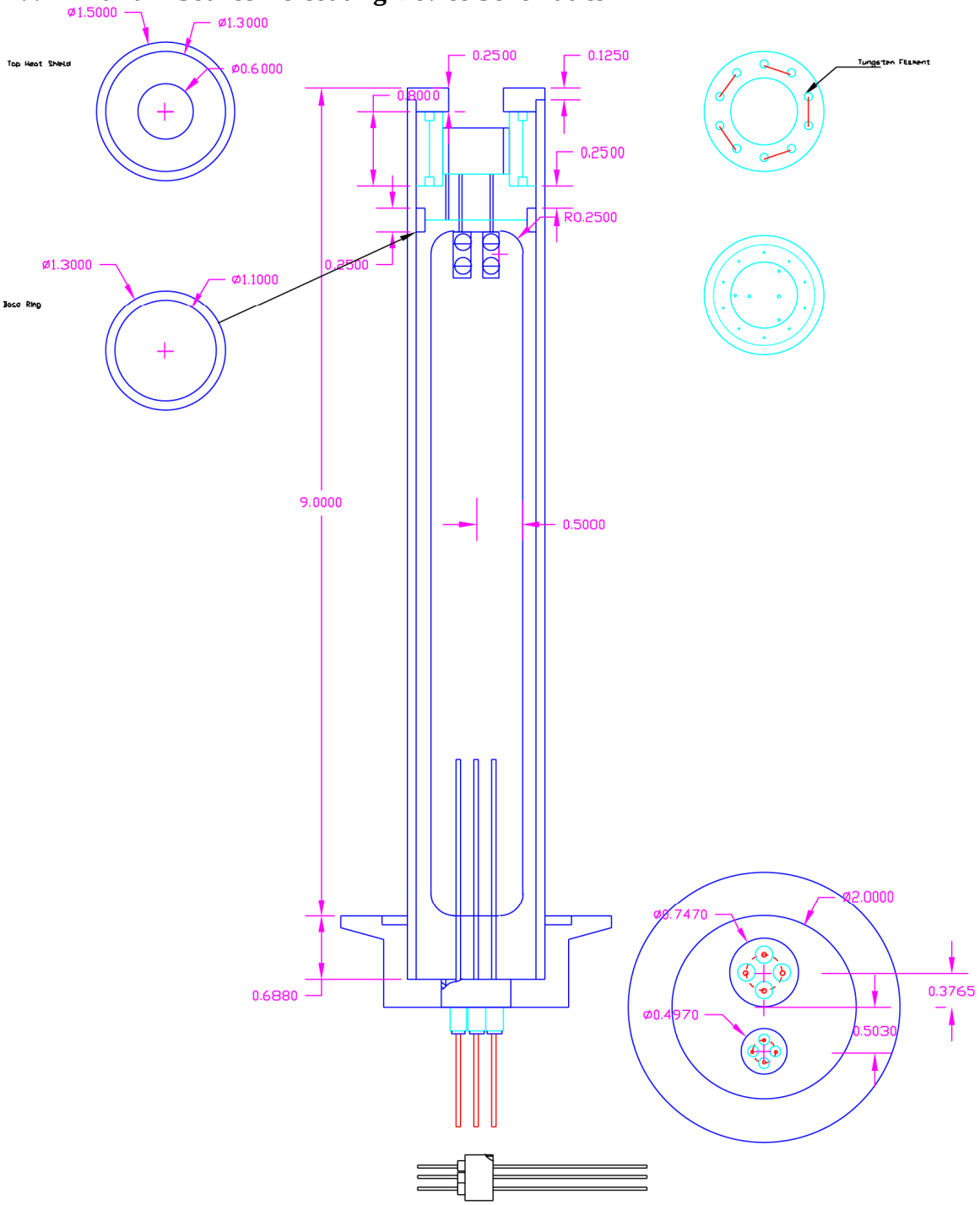

V. RF-Gun Feedthrough Modifications

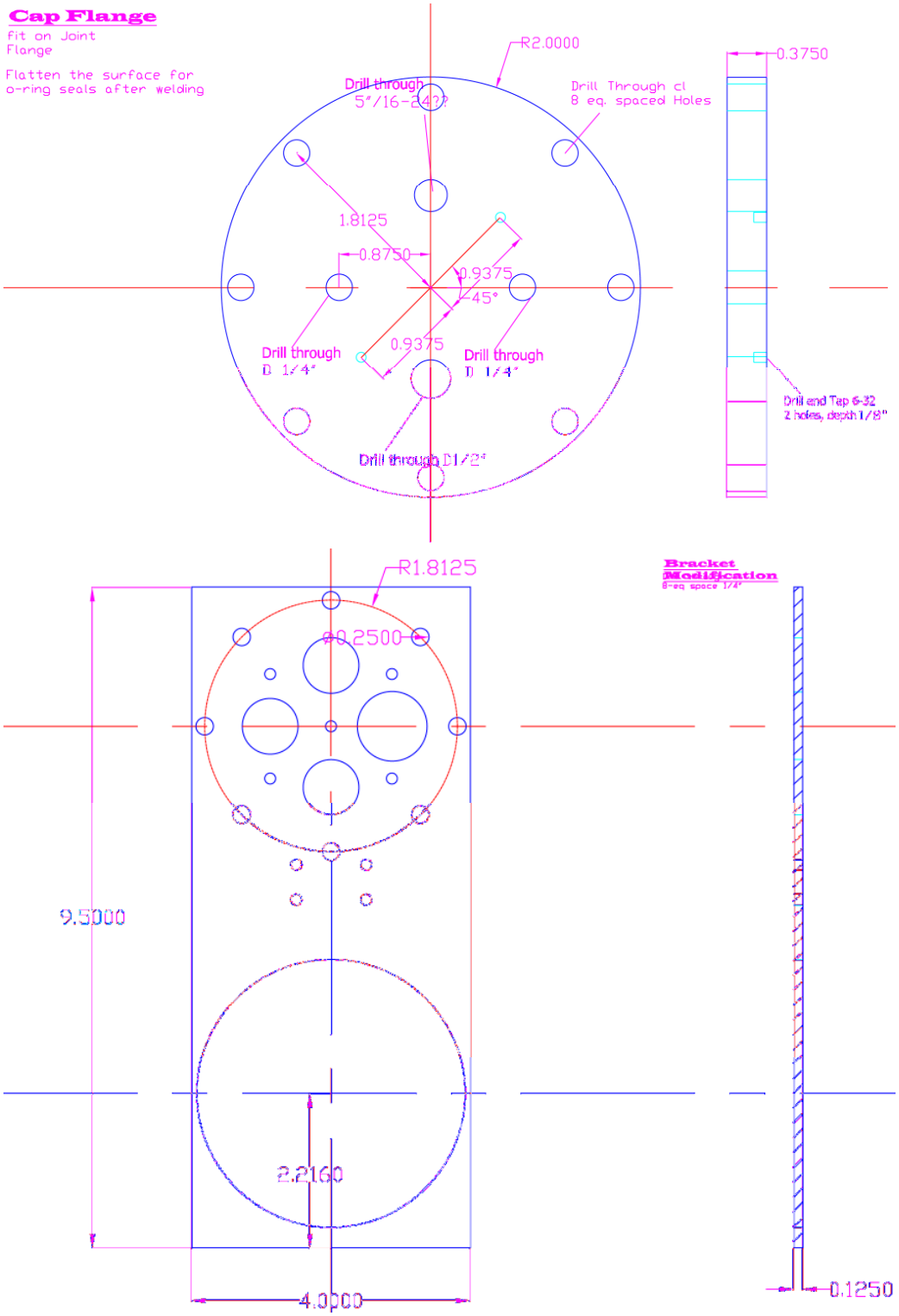

APPENDIX D: Instrument Calibration Data

I. Calibration of *b-dot* probes at the LAPD

PROBE	Amp Box		V/B (V/G)	R^2	V/B @ 5MHz		V/B @ 10MHz	
					measured	calculated	measured	calculated
#1	#1	X	(5.9899e-08)f	0.99404	0.310	0.299	0.576	0.599
		Y	(5.5862e-08)f	0.99165	0.290	0.279	0.528	0.279
		Z	(5.8158e-08)f	0.99475	0.306	0.291	0.561	0.291
#2	#2	X	(6.6878e-08)f	0.9929	0.350	0.334	0.631	0.669
		Y	(5.3393e-08)f	0.99387	0.271	0.267	0.516	0.534
		Z	(5.2683e-08)f	0.99379	0.275	0.263	0.513	0.527
#3	#3	X	(2.6969e-08)f	0.98945	0.143	0.135	0.259	0.270
		Y	(4.6448e-08)f	0.99253	0.240	0.232	0.445	0.464
		Z	(5.9999e-08)f	0.99239	0.318	0.300	0.582	0.600
#4	#4	X	(6.273e-08)f	0.98955	0.323	0.314	0.594	0.627
		Y	(5.8457e-08)f	0.98933	0.309	0.292	0.544	0.585
		Z	(5.3393e-08)f	0.9923	0.273	0.267	0.521	0.534
#5	#5	X	(6.4868e-07)f	0.99336	3.397	3.243	6.214	6.487
		Y	(5.573e-07)f	0.99444	2.894	2.787	5.352	5.573
		Z	(4.954e-07)f	0.99438	2.577	2.477	4.770	4.954
#6	#6	X	(6.2737e-07)f	0.99068	3.315	3.137	5.960	6.274
		Y	(5.1941e-07)f	0.99358	2.717	2.597	4.973	5.194
		Z	(6.0082e-07)f	0.99172	3.165	3.004	5.724	6.008
#7	#7	X	(5.6474e-07)f	0.99291	2.972	2.824	5.387	5.647
		Y	(6.4637e-07)f	0.99394	3.377	3.232	6.217	6.464
		Z	(6.0086e-07)f	0.99557	3.126	3.004	5.800	6.009
#8	#8	X	(5.8764e-07)f	0.99197	3.099	2.938	5.599	5.876
		Y	(6.4915e-07)f	0.98767	3.468	3.246	6.092	6.492
		Z	(6.1804e-07)f	0.99254	3.252	3.090	5.881	6.180
#9	#9	X	(5.8474e-07)f	0.98837	3.107	2.924	5.492	5.847
		Y	(6.7606e-07)f	0.99022	3.592	3.380	6.403	6.761
		Z	(5.4620e-07)f	0.99318	2.863	2.731	5.218	5.462
#10	#10	X	(5.5993e-07)f	0.99092	2.951	2.800	5.306	5.599
		Y	(6.3245e-07)f	0.99139	3.346	3.162	6.005	6.325
		Z	(4.7036e-07)f	0.99316	2.468	2.352	4.497	4.704